

CHARACTERIZING, IDENTIFYING, AND IMAGING OXIDIZED PHOSPHOLIPIDS BY  
MATRIX-ASSISTED LASER DESORPTION/IONIZATION TANDEM MASS  
SPECTROMETRY

By

WHITNEY LEIGH STUTTS

A DISSERTATION PRESENTED TO THE GRADUATE SCHOOL  
OF THE UNIVERSITY OF FLORIDA IN PARTIAL FULFILLMENT  
OF THE REQUIREMENTS FOR THE DEGREE OF  
DOCTOR OF PHILOSOPHY

UNIVERSITY OF FLORIDA

2013

© 2013 Whitney Leigh Stutts

To my loving family and cherished friends

## ACKNOWLEDGMENTS

First, I thank my advisor, Dr. Richard Yost, for his guidance throughout the last five years and for facilitating a learning environment where ideas are always shared and independent thinking is always encouraged. I am also grateful to my committee members, Dr. David Powell, Dr. Gail Fanucci, Dr. Frank Bova, and Dr. Tim Garrett, who have offered their advice and time in support of this research. Additionally, I thank all my fellow Yost group members, past and present, for their insightful discussions and review of this work. I would also like to especially thank Dr. Jodie Johnson, Dr. Mike Napolitano and Dr. Rob Menger, who have been excellent colleagues and friends. I also express my sincere appreciation for two undergraduate research assistants, Kerolyn de Souza Valente and Katelyn Bobek, whose enthusiasm and dedication have aided the success of this work.

I must also acknowledge several people who inspired and motivated me along this journey to my Ph.D. My love for chemistry was sparked by Dr. Roger Bacon, a professor at Western Carolina University, and his wife Lisa during a summer chemistry program for high school students. Their passion for chemistry was obvious and apparently contagious. Once at North Carolina State University, Dr. Phil Brown inspired me with his enthusiastic advanced-organic lectures, stories of graduate school, and hobby of backyard biodiesel synthesis. My undergraduate research advisor, Dr. Damian Shea, gave me the opportunity to test my aptitude for research and to participate in a study abroad program for water management and environmental forensics in China and Vietnam, which taught me the value of interdisciplinary collaborations for solving global problems.

During my graduate career, I have also had the pleasure of collaborating with many great scientists around the world. I thank Dr. Paolo Di Mascio at the University of São Paulo, Brazil for allowing me the opportunity to visit his lab and learn more about lipid oxidation and the detection of these products by mass spectrometry. I would also like to thank Dr. Ron Heeren and his group at FOM Institute AMOLF, especially Andrés Kiss, for a rewarding collaboration and valuable research experience. Additionally, much of this work would not have been possible without Dr. Nigel Calcutt at the University of California San Diego. Dr. Calcutt provided all of the rat tissue for these studies and valuable insight into the involvement of lipid oxidation in diabetic peripheral neuropathy.

I would also like to thank my family and friends for all their love and support. Most of all, I thank my mom; without her, I would not be the person I am today. Furthermore, I thank both my dad for instilling in me the importance of higher education and my sister, Lauren, for her unconditional love and for sharing with me so many of life's finest moments. I would also like to thank my grandparents and my Aunt Delita, who have been a solid support system throughout my life, even when life took me to Florida. In addition to my loving family, I have also been blessed with great friends who have made Gainesville feel like home. I thank Jess for a truly incredible friendship and many memories that will last a life time. Lastly, I am grateful to my boyfriend, Mike, who has loved, encouraged, and supported me throughout the last five years.

## TABLE OF CONTENTS

	<u>page</u>
ACKNOWLEDGMENTS.....	4
LIST OF TABLES.....	8
LIST OF FIGURES.....	9
ABSTRACT .....	12
CHAPTER	
1 ANALYSIS OF OXIDIZED PHOSPHOLIPIDS BY MATRIX-ASSISTED LASER DESORPTION/IONIZATION TANDEM MASS SPECTROMETRY.....	14
Research Motivation.....	14
Lipids and Lipid Oxidation.....	15
Phospholipid Oxidation.....	16
Techniques for Measuring Phospholipid Oxidation .....	18
Matrix-Assisted Laser Desorption/Ionization.....	19
Matrix Selection.....	20
MALDI Process.....	21
Instrumentation .....	22
Linear Ion Trap.....	23
Tandem Mass Spectrometry .....	25
Mass Spectrometric Imaging .....	26
Overview of Dissertation.....	27
2 CHARACTERIZATION OF PHOSPHATIDYLCHOLINE OXIDATION PRODUCTS BY MALDI MS <sup>n</sup> .....	38
Introduction.....	38
Experimental Methods .....	40
Chemicals.....	40
Preparation of OxPC Standards.....	40
Preparation of Spinal Cord Tissue.....	41
MALDI MS Instrumentation .....	41
MS <sup>n</sup> Instrumental Parameters .....	42
Accurate Mass Measurements.....	43
Results and Discussion.....	43
MS <sup>2</sup> Characterization of the [M+H] <sup>+</sup> Ions of Short-Chain OxPCs.....	44
MS <sup>n</sup> Characterization of the [M+Na] <sup>+</sup> Ions of Short-Chain OXPCs.....	45
Identifying and Imaging OxPCs in Spinal Cord Tissue.....	50
Conclusions .....	51

3	MALDI MS <sup>n</sup> CHARACTERIZATION OF PHOSPHATIDYLETHANOLAMINE OXIDATION PRODUCTS .....	67
	Introduction .....	67
	Experimental Section .....	69
	Chemicals.....	69
	Oxidation Procedure.....	69
	MS <sup>n</sup> Experimental Parameters .....	70
	Results and Discussion.....	70
	Autoxidation of POPE, PLPE, PDPE, and SDPE .....	70
	MS <sup>n</sup> of [M+Na] <sup>+</sup> Ions of OxPEs.....	71
	MS <sup>n</sup> of [M-H+2Na] <sup>+</sup> Ions of OxPEs .....	76
	Conclusions .....	78
4	IDENTIFYING AND IMAGING PHOSPHOLIPID OXIDATION PRODUCTS BY MALDI MS <sup>n</sup> .....	91
	Introduction .....	91
	Experimental Methods .....	92
	Chemicals.....	92
	Tissue Preparation .....	93
	In Vitro Oxidation.....	93
	Mass Spectrometry .....	94
	Statistical Analysis.....	94
	Results and Discussion.....	95
	MS Analysis of UV-exposed and Unexposed Spinal Cord .....	95
	PCA of UV-exposed and Unexposed Spinal Cord.....	96
	MS <sup>n</sup> Analysis of Oxidized Phospholipids in the Spinal Cord.....	98
	Unsaturated phosphatidylcholines .....	98
	Long-chain oxidation products .....	100
	Short-chain oxidation products.....	103
	Conclusions .....	105
5	CONCLUSIONS AND FUTURE WORK .....	121
	Conclusions .....	121
	Future Work .....	124
	LIST OF REFERENCES .....	126
	BIOGRAPHICAL SKETCH.....	134

## LIST OF TABLES

<u>Table</u>		<u>page</u>
2-1	Nomenclature of the OxPC standards analyzed.....	53
2-2	Product ions observed in the MS <sup>2</sup> spectra of [M+H] <sup>+</sup> ions of PAzPC, PONPC, PGPC, POVPC, and KOdiAPC.....	54
2-3	Product ions observed in MS <sup>2</sup> spectra of [M+Na] <sup>+</sup> ions of PAzPC, PONPC, PGPC, POVPC, and KOdiAPC.....	56
2-4	Product ions observed in MS <sup>3</sup> spectra of [M+Na-N(CH <sub>3</sub> ) <sub>3</sub> ] <sup>+</sup> ions of PAzPC, PONPC, PGPC, POVPC, and KOdiAPC.....	58
3-1	PE standards autoxidized and analyzed.....	79
3-2	Nomenclature of the observed PE oxidation products.....	80

## LIST OF FIGURES

<u>Figure</u>	<u>page</u>
1-1	Glycerophospholipid structure and select head groups..... 29
1-2	Two types of phospholipid oxidation products investigated in this work. .... 30
1-3	Structures of the three MALDI matrices evaluated for the analysis of oxidized phospholipids..... 31
1-4	Schematic of the MALDI process. .... 32
1-5	Schematic of the Thermo Scientific MALDI LTQ XL used in this work. .... 33
1-6	Schematic of the two-dimensional LIT adapted from Schwartz et al. Ions transmitted through the front section along the z-axis and are trapped in the center section by DC axial trapping and RF radial trapping..... 34
1-7	Mathieu stability diagram of the two-dimensional LIT. Since LITs are typically operated in RF-only mode ( $a_x = 0$ ), ions are successfully trapped along the $q_x$ axis with a low-mass cut-off (LMCO) $q_x = 0.908$ . .... 35
1-8	Sample mass spectra illustrating an $MS^2$ experiment..... 36
1-9	Mass spectrometric imaging (MSI) workflow. .... 37
2-1	$MS^2$ product ion spectrum of $m/z$ 666, the $[M+H]^+$ ion of PAzPC. The structure and proposed fragmentation of the ion at $m/z$ 666 are also shown. .... 55
2-2	$MS^2$ product ion spectrum of $m/z$ 688, the $[M+Na]^+$ ion of PAzPC. The structure and proposed fragmentation of the ion at $m/z$ 688 are also shown. .... 57
2-3	$MS^3$ product ion spectrum of $m/z$ 688→629, the $[M+Na-N(CH_3)_3]^+$ ion of PAzPC. The structure and proposed fragmentation of the ion at $m/z$ 629 are also shown..... 59
2-4	$MS^4$ product ion spectrum of $m/z$ 688→629→505, the $[M+Na-HPO_4(CH_2)_2N(CH_3)_3]^+$ ion of PAzPC. The proposed structure and fragmentation of the ion at $m/z$ 505 are also shown. .... 60
2-5	$MS^4$ product ion spectrum of $m/z$ 672→613→489, the $[M+Na-HPO_4(CH_2)_2N(CH_3)_3]^+$ ion of PONPC. The proposed structure and fragmentation of the ion at $m/z$ 489 are also shown. .... 61
2-6	$MS^4$ product ion spectrum of $m/z$ 632→573→449, the $[M+Na-HPO_4(CH_2)_2N(CH_3)_3]^+$ ion of PGPC. The proposed structure and fragmentation of the ion at $m/z$ 449 is also shown..... 62

2-7	MS <sup>4</sup> product ion spectrum of $m/z$ 616→557→433, the [M+Na-HPO <sub>4</sub> (CH <sub>2</sub> ) <sub>2</sub> N(CH <sub>3</sub> ) <sub>3</sub> ] <sup>+</sup> ion of POVPC. The proposed structure and fragmentation of the ion at $m/z$ 433 is also shown.....	63
2-8	MS <sup>4</sup> product ion spectrum of $m/z$ 686→627→503, the [M+Na-HPO <sub>4</sub> (CH <sub>2</sub> ) <sub>2</sub> N(CH <sub>3</sub> ) <sub>3</sub> ] <sup>+</sup> ion of KOdiAPC. The proposed structure and fragmentation of the ion at $m/z$ 503 are also shown. ....	64
2-9	Schemes for the proposed intramolecular retro-ene mechanism. ....	65
2-10	Identification and imaging of two proposed OxPCs at $m/z$ 716. The MS spectrum illustrates the complex mixture of biomolecules observed in tissue. ...	66
3-1	MS spectrum of POPE A) before and B) after autoxidation.....	81
3-2	Fragmentation pattern of [PAzPE+Na] <sup>+</sup> from autoxidized POPE.....	82
3-3	Fragmentation pattern of [PSuPE+Na] <sup>+</sup> from autoxidized PDPE.....	83
3-4	Fragmentation pattern of [SSuPE+Na] <sup>+</sup> from autoxidized SDPE.....	84
3-5	Fragmentation pattern of [PONPE+Na] <sup>+</sup> from autoxidized POPE.....	85
3-6	Fragmentation pattern of [POBPE+Na] <sup>+</sup> ( $m/z$ 560) from autoxidized PDPE.....	86
3-7	Fragmentation pattern of [SOBPE+Na] <sup>+</sup> ( $m/z$ 588) from autoxidized SDPE.....	87
3-8	MS <sup>2</sup> fragmentation of [PAzPE-H+2Na] <sup>+</sup> ( $m/z$ 668) from autoxidized POPE. The proposed structure and sites of fragmentation are also shown. ....	88
3-9	MS <sup>2</sup> fragmentation of [PONPE-H+2Na] <sup>+</sup> ( $m/z$ 652) from autoxidized POPE. The proposed structure and sites of fragmentation are also shown. ....	88
3-10	MS <sup>2</sup> fragmentation of [PSuPE-H+2Na] <sup>+</sup> ( $m/z$ 598) from autoxidized PDPE. The proposed structure and sites of fragmentation are also shown. ....	89
3-11	MS <sup>2</sup> fragmentation of [POBPE-H+2Na] <sup>+</sup> ( $m/z$ 582) from autoxidized PDPE. The proposed structure and sites of fragmentation are also shown. ....	89
3-12	MS <sup>2</sup> fragmentation of [SSuPE-H+2Na] <sup>+</sup> ( $m/z$ 626) from autoxidized SDPE. The proposed structure and sites of fragmentation are also shown. ....	90
3-13	MS <sup>2</sup> fragmentation of [SOBPE-H+2Na] <sup>+</sup> ( $m/z$ 610) from autoxidized SDPE. The proposed structure and sites of fragmentation are also shown. ....	90
4-1	MALDI MS spectrum from the left half of the tissue, which was exposed to UV for 4 hours (top) and from the right half of the tissue, which was not exposed to UV (bottom).....	106

4-2	Principal component 1 scaled loadings plot (left) and scores images (right) from the MSI data set in Figure 4-1. Principal component 1 dictates separation of the oxidized and unoxidized sides of the spinal cord.....	107
4-3	MS <sup>n</sup> of PC(16:0/18:1), an abundant unsaturated phospholipid in spinal cord tissue.....	108
4-4	MS <sup>2</sup> product ion spectrum of <i>m/z</i> 814, a proposed long-chain oxidation product of phosphatidylcholine. ....	109
4-5	MS <sup>3</sup> product ion spectrum of <i>m/z</i> 814→755. Images were generated by mapping the intensity of the product ions corresponding to the NLs of cyclophosphane (124 u), <i>sn</i> -1 moiety (256 u), and <i>sn</i> -2 moiety (314 u).....	110
4-6	MS <sup>4</sup> product ion spectrum of <i>m/z</i> 814→755→631. Product ions corresponding to the NLs of the <i>sn</i> -1 and oxidized <i>sn</i> -2 fatty acid substituents confirm the addition of two oxygens to the <i>sn</i> -2 moiety. ....	111
4-7	MS <sup>2</sup> product ion spectrum of <i>m/z</i> 842, a proposed long-chain oxidation product of phosphatidylcholine. ....	112
4-8	MS <sup>3</sup> product ion spectrum of <i>m/z</i> 842→783. ....	113
4-9	MS <sup>4</sup> product ion spectrum of <i>m/z</i> 842→783→659. Product ions corresponding to the NLs of the <i>sn</i> -1 and oxidized <i>sn</i> -2 fatty acid substituents confirm the addition of two oxygens to the <i>sn</i> -2 moiety. ....	114
4-10	MS <sup>2</sup> product ion spectrum of <i>m/z</i> 688, a proposed short-chain oxidation product of phosphatidylcholine. ....	115
4-11	MS <sup>3</sup> product ion spectrum of <i>m/z</i> 688→629. ....	116
4-12	MS <sup>4</sup> product ion spectrum of <i>m/z</i> 688→629→505.....	117
4-13	MS <sup>2</sup> product ion spectrum of <i>m/z</i> 716. Two possible isomeric short-chain oxidation products of phosphatidylcholine occur at <i>m/z</i> 716.....	118
4-14	MS <sup>3</sup> product ion spectrum of <i>m/z</i> 716→657. Product ions related to PC(16:0/11:0 COOH) and PC(18:0/9:0 COOH) are marked with stars and diamonds, respectively. ....	119
4-15	MS <sup>4</sup> product ion spectrum of <i>m/z</i> 716→657→533. Based on the observed fragmentation, the presence of two isomeric oxidized PCs, PC(16:0/11:0 COOH) and PC(18:0/9:0 COOH), was confirmed.....	120

Abstract of Dissertation Presented to the Graduate School  
of the University of Florida in Partial Fulfillment of the  
Requirements for the Degree of Doctor of Philosophy

CHARACTERIZING, IDENTIFYING, AND IMAGING OXIDIZED PHOSPHOLIPIDS BY  
MATRIX-ASSISTED LASER DESORPTION/IONIZATION TANDEM MASS  
SPECTROMETRY

By

Whitney Leigh Stutts

August 2013

Chair: Richard A. Yost  
Major: Chemistry

Understanding the involvement of lipid oxidation in both inflammatory processes and the pathogenesis of various diseases is an important endeavor. Despite growing interest in the field of lipidomics, lipid oxidation products remain poorly characterized. However, mass spectrometry, coupled with soft-ionization techniques, has become a key tool for investigating lipids and elucidating structural changes resulting from oxidative modifications. In this research, matrix-assisted laser desorption/ionization tandem mass spectrometry (MALDI MS<sup>n</sup>) techniques were developed for characterizing, identifying, and imaging oxidized phospholipids.

Specifically, the research presented in this work focused on three distinct aspects of oxidized phospholipid analysis. Initially, the MALDI MS<sup>n</sup> (where n = 2, 3, or 4) fragmentation pathways of short-chain phosphatidylcholine oxidation products (OxPCs) were characterized. This study identified several fragmentation pathways that allowed for unambiguous detection of low abundant OxPC species, and the developed method was applied for the identification of these species in rat spinal cord tissue. Next, a similar study was conducted for phosphatidylethanolamine oxidation products (OxPEs).

In this second study, novel fragmentation pathways were identified for short-chain aldehydic OxPEs. This proposed pathway resulted in a macrocyclic gas-phase rearrangement that can be exploited for MS<sup>n</sup> detection of these OxPEs in biological samples. The final study presented in this work describes a methodology utilizing principal component analysis (PCA) for untargeted detection of oxidized phospholipids following mass spectrometric imaging (MSI) experiments.

In summary, this work demonstrates that MALDI MS<sup>n</sup> provides a selective method for investigating individual molecular species resulting from phospholipid oxidation. Utilizing the MS<sup>n</sup> capabilities of the linear ion trap, OxPLs were distinguished from isobaric, and even isomeric, phospholipids. Furthermore, the utility of MALDI MS<sup>n</sup> in conjunction with multivariate data analysis techniques, namely PCA, for discovering, identifying, and imaging individual phospholipid oxidation products in spinal cord tissue is exemplified.

# CHAPTER 1

## ANALYSIS OF OXIDIZED PHOSPHOLIPIDS BY MATRIX-ASSISTED LASER DESORPTION/IONIZATION TANDEM MASS SPECTROMETRY

### **Research Motivation**

Increasing evidence suggests that oxidized lipids are markers and pathogenic factors in a variety of disease states.<sup>1</sup> Lipid oxidation has been implicated in numerous diseases including Alzheimer's,<sup>2-4</sup> age-related macular degeneration,<sup>5</sup> atherosclerosis,<sup>5,6</sup> cataractogenesis,<sup>5</sup> multiple sclerosis,<sup>7</sup> and rheumatoid arthritis.<sup>8</sup> Furthermore, several studies have demonstrated the involvement of oxidative stress and lipid oxidation in central nervous system injuries, including stroke, traumatic brain injury, and spinal cord injury.<sup>9</sup> Thus, there is growing interest in developing methods to identify potential biomarkers of oxidative damage or disease, which may lead to a better understanding of the involvement of lipid oxidation products in these various diseases.

With the advent of soft ionization techniques such as electrospray ionization (ESI)<sup>10</sup> and matrix-assisted laser desorption/ionization (MALDI),<sup>11,12</sup> mass spectrometry (MS) has become an indispensable tool in the emerging field of oxidative lipidomics.<sup>13</sup> Although still in a state of infancy, several review articles have provided the framework for and outlined the goals and challenges associated with this field.<sup>13-15</sup> Thus far, oxidative lipidomics studies have primarily focused on ESI of samples in a liquid state such as brain lipid extracts; however, the potential of MALDI for in situ identification and imaging has also been proposed.<sup>13,16</sup> This work makes significant contributions to the field of oxidative lipidomics as the first studies are described reporting MALDI tandem mass spectrometry (MS<sup>n</sup>) characterization of both short- and long-chain phospholipid oxidation products (OxPLs) and MS imaging of these products in intact tissue sections.

## Lipids and Lipid Oxidation

Lipids are vital structural components of cell membranes and are known to have various biochemical roles including energy storage, maintenance of electrochemical gradients, and nerve cell insulation.<sup>17,18</sup> Defined as “water-insoluble biomolecules that are highly soluble in organic solvents”,<sup>19</sup> lipids can be classified into storage and membrane lipids.<sup>20</sup> Membrane lipids can be sub-classified as phospholipids and glycolipids and then further classified according to the chemical structure of the lipid backbone (i.e., glycerol or sphingosine).<sup>20</sup>

Glycerophospholipids (GPLs), often referred to as phospholipids—although not all phospholipids contain a glycerol backbone, are abundant in cell membranes and lipoproteins.<sup>21</sup> These lipids are amphipathic (i.e., contain both hydrophobic and hydrophilic regions) and can, therefore, aggregate into bilayers.<sup>22</sup> GPLs consist of a glycerol backbone, a phosphate-containing polar headgroup at the *sn*-3 position of the glycerol backbone, and two non-polar fatty acid tails esterified to the *sn*-1 and *sn*-2 positions (Figure 1-1).<sup>1</sup> Depending on the nature of the polar head group at the *sn*-3 position, GPLs can be subdivided into distinct classes including phosphatidylcholines (PCs), phosphatidylethanolamines (PEs), and phosphatidylserines (PSs), as shown in Figure 1-1.<sup>23</sup>

In eukaryotic cells, phospholipid fatty acid moieties vary in length, typically having an even number of carbons between 14 and 24.<sup>24</sup> These fatty acids can be saturated (i.e., contain no double bonds) or unsaturated (i.e., contain one or more double bonds). Saturated fatty acids are typically bound to the *sn*-1 position, whereas unsaturated fatty acids, which have between one and six double bonds, are preferentially bound to the *sn*-2 position.<sup>25</sup> As saturated fatty acids are not as prone to oxidative modification as

mono- or poly-unsaturated fatty acids, most oxidized phospholipids are modified at the *sn*-2 position.<sup>26</sup>

### **Phospholipid Oxidation**

The term “oxidized phospholipids” was coined in 1939 by Fredrick and Mary Bernheim, who were investigating the catalytic effects of vanadium salts on phospholipid oxidation in heart and brain tissue.<sup>27</sup> Since the 1940s, studies on the mechanisms of lipid oxidation have been ongoing. Although there are various mechanisms for lipid oxidation, the most commonly referenced mechanism is the classic free-radical chain reaction that proceeds through three steps: initiation, propagation, and termination.<sup>28</sup> The first step, initiation, occurs when an initiator abstracts an electron from the unsaturated fatty acid moiety of a phospholipid. Initiators of phospholipid oxidation, summarized in a recent review article by Bochkov et al. and commonly referred to as reactive oxygen species (ROS), can be non-radical species (e.g., ozone ( $O_3$ ) or singlet oxygen ( $O_2^1$ )) or radical species (e.g., superoxide anion radical ( $O_2^{\cdot-}$ ) or hydroxyl radical ( $OH^{\cdot}$ )).<sup>1</sup> Furthermore, several catalysts of phospholipid oxidation have been reported including redox-active metals and ultraviolet (UV) light.<sup>29</sup> Once a hydrogen is abstracted from the unsaturated phospholipid, the carbon-centered radical ( $L^{\cdot}$ ) reacts with molecular oxygen to produce a lipid peroxy radical ( $LOO^{\cdot}$ ). The propagation step involves the subsequent reaction of the lipid peroxy radical with other unsaturated phospholipids in the cell membrane; thus, the reaction is self-propagating.<sup>29</sup> Although the overall lipid oxidation chain reaction is not expected to fully stop, “termination” is used to describe the event that occurs when radicals recombine or otherwise terminate to form non-radical products. Greater detail on the theoretical

aspects of lipid oxidation and generation of oxidized phospholipids in vivo is provided by Schaich<sup>29</sup> and Bochkov et al.,<sup>1</sup> respectively.

In vitro oxidation of phospholipids may be initiated through three pathways: enzymatic; non-enzymatic, free-radical; and non-enzymatic, non-radical. However, it is difficult to determine which method most accurately mimics the naturally occurring oxidation in living cells.<sup>30</sup> Enzymatic oxidation of phospholipids has been investigated using low-density lipoproteins and lipoxygenases.<sup>31-33</sup> Non-enzymatic, free radical oxidation has been studied using  $\text{H}_2\text{O}_2/\text{Fe}^{2+}$ ,  $\text{H}_2\text{O}_2/\text{Cu}^{2+}$ , or *t*-butylhydroperoxide to generate hydroxyl radicals.<sup>14</sup> Additionally, the non-enzymatic, free radical pathway has also been promoted by autoxidation, which involves the reaction of phospholipids with trace amounts of metals (e.g., iron) or phospholipid hydroperoxides.<sup>34</sup> Previous studies reporting non-enzymatic, non-radical oxidation have exposed phospholipids to singlet oxygen or ozone to produce lipid oxidation products.<sup>1,35</sup> For the experiments detailed in this work, autoxidation involving the exposure of unsaturated phospholipids to ambient air and light was used to promote oxidation of phospholipid standards. Furthermore, in vitro oxidation in tissue was catalyzed by UV light.

Following oxidative stress, many phospholipid oxidation products with varying structures and biological activities are formed.<sup>1,14</sup> These products are classified according to the nature of the modification: 1) long-chain products, formed by insertion of oxygen atoms; 2) short-chain products, formed by oxidative cleavage of the unsaturated fatty acid tails; and 3) phospholipid adducts, formed by reaction between oxidation products and/or molecules containing nucleophilic groups.<sup>14</sup> Additionally,

highly reactive degradation products of lipid peroxidation such as low molecular weight aldehydes (e.g., 4-hydroxynonenal and malondialdehyde) may be formed.<sup>26</sup>

In this work, the first two types of oxidation products, long-chain and short-chain, were investigated; examples of these products are shown in Figure 1-2. Due to the relatively high abundance in animal tissue,<sup>22</sup> PCs and PEs were the primary phospholipids investigated. Moreover, previous studies reported that most oxidized phospholipids detected in mammalian tissue contained a choline head group or, in the case of retina, an ethanolamine head group.<sup>26</sup>

### **Techniques for Measuring Phospholipid Oxidation**

Numerous techniques for the detection of phospholipid oxidation have been reported.<sup>36,37</sup> Biochemical assays, such as the thiobarbituric acid (TBA) assay,<sup>38</sup> have been widely used to study lipid oxidation, but these assays lack the selectivity needed for structural elucidation.<sup>36,39</sup> Another commonly used method for determining the extent of phospholipid oxidation is the measurement of diene conjugation by UV absorbance at  $\lambda = 234$  nm; however, this method also suffers from poor selectivity.<sup>36</sup> MS, which characterizes biomolecules based on mass-to-charge ratios ( $m/z$ ), has become increasingly important in phospholipid oxidation research.<sup>14</sup> Several studies have investigated phospholipid oxidation by gas chromatography (GC)-MS and liquid chromatography (LC)-MS; however, these methods require extraction and often derivatization.<sup>14,36</sup>

Most of the recent MS studies of oxidized phospholipids use electrospray ionization.<sup>14</sup> Although ESI has several advantages, such as the ability to be coupled to high-performance LC (HPLC), there are also many drawbacks. One limitation is that conventional ESI requires analytes to be in solution;<sup>40,41</sup> thus, direct analysis of intact

tissue is not possible. Furthermore, salts and other impurities found in the analyte solution may cause ion suppression in ESI.<sup>42</sup> These limitations can be overcome by matrix-assisted laser desorption/ionization, as it is not limited to analytes in solution and is also less sensitive to salts and other impurities found in complex sample matrices,<sup>39,43</sup> thus, MALDI is amenable to the analysis of intact biological tissue.<sup>44</sup> In terms of lipid oxidation studies, another important advantage of using MALDI is the minimal sample handling and preparation required, which reduces the likelihood of artifactual oxidation products.<sup>40, 43</sup>

The application of MALDI for lipid oxidation studies has been described previously; yet, in these experiments, MALDI is most often coupled to a time-of-flight (ToF) mass analyzer.<sup>14,45,46</sup> For the experiments described in this work, a linear ion trap (LIT) will be used as the mass analyzer. The primary advantage of the LIT is the MS<sup>n</sup> capabilities, which provide enhanced selectivity resulting in more reliable compound identification.<sup>43,47</sup> Furthermore, MALDI-LIT MS<sup>n</sup> is a powerful technique for mass spectrometric imaging of lipids<sup>48-50</sup> and, as shown in this work, lipid oxidation products.

### **Matrix-Assisted Laser Desorption/Ionization**

MALDI was first introduced by Karas and Hillenkamp in 1985.<sup>51</sup> Over the past 28 years, MALDI developed into an indispensable technique for MS analysis of labile and non-volatile molecules.<sup>43</sup> Since its introduction, MALDI has been widely used for the investigation of large biomolecules including peptides and proteins.<sup>43</sup> Recent developments in sample preparation, matrix selection, and applications of tandem mass spectrometry have revealed the utility of MALDI for the analysis of small molecules such as drugs, metabolites, and lipids.<sup>52,53</sup>

MALDI is a soft ionization technique (i.e., gas-phase ions are produced without extensive fragmentation) that uses a pulsed laser beam and a chemical matrix to generate gas-phase ions from both small and large molecules. The MALDI matrix typically consists of a small organic acid that has a strong molar absorptivity at the laser's wavelength, which is often in the UV region at  $\lambda = 337 \text{ nm}$ .<sup>43</sup> However, there is no single MALDI matrix or sample preparation protocol for MALDI MS analyses. Thus, the MALDI matrix solution and sample preparation methods must be developed for the analytes of interest.

### **Matrix Selection**

The view that selection of a proper matrix is critical in MALDI MS analysis is widely held and commonly cited.<sup>40,43,54</sup> In addition to strong absorptivity at the wavelength of the MALDI laser, an ideal matrix typically has a low vapor pressure, appropriate crystallization properties, and sufficient gas-phase acidity/basicity.<sup>54</sup> One of the most commonly used matrices for phospholipid analysis is 2,5-dihydroxybenzoic acid (DHB).<sup>43,55</sup> In addition, 2,4,6-trihydroxyacetophenone (THAP) is commonly used for the analysis of phospholipids and offers the advantage of fewer matrix background ions.<sup>45</sup> A lesser-known MALDI matrix, 6-aza-2-thiothymine (ATT), was recently evaluated for the analysis of oxidized phospholipids and was found to offer higher sensitivity and less fragmentation than either DHB or THAP.<sup>45</sup> The structures of these three matrices are illustrated in Figure 1-3.

Once a MALDI matrix is selected, parameters such as solvent systems and additives may then be optimized. When choosing a solvent system, the solubility of the MALDI matrix and the analyte should be considered. A proper solvent system should be capable of dissolving the analyte and also allow for a saturated solution of MALDI

matrix.<sup>56</sup> Additionally, solvent systems should have sufficiently high vapor pressure to facilitate rapid evaporation and the formation of a microcrystalline film.<sup>56</sup>

Furthermore, several studies have illustrated the utility of adding salts (e.g., lithium acetate, potassium acetate, or sodium acetate) to MALDI matrix solutions for improving sensitivity, reducing spectral complexity, and enhancing the structural analysis of lipids by MALDI MS<sup>n</sup>.<sup>57,58</sup> One recent investigation by Griffiths and Bunch demonstrated that not only cation choice, but also salt type (e.g., acetates, chlorides, or nitrates) and concentration, impacted spectral results.<sup>58</sup> Thus, the selection of an additive should also be an important consideration for optimizing MALDI experiments.

For MS<sup>n</sup> and imaging of the OxPLs investigated in this work, no significant differences in performance of DHB, THAP, and ATT were observed. Given that DHB was far less expensive than either ATT or THAP, DHB was the primary MALDI matrix used in these studies. However, for analysis of low abundant, endogenous lipid oxidation products, ATT may be a more suitable matrix. Regarding solvent selection, this work used solvents including methanol, water, and chloroform. Lastly, sodium acetate was added to the matrix solutions used in this work because enhanced structural information was obtained from the sodium adducts of OxPLs.

### **MALDI Process**

For MALDI MS analysis, the analyte solution and an excess of matrix are typically pipetted onto a stainless steel MALDI target plate.<sup>43</sup> As the solvent evaporates, the matrix and analytes co-crystallize. The sample plate is then inserted into the mass spectrometer and rastered beneath a pulsed laser beam. When the laser strikes the sample surface, matrix–analyte co-crystals are desorbed into the gas phase plume consisting of positive ions, negative ions, and neutrals (Figure 1-4).

The ionization process of MALDI is still under investigation; however, two theories for ion formation in MALDI have been proposed: the lucky survivor model<sup>59,60</sup> and the gas-phase protonation model.<sup>61,62</sup> The lucky survivor model proposes that analytes retain their respective charge states from solution when they are incorporated into the matrix–analyte co-crystals. Following desorption, ions that are not neutralized in the plume are detected and are so-called “lucky survivors”.<sup>59</sup> In contrast, the gas-phase protonation model postulates that neutral analytes undergo gas-phase collisions with protonated  $[ma+H]^+$  or deprotonated  $[ma-H]^-$  matrix leading to proton transfer and the detection of protonated  $[A+H]^+$  or deprotonated  $[A-H]^-$  analyte.<sup>61</sup> Recently, evidence supporting both of these ionization pathways led to a unified model that combines the lucky survivor and gas-phase protonation theories.<sup>63</sup>

### **Instrumentation**

In this work, the primary instrument used was the Thermo Scientific MALDI LTQ XL (San Jose, CA). A schematic of this instrument is displayed in Figure 1-5. The MALDI source is composed of an optics module and sample module. The optics module contains a stationary 60-Hz N<sub>2</sub> laser ( $\lambda = 337$  nm) and optics, which include lenses, mirrors, and neutral density filters that focus, direct, and attenuate the laser beam as needed prior to reaching the sample target. This module is also equipped with a charge-coupled device (CCD) camera that captures optical images of the sample inside the instrument and provides a real-time view of the sample during analysis. The sample module transfers the sample plate from atmospheric pressure to intermediate pressure (75 mTorr) and moves the sample target in the xy-plane relative to the laser. Ion optics for transferring ions to the MS detector are also contained within the sample module.<sup>64</sup>

Following ionization in the MALDI source, ions are transmitted to the mass analyzer via a series of ion optics. The ions first pass through a square array of square-profile rods, the Q00 quadrupole. Next, the ions are transmitted through the Q0 quadrupole and the Q1 octopole and into the mass analyzer, which on this instrument is a linear ion trap (LIT).

### **Linear Ion Trap**

In the Thermo LTQ XL, the LIT mass analyzer is the site of storage, isolation, dissociation, and ejection of ions.<sup>64</sup> As depicted in the schematic in Figure 1-6, the two-dimensional LIT is composed of a rectangular array of hyperbolic-profile rods, which are divided into three sections: front, center, and back.<sup>65</sup> The front and back sections are 12 mm in length, whereas the center section is 37 mm in length with 30-mm × 0.25-mm ejection slits in the two x-axis rods. To account for field imperfections due to these slits, the x-axis rods are spaced farther apart (9.5 mm) than the y-axis rods that are 8 mm apart.<sup>66</sup>

Ions are trapped in stable orbits within the center-section by a time-varying radiofrequency (RF) electric field that is applied to opposite pairs of rods.<sup>67</sup> The stability of ions in a LIT is governed by the solutions (Equations 1-1 and 1-2) to a set of non-linear equation known as the Mathieu equations.<sup>67</sup>

$$a_x = \frac{8eU}{mr_0^2\Omega^2} \quad (1 - 1)$$

$$q_x = \frac{-4eV}{mr_0^2\Omega^2} \quad (1 - 2)$$

In these equations,  $e$  is the electronic charge of the ion,  $U$  is the applied DC potential,  $V$  is the applied AC potential,  $m$  is the mass of the ion,  $r_0$  is the radius of an inscribed circle of the rod array, and  $\Omega$  is the angular frequency.<sup>67</sup>

Ions have stable trajectories inside the trap when they are at  $a_x$ ,  $q_x$  values that fall within the shaded portion of the Mathieu stability diagram (Figure 1-7).<sup>65</sup> However, mass analysis in the LIT is performed by mass-selective instability scanning, whereby the LIT is operated in RF-only mode (i.e.,  $U = 0$  and, therefore,  $a_x = 0$ ); thus, allowing for the expression of ion stability in terms of  $q_x$  only. After trapping, mass analysis is performed by linearly increasing the amplitude of the RF potential and simultaneously applying a resonance excitation voltage across the two x-electrodes. As the resonance excitation frequency reaches the secular frequency of a specific  $m/z$ , the ions at this  $m/z$  value are radially ejected through the slits in the two center-section rods.<sup>66</sup> Although not shown in Figure 1-5, ions radially ejected from the LIT strike one of two conversion dynodes on either side of the LIT creating secondary charged particles, that are then detected by electron multipliers.<sup>64</sup> The current on the multipliers is amplified and then the on-board data acquisition computer synchronizes the time of the ions' ejection to the current to produce a mass spectrum.

In single-stage full-scan mode (MS), ions are stored in the LIT and sequentially scanned out of the ion trap by mass-selective instability to produce a mass spectrum.<sup>64</sup> MS spectra yield profiles of ions within a given sample and are ideal for initial comparison of two data sets (e.g., control vs diseased). Additionally, one of the primary advantages of the LIT mass analyzer is the MS<sup>n</sup> capabilities, which allow for enhanced selectivity and structural information. In contrast to many other tandem mass analyzers

(e.g., ToF-ToF or QqToF) that can only perform up to two stages of mass analysis, the LIT can perform up to 10 stages of mass analysis.

### **Tandem Mass Spectrometry**

Tandem mass spectrometry ( $MS^n$ ) is a valuable technique for characterizing phospholipids, allowing for the elucidation of phospholipid structure and differentiation of isobaric species.<sup>68</sup> Although  $MS^n$  can be performed on a number of mass analyzers, this work will focus on  $MS^n$  in ion traps. Once in the ion trap, ions within a certain  $m/z$  range can be isolated and then fragmented by ion activation methods, the most common of which is collision-induced dissociation (CID).<sup>69</sup> CID occurs by a two-step mechanism involving excitation and fragmentation of precursor ions.<sup>69</sup> First, the mass-selected precursor ions are excited by an applied resonant excitation voltage. As these ions gain translational energy inelastic collisions occur between the ions and the helium damping gas resulting in the transfer of part of the ions' kinetic energy into internal energy. Second, fragmentation occurs when the precursor ions gain enough internal energy to dissociate into one or more product ions and neutrals.<sup>69</sup> These product ions are stored and then ejected from the trap in order of increasing  $m/z$  by linearly increasing the main RF voltage and applying a supplementary resonant ejection voltage, which is used to improve mass resolution in the LIT.<sup>66</sup> The result of this technique is a product-ion ( $MS^2$ ) spectrum consisting of fragment ions from the mass-selected precursor ion as shown in Figure 1-8.

During storage of the  $MS^2$  product ions, but prior to scan-out, a product ion can be isolated and further fragmented by CID ( $MS^3$ ).<sup>43</sup> Assuming sufficient isolation and fragmentation efficiency, with each additional stage of MS selectivity is gained and enhanced structural information is often attained. For the identification of phospholipid

oxidation products in this dissertation, multiple stages of MS (up to MS<sup>4</sup>) were used. MS<sup>n</sup> is also applicable to mass spectrometric imaging (MSI) experiments; thus, images of product ions can be generated allowing the spatial distributions of isobaric ions to be differentiated.<sup>70</sup>

### **Mass Spectrometric Imaging**

MSI has emerged as a powerful technique for investigating regional distributions of specific lipids in biological tissues<sup>71</sup> including brain,<sup>68,72</sup> heart,<sup>50</sup> lung,<sup>73</sup> and spinal cord.<sup>48</sup> This technique, which has been the subject of several recent review articles,<sup>44,74,75</sup> combines the multichannel (*m/z*) measurement capabilities of mass spectrometers with surface sampling methods (e.g., MALDI) that allow for retention of spatially-resolved chemical distributions.<sup>76</sup> Furthermore, MSI data can be correlated to anatomical structures in tissues, which may offer insight into a number of complex biochemical processes that occur within living organisms.<sup>76</sup>

In MSI experiments, thin tissue sections are directly interrogated in a distinct pattern so that the spatial distributions of target compounds within the tissue section may be observed.<sup>43,70</sup> Figure 1-9 illustrates the typical MSI workflow. MSI experiments are performed by first sectioning the frozen tissue on a cryostat (temperature of ca. -25 °C) into thin (10–20 μm) sections. For applications outside of MS, such as histology, the tissue sample is usually affixed to the sample stage using an optimal cutting-temperature medium (OCT); however, OCT is formulated from water-soluble glycols and resins and typically contains a number of compounds, such as benzalkonium chloride, that can interfere with mass spectrometric analysis.<sup>77,78</sup> Therefore, for MSI analysis, HPLC-grade water is often used to freeze the tissue to the sample stage.

Once cut, the frozen tissue sections are transferred onto a cold MALDI target surface that is usually a glass or conductive glass microscope slide or, in some cases, a metal surface such as stainless steel.<sup>79</sup> Sections are then thaw-mounted by localized warming of the tissue by placement of a gloved finger on the back side of the MALDI target, causing the tissue to adhere to the target surface. Once collected, the tissue sections on the MALDI target are dried (ca. 30 min) in a vacuum desiccator and coated with MALDI matrix. Various techniques for depositing matrix atop tissue samples for MSI have been reported including dry-powder coating,<sup>80</sup> electrospray deposition,<sup>77,81</sup> inkjet printing,<sup>82</sup> pneumatic spraying,<sup>77,83</sup> and sublimation.<sup>84</sup> Next, the tissue is rastered with respect to the laser in a predefined, equal step-size pattern. At each spot where the tissue is irradiated, a mass spectrum is recorded along with its relative position. Once the data are acquired, imaging software is employed to extract and display the intensity of individual ions as a function of position.<sup>85</sup>

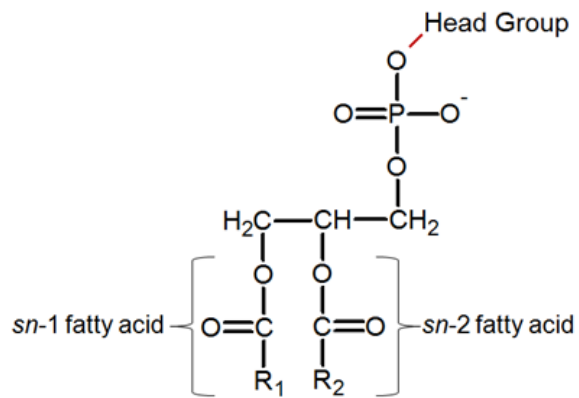
### **Overview of Dissertation**

To better understand phospholipid oxidation and the involvement of oxidation products in the development and progression of disease, methods for identifying these products in biological samples must be developed. The purpose of this research was to utilize MALDI MS<sup>n</sup> to develop such methods. In the following chapters, MS<sup>n</sup> is used as a selective method for characterizing, identifying, and imaging phospholipid oxidation products.

Chapter 2 details the MS<sup>2</sup>, MS<sup>3</sup>, and MS<sup>4</sup> fragmentation pathways of various PC oxidation products and identifies structurally informative product ions. This chapter illustrates the utility of the MS<sup>n</sup> capabilities on the LIT for providing enhanced selectivity, which will be important for detection of these low-abundance oxidation products in

complex biological samples. Chapter 3 describes the use of MALDI MS<sup>n</sup> for identifying PE oxidation products following autoxidation of unsaturated PE standards. Various structurally informative product ions were discovered that allowed for confirmation of oxidative modification to the *sn*-2 fatty acid substituent. Furthermore, key differences in the fragmentation of OxPE aldehyde and carboxylic acid derivatives are discussed. In Chapter 4, principal component analysis and MALDI MS<sup>n</sup> imaging were combined to identify and localize lipid oxidation products in spinal cord tissue following *in vitro* oxidation. This chapter illustrates the potential of the MALDI MS<sup>n</sup> methodologies developed in this work for identifying and imaging lipid oxidation products in tissue from animal models of oxidative stress, injury, or disease. Lastly, Chapter 5 provides conclusions to the work presented within this dissertation and insight into future experiments that could expand upon this work to further the understanding of the biological roles of phospholipid oxidation products in human health and disease.

## Glycerophospholipids (GPLs)



## Head Groups

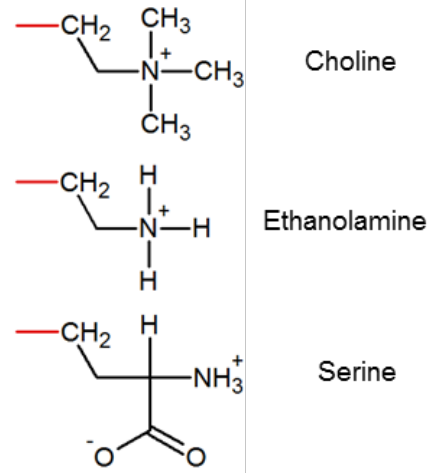
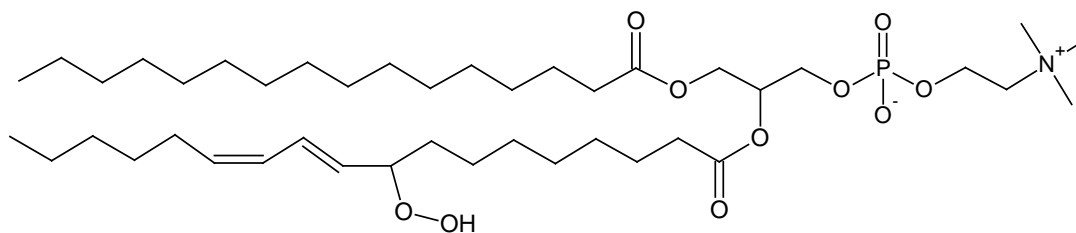


Figure 1-1. Glycerophospholipid structure and select head groups.

### Long-Chain Oxidation Product



### Short-Chain Oxidation Product

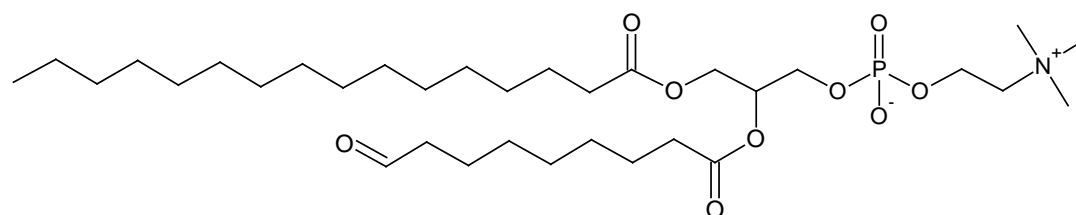
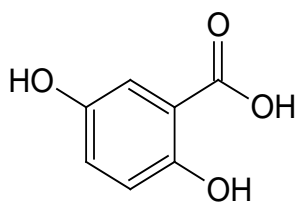
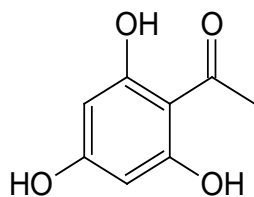


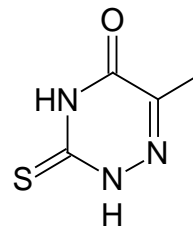
Figure 1-2. Two types of phospholipid oxidation products investigated in this work.



DHB  
MW=154.12



THAP  
MW=168.15



ATT  
MW=143.16

Figure 1-3. Structures of the three MALDI matrices evaluated for the analysis of oxidized phospholipids.<sup>45</sup>

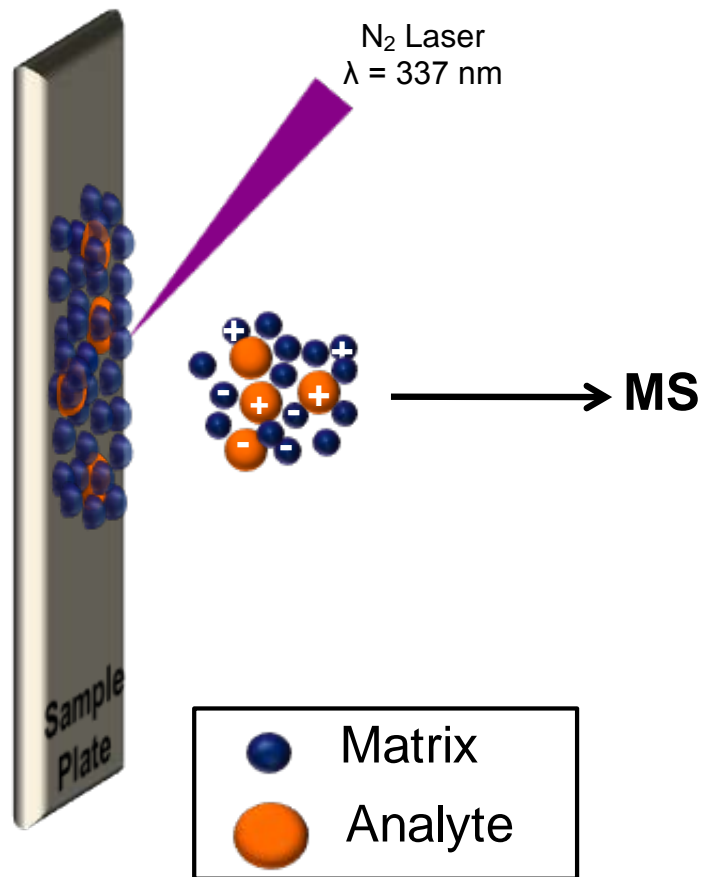


Figure 1-4. Schematic of the MALDI process. Adapted from Chughtai et al.<sup>44</sup>

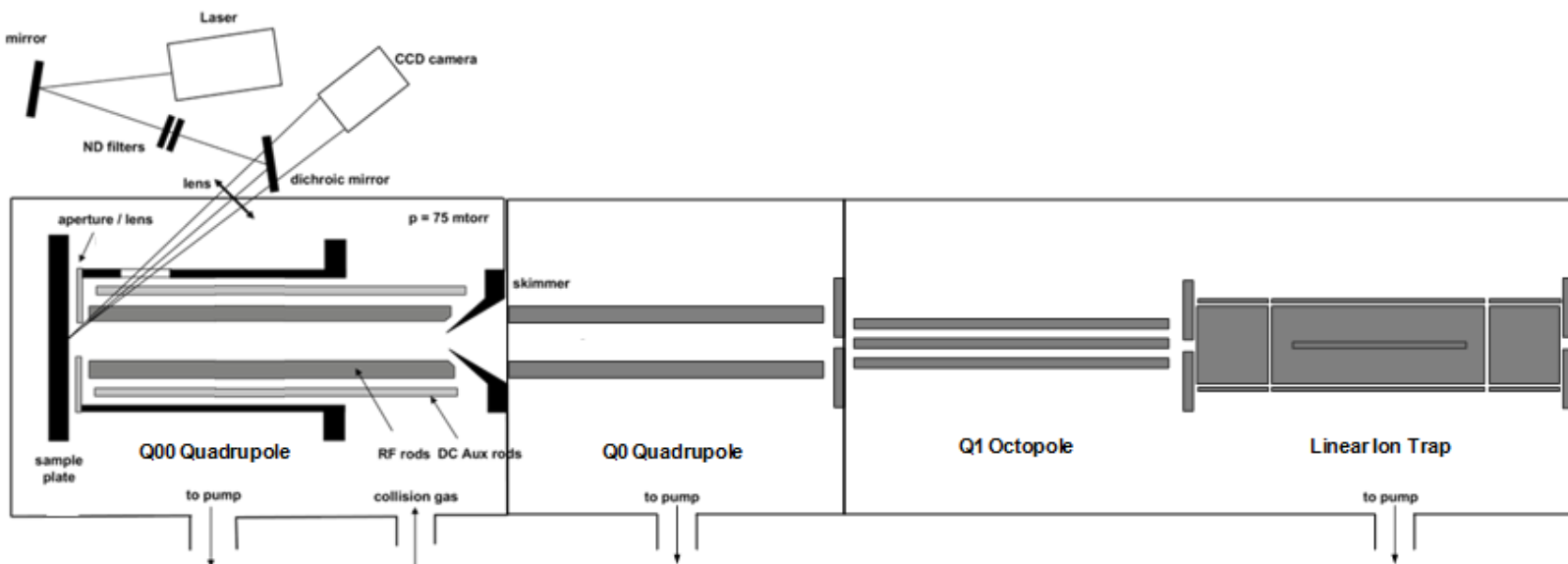


Figure 1-5. Schematic of the Thermo Scientific MALDI LTQ XL used in this work. Adapted from Strupat et al.<sup>86</sup> and Garrett et al.<sup>68</sup>

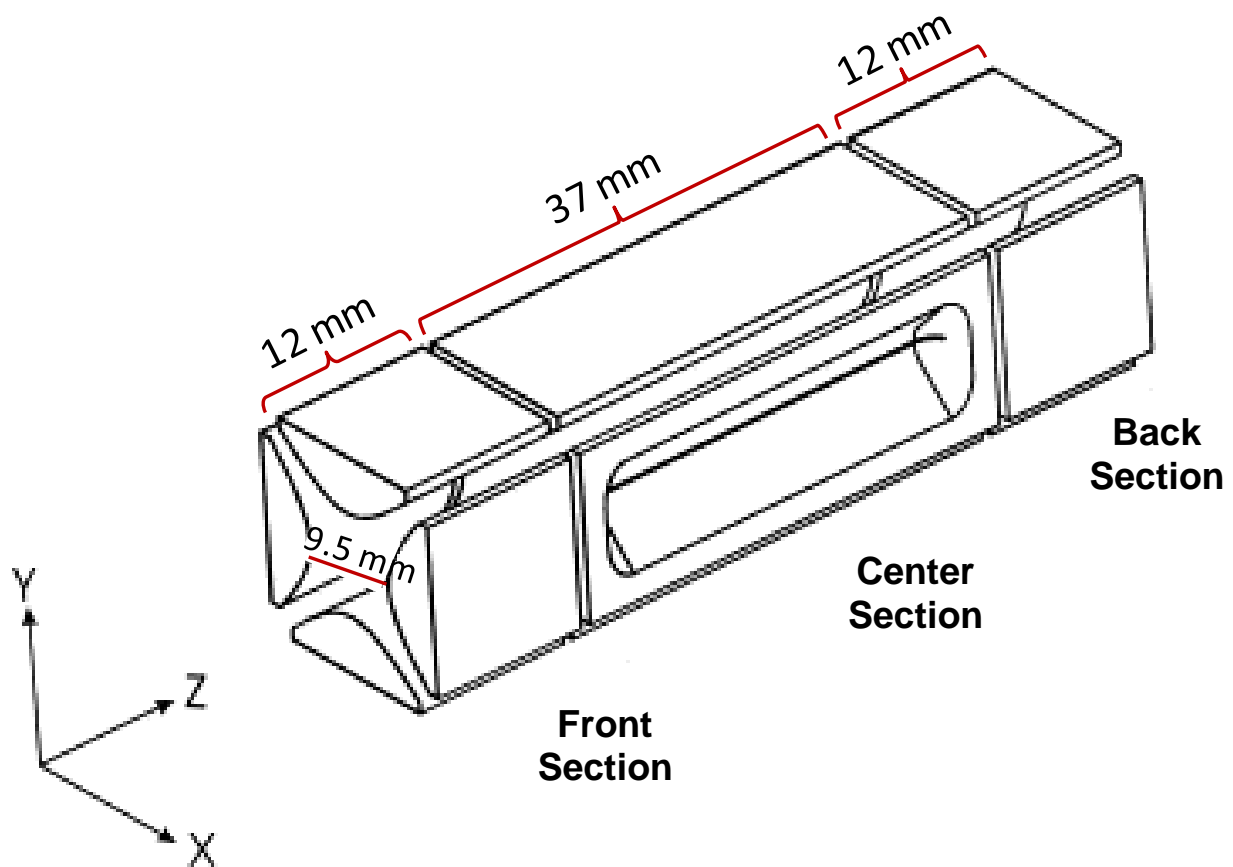


Figure 1-6. Schematic of the two-dimensional LIT adapted from Schwartz et al.<sup>66</sup> Ions transmitted through the front section along the z-axis and are trapped in the center section by DC axial trapping and RF radial trapping.

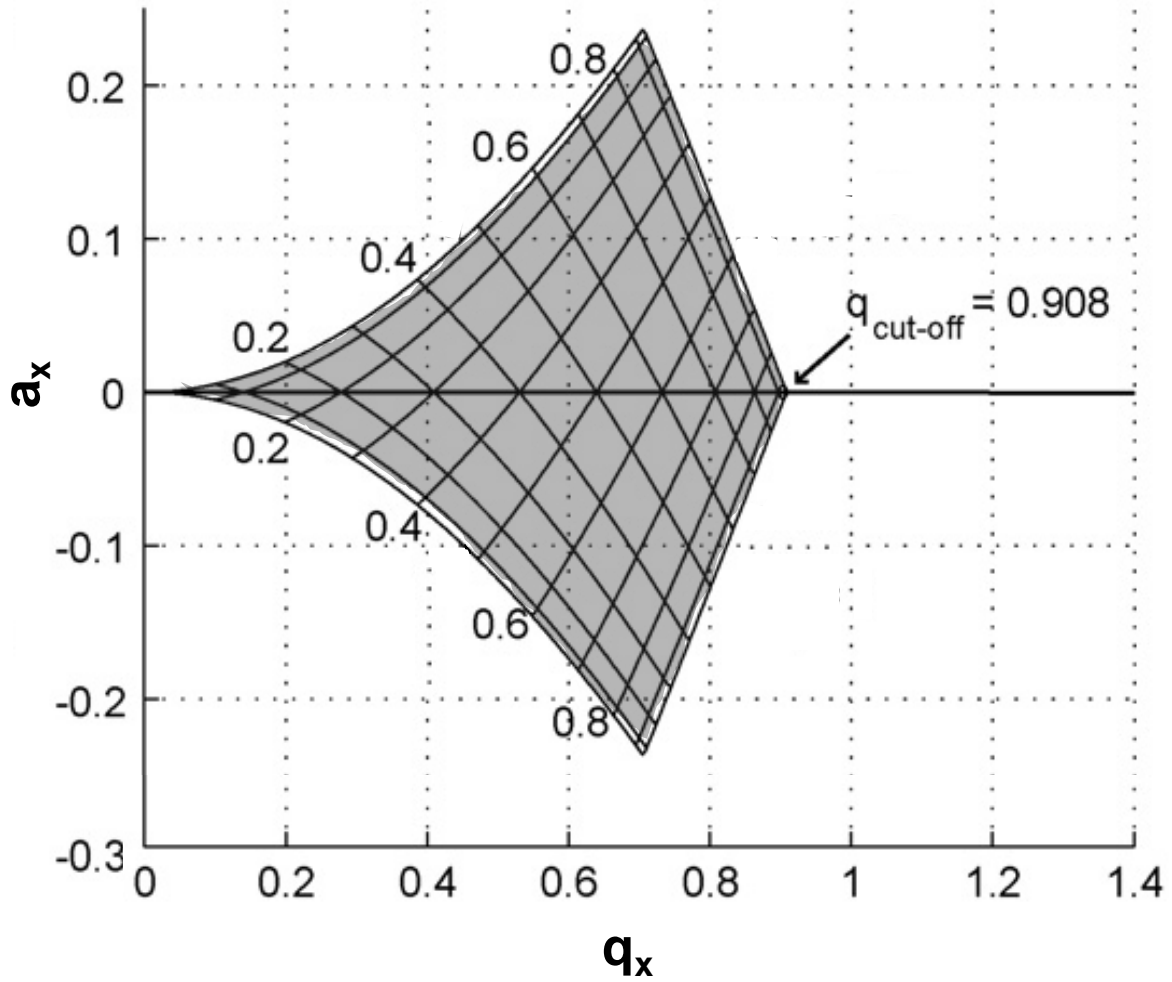


Figure 1-7. Mathieu stability diagram of the two-dimensional LIT. Since LITs are typically operated in RF-only mode ( $a_x = 0$ ), ions are successfully trapped along the  $q_x$  axis with a low-mass cut-off (LMCO)  $q_x = 0.908$ . Adapted from Krishnaveni et al.<sup>65</sup>

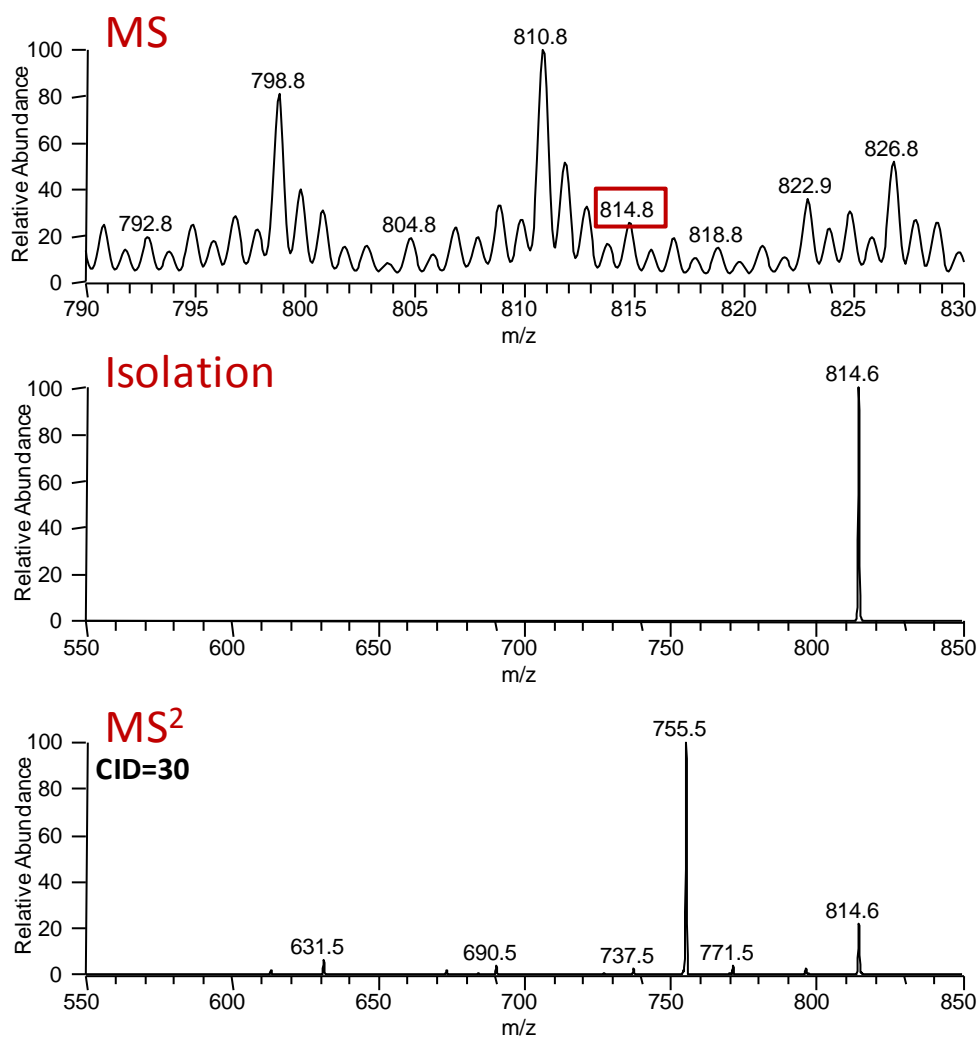


Figure 1-8. Sample mass spectra illustrating an MS<sup>2</sup> experiment. First, precursor ions of a chosen  $m/z$  value are selected for MS<sup>2</sup> analysis (top). Next, the precursor ions at this  $m/z$  are isolated (middle) and CID is applied to produce the MS<sup>2</sup> product-ion spectrum (bottom).

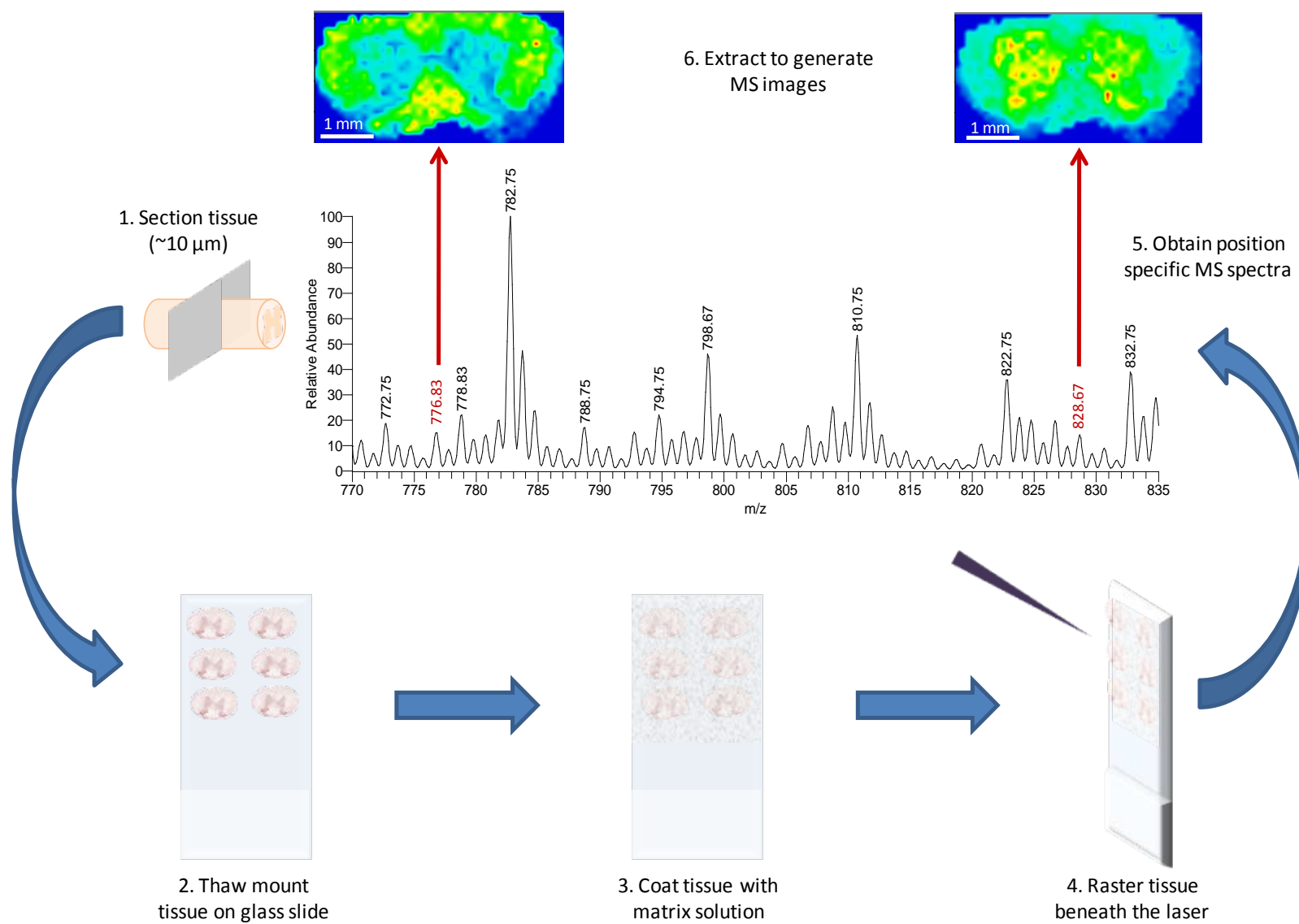


Figure 1-9. Mass spectrometric imaging (MSI) workflow.

## CHAPTER 2 CHARACTERIZATION OF PHOSPHATIDYLCHOLINE OXIDATION PRODUCTS BY MALDI MS<sup>n</sup>

### Introduction

Lipid oxidation has been implicated in the pathogenesis and/or progression of various human disorders and diseases including Alzheimer's,<sup>2-4</sup> age-related macular degeneration,<sup>5</sup> atherosclerosis,<sup>5,6</sup> cataractogenesis,<sup>5</sup> multiple sclerosis,<sup>7</sup> and rheumatoid arthritis.<sup>8</sup> Probing lipid oxidation has proved challenging for a number of reasons, including the diversity of oxidation products, the instability of select oxidation products, and the sensitivity necessary to detect these oxidation products.<sup>87</sup> Furthermore, several studies have illustrated the various important biological activities of lipid oxidation products and have shown that many of these activities (e.g., inflammatory vs anti-inflammatory) are dependent on the specific chemical structure of the oxidized species;<sup>88</sup> the type of modification to the *sn*-2 substituent (terminal carboxylic acid vs terminal aldehyde), the chemical bond linking the *sn*-1 substituent (ether vs ester), the fatty acid chain length, and the charge on the head group have all been shown to affect the biological activities of lipid oxidation products.<sup>88-92</sup> Thus, there is growing interest in developing methods for characterizing and identifying lipid oxidation products in biological samples.<sup>28</sup>

Biochemical assays, such as the thiobarbituric acid (TBA) assay,<sup>38</sup> have been widely used to detect total lipid oxidation; however, these assays lack the selectivity needed for structural elucidation.<sup>39</sup> Diene conjugation, measured by UV absorbance at 234 nm, has also been utilized to determine the extent of lipid oxidation, but this method also suffers from poor selectivity.<sup>39</sup> Mass spectrometry (MS) has become increasingly utilized in lipid oxidation research due to the ability to characterize biomolecules based

on their mass-to-charge ( $m/z$ ) ratios, yielding superior selectivity relative to the aforementioned techniques.<sup>1,14,15</sup> Despite the various challenges, several MS methods have been developed for the analysis of the oxidatively modified phospholipids (OxPLs). Gas chromatography-mass spectrometry (GC-MS) and liquid chromatography-mass spectrometry (LC-MS) have been used for identification and quantitation of phospholipid oxidation products;<sup>93-98</sup> however, many of these methods require hydrolysis of the oxidized free fatty acid moieties from the phospholipid head group and extensive derivatization prior to analysis.

More recently, soft ionization methods have been employed for the analysis of OxPLs without derivatization.<sup>30,99-108</sup> Electrospray ionization mass spectrometry (ESI MS) combined with reversed-phase high-performance liquid chromatography (RP-HPLC) has become the most widely used method for the analysis of OxPLs.<sup>15</sup> This method offers several advantages. First, OxPLs readily ionize by ESI and RP-HPLC offers chromatographic separation based on fatty acid composition. Second, these methods are amenable to tandem mass spectrometry ( $MS^n$ ), though in most cases only two stages of MS (i.e.,  $MS^2$ ) have been performed.<sup>14,15</sup> Matrix-assisted laser desorption/ionization (MALDI) has also been used to investigate OxPLs,<sup>16</sup> but few published studies have used this ionization method in spite of the many inherent advantages.<sup>45</sup> In comparison to LC coupled with ESI MS, MALDI MS requires less sample and offers more rapid analysis. Furthermore, MALDI is less sensitive to salts and other impurities found in complex biological samples;<sup>39</sup> in fact, addition of salts is often advantageous for the structural elucidation of various phospholipids by MALDI

MS<sup>n</sup>.<sup>49,50,68,106</sup> Additionally, MALDI can be coupled to mass spectrometric imaging (MSI) techniques for in situ detection and localization of PLs in biological tissues.<sup>13,48-50</sup>

This investigation characterized oxidation products of phosphatidylcholines, the most abundant phospholipids in cell membranes,<sup>109</sup> by MALDI MS<sup>n</sup> using a linear ion trap (LIT) mass analyzer. The MS<sup>n</sup> (where n = 2, 3, or 4) capabilities of the LIT were exploited for enhanced selectivity resulting in more reliable characterization of the collision-induced dissociation (CID) fragmentation pathways of OxPCs. Additionally, preliminary results illustrate the utility of the developed MALDI MS<sup>n</sup> method for identifying and imaging these OxPCs in biological tissues.

## **Experimental Methods**

### **Chemicals**

Avanti Polar Lipids (Alabaster, AL) was the source for all lipid standards except 1-(palmitoyl-2-(5-keto-6-octene-dioyl)-*sn*-glycero-3-phosphatidylcholine (KOdiAPC), which was purchased from Cayman Chemical (Ann Arbor, MI). MALDI matrix, 2,5-dihydroxybenzoic acid (DHB), was purchased from Acros Organics (Geel, Belgium). Sodium acetate trihydrate (NaOAc) and HPLC-grade water and methanol were purchased from Fisher Scientific (Fair Lawn, NJ). Ethanol (200 proof) was purchased from Decon Labs (King of Prussia, PA).

### **Preparation of OxPC Standards**

The short-chain oxidation product (OxPC) standards listed in Table 2-1 were dissolved in cold, degassed ethanol to a concentration of 100 ppm. A MALDI matrix solution consisting of 40 mg/mL DHB in 70:30 methanol:water (v/v) and 10 mM NaOAc (final concentration) was prepared. Sodium acetate was added to enhance the relative intensity of the [M+Na]<sup>+</sup> ions, which yielded more structurally informative fragmentation.

OxPC standards were deposited atop a 384-well stainless steel MALDI plate using a modified dried-droplet method.<sup>12</sup> For this method, 1  $\mu\text{L}$  of the 100 ppm OxPC standards followed by 1  $\mu\text{L}$  of MALDI matrix were pipetted into the sample wells. The solvent was allowed to evaporate in ambient air, resulting in matrix/analyte co-crystals.

### **Preparation of Spinal Cord Tissue**

To illustrate the potential for identification and MSI of OxPCs, spinal cord tissue from the lumbar region of adult, female Sprague-Dawley rats (Harlan, San Diego, CA) was utilized. Animal studies were approved by the local IACUC at the University of California, San Diego, and were performed in an AAALAC-approved vivarium. Following euthanasia, excised tissue was immediately flash-frozen in liquid nitrogen and stored at  $-80\text{ }^{\circ}\text{C}$  until further use. Tissue was sectioned at  $-25\text{ }^{\circ}\text{C}$  using a Microm HM 505E cryostat (Walldorf, Germany). To avoid analyte ion suppression resulting from tissue mounting media (e.g., optimal cutting-temperature polymer),<sup>77</sup> spinal cord tissue was fused to the cutting stage using HPLC-grade water. Cross-sections (10  $\mu\text{m}$  thick) were thaw-mounted atop cold glass microscope slides and subsequently dried in a vacuum desiccator for approximately 30 min to remove excess water. The slides were then spray coated with MALDI matrix using a glass Type A Meinhard nebulizer (Golden, CO) and nitrogen (30 PSI) as the nebulizing gas. Matrix was applied until a homogenous layer of matrix–analyte co-crystals was observed over the entire tissue.

### **MALDI MS Instrumentation**

Mass spectra were acquired in positive ion mode using an intermediate-pressure (70 mTorr) MALDI-LIT mass spectrometer, a Thermo Scientific MALDI LTQ XL (San Jose, CA). This instrument was equipped with a 337-nm nitrogen laser with a 60-Hz repetition rate and 100  $\mu\text{m}$  laser spot diameter. Laser energies of 2.0–8.0  $\mu\text{J}$  per laser

shot and 3–4 laser shots per raster spot were used in these experiments; automatic gain control (AGC) was toggled off. For MSI experiments, images were generated using Thermo ImageQuest 1.0.1 software (San Jose, Ca). Mass spectral images generated following one stage of mass analysis (MS) were normalized to the total ion current (TIC). For images generated from higher stages of mass analysis, the intensity of the most abundant product ion was plotted at each pixel and was not normalized to TIC. For all other data processing, Thermo QualBrowser 2.0.7 (San Jose, Ca) was used.

### **MS<sup>n</sup> Instrumental Parameters**

For MS<sup>2</sup> experiments, a precursor ion isolation width of 1.2 u was utilized. For MS<sup>3</sup>, the precursor ion isolation widths for the first and second isolation events were adjusted to 1.5 and 2.0 u, respectively. Lastly, for MS<sup>4</sup>, isolation widths of 1.5, 2.0, and 2.5 u were utilized for the first, second, and third isolation events, respectively. Each mass spectrum presented represents an average of 100 analytical scans, unless otherwise noted.

MS<sup>2</sup>, MS<sup>3</sup>, and MS<sup>4</sup> experiments were performed using CID. Collision energies were optimized to achieve maximum product ion intensity. In general, the precursor ion was depleted to <20% of the most intense fragment ion; however, without exception, the precursor ion was detected above the baseline. For precursor ions with higher  $m/z$  values (greater than  $m/z$  599), the  $q$  of activation ( $q_{act}$ ) was reduced to 0.22 (typically  $q_{act}$  = 0.25 on the LTQ XL), when necessary, to decrease the low-mass cutoff (LMCO). Specifically, the LMCO was decreased to observe the product ion at  $m/z$  184 for protonated OxPCs.

## Accurate Mass Measurements

To validate several proposed fragmentation pathways and product ion identifications, accurate mass measurements were performed using a 7-T hybrid LIT-Fourier transform ion cyclotron resonance (FTICR) mass spectrometer, the Finnigan LTQ FT (Thermo Fisher Scientific, Bremen, Germany). This instrument was equipped with a Thermo Scientific nanospray ionization (NSI) source. For these experiments, OxPC standards diluted to 1000 nM in ethanol were directly infused at a flow rate of 0.5  $\mu\text{L}/\text{min}$ , and the NSI spray voltage was set to +2 kV. The heated capillary on the LTQ was held at +39 V and 200  $^{\circ}\text{C}$ .  $\text{MS}^n$  isolation and excitation were performed in the LIT, whereas mass analysis of the product ions was conducted in the ICR cell. AGC was toggled on for all experiments with a maximum injection time of 100 ms. For  $\text{MS}^n$  experiments on the LTQ FT, the parameters for precursor ion isolation widths were the same as those outlined above, with the exception of the third isolation event in  $\text{MS}^4$ , which was lowered from 2.5 to 2.0 u. Additionally, collision energies were optimized as described above. The FT portion of the instrument was operated in wide scan mode at a resolving power of 100,000 with 50 analytical scans averaged to obtain accurate mass values.

## Results and Discussion

Ionization of unmodified PCs by MALDI produces both protonated species,  $[\text{M}+\text{H}]^+$ , and alkali metal adducts such as  $[\text{M}+\text{Na}]^+$ .<sup>14</sup> Depending on the precursor ion selected, the fragmentation pathways observed by  $\text{MS}^2$  vary greatly.<sup>47</sup> In contrast to the  $[\text{M}+\text{H}]^+$  ions of unmodified PCs, which yield one predominant  $\text{MS}^2$  product ion ( $m/z$  184) and little structural information, CID of the  $[\text{M}+\text{Na}]^+$  ions yields many structurally informative product ions.<sup>68,110</sup> In this work, MALDI MS utilizing DHB as a positive-mode

matrix produced both protonated and sodiated ions of OxPCs. Subsequently, the fragmentation pathways of the  $[M+H]^+$  and  $[M+Na]^+$  ions were explored for each of the OxPCs listed in Table 2-1.

### **MS<sup>2</sup> Characterization of the $[M+H]^+$ Ions of Short-Chain OxPCs**

The observed MS<sup>2</sup> product ions resulting from CID of the  $[M+H]^+$  ions of PAzPC, PONPC, PGPC, POVPC, and KOdiAPC are listed in Table 2-2. Many of these product ions are in accordance with the ESI MS<sup>2</sup> fragmentation of  $[M+H]^+$  ions of 1-palmitoyl-2-linoleoyl-*sn*-glycero-3-phosphocholine (PLPC) and 1-palmitoyl-2-arachidonoyl-*sn*-glycero-3-phosphocholine (PAPC) oxidation products reported by Reis et al.<sup>104</sup> Similar to unmodified PCs, following CID of the  $[M+H]^+$  ion, short-chain OxPCs yielded a dominant product ion at  $m/z$  184, corresponding to the protonated phosphocholine head group ( $[H_2PO_4(CH_2)_2N(CH_3)_3]^+$ ).<sup>111,112</sup> Although much lower in abundance (0.5–4% relative abundance), the product ions corresponding to the neutral losses (NLs) of the fatty acid moieties, as free acids or as ketenes, were also observed. These product ions were reported previously in ESI MS<sup>2</sup> studies of unmodified PCs and allowed for differentiation of positional isomers based on the relative abundances of the *sn*-1 and *sn*-2 ketene losses; the product ion corresponding to the *sn*-2 ketene NL ( $-R_2=C=O$ ) demonstrated greater abundance than the product ion due to the *sn*-1 ketene NL ( $-R_1=C=O$ ).<sup>112</sup> This trend was also observed for all short-chain OxPCs studied in this work; that is, the loss of the saturated *sn*-1 ketene was, in all cases, less abundant than the loss of the oxidized *sn*-2 ketene. Furthermore, the modified *sn*-2 fatty acid chain was preferentially lost as the ketene ( $-R_2'=C=O$ ) while the *sn*-1 fatty acid chain was preferentially lost as the free acid ( $-R_1COOH$ ).

As a specific example, Figure 2-1 illustrates these fragmentation pathways for MS<sup>2</sup> of the [M+H]<sup>+</sup> ion of PAzPC (*m/z* 666). The product ion corresponding to the phosphocholine head group, *m/z* 184, was the base peak; all other product ions were observed below 2% relative abundance. Upon 20× magnification of the upper mass region of the spectrum (greater than *m/z* 184), product ions related to the fatty acid tails were observed. The losses of the *sn*-2 tail as the ketene (NL of 170 u) and as the free acid (NL of 188 u), although lower in abundance, were observed at *m/z* 496 and 478, respectively. Likewise, losses of the *sn*-1 tail as the ketene and as the free acid were observed at *m/z* 428 and 410, respectively; however, the *sn*-1 tail was preferentially lost as the free acid instead of the ketene. The trend mentioned above for the relative abundance of the *sn*-1 ketene loss and the *sn*-2 ketene loss is also illustrated in the MS<sup>2</sup> product ion spectrum of *m/z* 666; that is, the ion corresponding to the *sn*-2 ketene loss (*m/z* 496) was greater in abundance than that of the *sn*-1 ketene loss (*m/z* 428).

Although structural information may be obtained from CID of the [M+H]<sup>+</sup> ions, the majority of the product ion intensity falls at *m/z* 184, a structurally uninformative fragment ion with regards to the substituents bound to the *sn*-1 and *sn*-2 positions of the glycerol backbone. Thus, fragmentation of the [M+H]<sup>+</sup> ion presents a relatively inefficient method for determining fatty acid composition and position. Accordingly, the fragmentation pathways related to the [M+Na]<sup>+</sup> ions of OxPCs were explored.

### **MS<sup>n</sup> Characterization of the [M+Na]<sup>+</sup> Ions of Short-Chain OxPCs**

The MS<sup>n</sup> product ion spectra of the short-chain products studied illustrated distinct fragmentation patterns for the [M+Na]<sup>+</sup> ions. For each of the OxPCs, the MS<sup>2</sup> product ions resulting from CID of the [M+Na]<sup>+</sup> precursor ions are listed in Table 2-3.

Many of these product ions are in agreement with ESI MS<sup>2</sup> product ions previously observed following CID of PLPC and PAPC oxidation products.<sup>104</sup> Characteristic MS<sup>2</sup> fragmentation resulting in product ions produced from NLs of 59 u (trimethylamine) and 183 u (phosphocholine) were observed.<sup>47,104,113</sup> Although these were the two most abundant product ions of each of the short-chain OxPCs investigated in this work, product ions resulting from the NLs of the *sn*-1 and *sn*-2 fatty acid tails were also observed following CID.

In MS<sup>2</sup>, the *sn*-1 tail was lost as the free acid or as the concurrent loss of the *sn*-1 free fatty acid and trimethylamine. Additionally, various losses of the *sn*-2 tail were observed for each of the OxPCs investigated. For all of the short-chain OxPCs except PGPC, the *sn*-2 tail was preferentially lost as the neutral, sodiated free acid; PGPC fragmentation also yielded a loss of the *sn*-2 tail as the neutral, sodiated free acid, but the *sn*-2 ketene loss (NL of 114 u) was more abundant.

Product ions resulting from the concurrent loss of the *sn*-2 tail and the trimethylamine were also observed at approximately equal or greater relative abundance than that of the product ions resulting from concurrent loss of the *sn*-1 tail and the trimethylamine. This fragmentation pathway has been previously reported for lithium adducts of unmodified PCs.<sup>112</sup> However, the opposite trend was previously observed (i.e., the  $[M+Li-R_1COOH-N(CH_3)_3]^+$  ion was greater in abundance than the  $[M+Li-R_2COOH-N(CH_3)_3]^+$  ion).<sup>112</sup> Therefore, the oxidative modification to the *sn*-2 tail and/or the sodium likely influences this fragmentation pathway.

Figure 2-2 illustrates the MS<sup>2</sup> fragmentation pathways of the PAzPC  $[M+Na]^+$  ion (*m/z* 688). CID of *m/z* 688 resulted in a predominant product ion at *m/z* 629, resulting

from the NL of trimethylamine (NL of 59 u). Loss of the phosphocholine head group (NL of 183 u) was observed at  $m/z$  505. Additionally, NLs of the *sn*-1 free fatty acid (NL of 256 u) and the sodiated *sn*-2 free fatty acid (NL of 210 u) were observed at  $m/z$  432 and 478, respectively. At even lower relative abundances (<0.1%), but still detectable above baseline, product ions corresponding to the loss of the *sn*-2 free acid ( $m/z$  500), *sn*-1 free acid combined with trimethylamine ( $m/z$  373), and *sn*-2 free acid combined with trimethylamine ( $m/z$  441) were observed.

Although MS<sup>2</sup> provides useful structural information, in situ identification of these OxPCs would likely be confounded by isobaric species. Thus, further stages of MS were utilized for enhanced selectivity and increased structural information. For these studies, MS<sup>3</sup> was performed on the product ions resulting from the loss of trimethylamine (NL of 59 u). Table 2-4 summarizes the product ions and relative abundances observed in the MS<sup>3</sup> spectra from the  $[M+Na-N(CH_3)_3]^+$  ions of the short-chain OxPCs. As was shown previously for unmodified PCs,<sup>47</sup> the predominant MS<sup>3</sup> product ion observed resulted from the loss of the remaining portion of the phosphocholine head group (cyclophosphane; NL of 124 u). Although much lower in abundance, MS<sup>3</sup> of these OxPCs yielded product ions corresponding to the NLs of the *sn*-1 and *sn*-2 tails (both as the free acid). In contrast to MS<sup>2</sup> fragmentation, the sodium was not lost with the *sn*-2 tail. Instead, a minor product ion corresponding to the NL of cyclophosphane with sodium (NL of 146 u) was present in the MS<sup>3</sup> spectra from each of the oxidation products studied. Furthermore, an MS<sup>3</sup> product ion at  $m/z$  415, proposed to be the loss of the *sn*-2 tail combined with the loss of acetylene (possibly from the remaining portion of the PC head group), was observed in the MS<sup>3</sup> spectra from each of the short-chain

OxPCs. Lastly, structurally informative product ions, which were only observed for OxPCs containing a terminal carboxylic acid on the *sn*-2 fatty acid tail, resulted from the loss of CO<sub>2</sub> (NL of 44 u). Thus, the NL of CO<sub>2</sub> results in a diagnostic product ion that can be used to differentiate short-chain OxPCs containing a terminal carboxyl group from those containing a terminal aldehyde.

Figure 2-3 illustrates the MS<sup>3</sup> product ion spectrum and fragmentation pathways of the [M+Na-N(CH<sub>3</sub>)<sub>3</sub>]<sup>+</sup> ion (*m/z* 629) of PAzPC. In addition to the product ions observed for all OxPCs investigated, MS<sup>3</sup> product ions of PAzPC resulting from the concurrent loss of the *sn*-1 free acid and cyclophosphane or the sodiated cyclophosphane were observed at *m/z* 249 and 227, respectively. Interestingly, this MS<sup>3</sup> fragmentation pathway was not observed for any of the other short-chain products studied in this work. Furthermore, since PAzPC contains a terminal carboxylic acid group on the *sn*-2 tail, a loss of CO<sub>2</sub> (NL of 44 u) was observed, indicating cleavage of the α-bond relative to the terminal functional group.

MS<sup>4</sup> fragmentation of the [M+Na-HPO<sub>4</sub>(CH<sub>2</sub>)<sub>2</sub>N(CH<sub>3</sub>)<sub>3</sub>]<sup>+</sup> ions varied drastically depending on the *sn*-2 fatty acid length and composition. Despite the variation, the observed product ions yield valuable structural information. Figure 2-4 illustrates the characteristic fragmentation observed in the MS<sup>4</sup> product ion spectrum of *m/z* 688→629→505 corresponding to the [M+Na-HPO<sub>4</sub>(CH<sub>2</sub>)<sub>2</sub>N(CH<sub>3</sub>)<sub>3</sub>]<sup>+</sup> ion of PAzPC. Although recent evidence has suggested that either a 5- or 6-member cyclic structure forms for unmodified PCs prior to MS<sup>4</sup>,<sup>112</sup> at present, the exact structure of this ion is unclear due to the presence of the modified *sn*-2 fatty acid. For simplicity, this ion is displayed without the ring structure. Regardless of the structure, the predominant

product ions at  $m/z$  249 and 227 resulted from the NL of the *sn*-1 fatty acid tail and the *sn*-1 tail with sodium, respectively. These product ions, in addition to the product ions at  $m/z$  279, 211, 193, 171, and 153, which were attributed to  $[R_1\text{COOH}+\text{Na}]^+$ ,  $[R_2'\text{COOH}+\text{Na}]^+$ ,  $[R_2'\text{COOH}+\text{Na}-\text{H}_2\text{O}]^+$ ,  $[R_2'\text{COOH}+\text{H}-\text{H}_2\text{O}]^+$ , and  $[R_2'\text{COOH}+\text{H}-2\text{H}_2\text{O}]^+$ , respectively, confirmed the identification of both fatty acid substituents of PAzPC. Furthermore, the NL of 56 u ( $m/z$  449) was observed in the MS<sup>4</sup> product ion spectrum of PAzPC and likely corresponds to the loss of C<sub>3</sub>H<sub>4</sub>O as previously reported for MS<sup>n</sup> on the  $[M+\text{Na}]^+$  ions of triacylglycerols.<sup>114</sup> However, this loss of 56 was observed in the MS<sup>4</sup> product ion spectrum from each of the OxPCs investigated in this work and is therefore less structurally informative than the product ions related to the fatty acid tails.

The MS<sup>4</sup> product ion spectra from CID of the  $[M+\text{Na}-\text{HPO}_4(\text{CH}_2)_2\text{N}(\text{CH}_3)_3]^+$  ion of PONPC, PGPG, POVPC and KOdiAPC are depicted in Figures 2-5, 2-6, 2-7, and 2-8 respectively. Many product ions analogous to those described above for PAzPC were also observed in the MS<sup>4</sup> spectra of the other OxPCs; however, MS<sup>4</sup> product ions specific to the type of oxidative modification were also detected. One diagnostic fragmentation pathway was the loss of the *sn*-1 fatty acid tail; in contrast to the carboxylic acid derivatives, the OxPCs containing a terminal aldehyde lost the *sn*-1 tail (palmitic acid; 256 u) as the NL of 254 u rather than 256 u. Based on previously reported MS<sup>2</sup> fragmentation of  $[M+\text{Li}]^+$  ions of unmodified PCs<sup>115</sup> and triacylglycerols,<sup>114</sup> the NL of 254 u likely results from the elimination of  $\alpha,\beta$ -unsaturated fatty acid from the *sn*-1 substituent. Interestingly, unmodified PCs only lost the  $\alpha,\beta$ -unsaturated fatty acid from the *sn*-2 substituent, not from the *sn*-1 substituent;<sup>115</sup> thus the terminal aldehyde

on the *sn*-2 substituent of the OxPCs is likely playing some role in the formation of this product ion.

Furthermore, MS<sup>4</sup> of the keto-containing OxPC, KOdiAPC, yielded multiple fragmentation pathways not observed for other short-chain OxPCs; specifically, cleavages between C<sub>2</sub>–C<sub>3</sub> (*m/z* 377) and C<sub>3</sub>–C<sub>4</sub> (*m/z* 367) of the *sn*-2 fatty acid tail were observed (Figure 2-8). To confirm these fragmentation pathways, accurate mass measurements were performed on the hybrid LTQ FT mass spectrometer. The FTICR mass spectra obtained from MS<sup>4</sup> on the [M+Na–HPO<sub>4</sub>(CH<sub>2</sub>)<sub>2</sub>N(CH<sub>3</sub>)<sub>3</sub>]<sup>+</sup> ion from KOdiAPC exhibited product ions at *m/z* 377.2676 (error of 2.18 ppm) and *m/z* 367.2856 (error of 2.10 ppm), thereby confirming the proposed molecular formulae. Although the mechanism was not confirmed, one possible rationale for the C<sub>2</sub>–C<sub>3</sub> cleavage is an intramolecular retro-ene reaction involving the C<sub>5</sub> carbonyl group (Figure 2-9 Scheme 1). This mechanism is similar to that proposed by Cheng and Gross for β-cleavage of oxofatty acids.<sup>116</sup> Although γ-cleavage was observed relative to the C<sub>5</sub> carbonyl group, the C<sub>3</sub>–C<sub>4</sub> cleavage is thought to result from an intramolecular retro-ene reaction involving the C<sub>1</sub> carbonyl group (Figure 2-9 Scheme 2), rather than 1,4-hydrogen elimination as previously reported.<sup>116</sup> 1,4-hydrogen elimination was considered; however, the six-membered cyclic intermediate required for 1,4-hydrogen elimination is not favorable, as the *sn*-2 tail does not contain four consecutive carbons with accessible hydrogens.

### Identifying and Imaging OxPCs in Spinal Cord Tissue

Following MS<sup>n</sup> characterization of OxPC standards, [M+Na]<sup>+</sup> ions of potential OxPCs were targeted for in situ identification and MS<sup>n</sup> imaging. Figure 2-10 illustrates the identification and localization of two isobaric OxPCs in spinal cord tissue. The

MALDI MS spectrum obtained by averaging the mass spectra across the entire tissue section (approximately 700 scans) depicts the complex mixture of biomolecules obtained from tissue. One potential PC oxidation product, PC(18:0/9:0 COOH), was targeted for MS<sup>n</sup> analysis. Upon CID of the expected [M+Na]<sup>+</sup> ion (*m/z* 716), MS<sup>n</sup> product ions (indicated with purple diamonds) were analogous to those predicted based on the fragmentation pathways outlined in Tables 2-2, 2-3, and 2-4. Thus, product ions observed in the MS<sup>2</sup>, MS<sup>3</sup>, and MS<sup>4</sup> spectra allowed for in situ identification of PC(18:0/9:0 COOH). However, additional MS<sup>2</sup>, MS<sup>3</sup>, and MS<sup>4</sup> product ions (indicated with orange stars) indicated the presence of an isobaric ion at *m/z* 716. Based on these product ions, another OxPC was identified at *m/z* 716, [PC(16:0/11:0 COOH)+Na]<sup>+</sup>.

After collecting the MS<sup>n</sup> spectra, extracted ion images were generated to determine the localization of the OxPCs at *m/z* 716 in tissue. The MS image of [PC(16:0/16:0)+Na]<sup>+</sup> at *m/z* 756 (normalized to the TIC) is provided to distinguish the gray matter (outlined in red) from the white matter of the spinal cord; this same outline is superimposed atop the other images, demonstrating the localization of these OxPCs in the gray matter. The MS<sup>n</sup> spectra and images depicted in Figure 2-10 illustrate the enhanced selectivity afforded by the LIT, allowing for identification and localization of OxPCs in situ.

## Conclusions

This study has established that MALDI MS<sup>n</sup> is a powerful technique for characterizing various short-chain oxidation products of phosphatidylcholines. Based on the characteristic MALDI MS<sup>n</sup> fragmentation of the [M+H]<sup>+</sup> and [M+Na]<sup>+</sup> ions of various short-chain OxPCs, valuable structural information is obtained. In MS<sup>2</sup>, CID of the [M+H]<sup>+</sup> and [M+Na]<sup>+</sup> ions of PAzPC, PONPC, PGPC, POVPC, and KOdiAPC led to

various product ions, which were analogous to those previously reported for unmodified PCs. For additional structural information, the ion corresponding to the NL of 59 u from the  $[M+Na]^+$  was fragmented in  $MS^3$  and yielded multiple product ions, one of which (the NL of  $CO_2$ ) was diagnostic of a terminal carboxyl group on the *sn*-2 tail. Furthermore,  $MS^4$  of the  $[M+Na]^+$  resulted in drastically different fragmentation depending on the *sn*-2 fatty acid length and type of functional group(s) added. An  $MS^4$  fragmentation pathway characteristic of OxPCs containing a terminal aldehyde rather than a carboxylic acid was the NL of 254 u, thought to correspond to the elimination of the  $\alpha,\beta$ -unsaturated *sn*-1 fatty acid substituent (16:1). Additionally, the presence of the keto group in KOdiAPC led to mid-chain cleavages of the *sn*-2 fatty acid moiety.

This work also illustrates the feasibility of this MALDI  $MS^n$  methodology for the analysis and identification of individual PC oxidation products in complex mixtures including intact biological tissues. The diagnostic ions detailed in this study were utilized for targeted MALDI  $MS^n$  imaging studies to determine the distribution of OxPCs in tissue sections. Through the development of selective methods for identifying these OxPCs and determining their in situ localization, a greater understanding of the biological and physiopathological activities of these phospholipid oxidation products may be achieved.

Table 2-1. Nomenclature of the OxPC standards analyzed.<sup>a</sup>

Chemical Name [shorthand]	R <sub>1</sub>	R <sub>2</sub> '	Monoisotopic Mass
1-palmitoyl-2-(5-oxo-valeroyl)- <i>sn</i> -glycero-3-phosphocholine [POVPC]	16:0	5:0 (CHO)	593.37
1-palmitoyl-2-glutaryl- <i>sn</i> -glycero-3-phosphocholine [PGPC]	16:0	5:0 (COOH)	609.36
1-palmitoyl-2-(9-oxo-nonanoyl)- <i>sn</i> -glycero-3-phosphocholine [PONPC]	16:0	9:0 (CHO)	649.43
1-palmitoyl-2-azelaoyl- <i>sn</i> -glycero-3-phosphocholine [PAzPC]	16:0	9:0 (COOH)	665.43
1-palmitoyl-2-(5-keto-6-octene-dioyl)- <i>sn</i> -glycero-3-phosphocholine [KODiAPC]	16:0	8:1 (COOH) <sup>b</sup>	663.37

<sup>a</sup> Nomenclature according to the LIPID MAPS systematic naming is used ([www.lipidmaps.org](http://www.lipidmaps.org)). R<sub>1</sub> represents the number of carbons and double bonds (#C:#DB) in the fatty acid substituents esterified to the *sn*-1 position of the glycerol backbone. R<sub>2</sub>' represents the number of carbons and double bonds in the oxidatively truncated fatty acid substituent. These *sn*-2 acyl groups contain 5–9 carbon atoms and a terminal aldehyde (CHO) or carboxyl group (COOH).

<sup>b</sup> In addition to the terminal  $\alpha,\beta$ -unsaturated carboxyl group, the *sn*-2 tail of KODiAPC also contains a ketone at C<sub>5</sub>.

Table 2-2. Product ions observed in the MS<sup>2</sup> spectra of [M+H]<sup>+</sup> ions of PAzPC, PONPC, PGPC, POVPC, and KOdiAPC.<sup>a</sup>

	PAzPC <i>m/z</i> 666	PONPC <i>m/z</i> 650	PGPC <i>m/z</i> 610	POVPC <i>m/z</i> 594	KOdiAPC <i>m/z</i> 664
[H <sub>2</sub> PO <sub>4</sub> (CH <sub>2</sub> ) <sub>2</sub> N(CH <sub>3</sub> ) <sub>3</sub> ] <sup>+b</sup>	184 (100)	184 (100)	184 (100)	184 (100)	184 (100)
-R <sub>1</sub> =C=O	428 (0.4)	412(1.6)	372(0.6)	356 (0.5)	426 (1.0)
-R <sub>2</sub> '=C=O	496 (1.1)	496 (3.4)	496 (1.1)	496 (0.7)	496 (2.5)
-R <sub>1</sub> COOH	410 (1.2)	394 (3.5)	354 (1.2)	338 (0.8)	408 (1.4)
-R <sub>2</sub> 'COOH	478 (0.5)	478 (2.1)	478(0.7)	478 (0.7)	478 (1.1)
-HPO <sub>4</sub> (CH <sub>2</sub> ) <sub>2</sub> N(CH <sub>3</sub> ) <sub>3</sub>	483 (0.3)	467 (1.2)	427 (0.3)	411 (0.5)	481 (1.2)
-H <sub>2</sub> O	648 (1.5)	NA	592 (1.1)	NA	646 (9.6)
-N(CH <sub>3</sub> ) <sub>3</sub>	NA	591 (0.4)	NA	NA	605 (8.9)
-CO <sub>2</sub>	NA	NA	566 (0.1)	NA	620 (1.9)

<sup>a</sup> Relative abundances (%) for each product ion are given in parentheses. The abundance was rounded to the nearest tenth of a percent. NA=relative abundances ≤0.1%.

<sup>b</sup> Indicates a product ion rather than a NL.

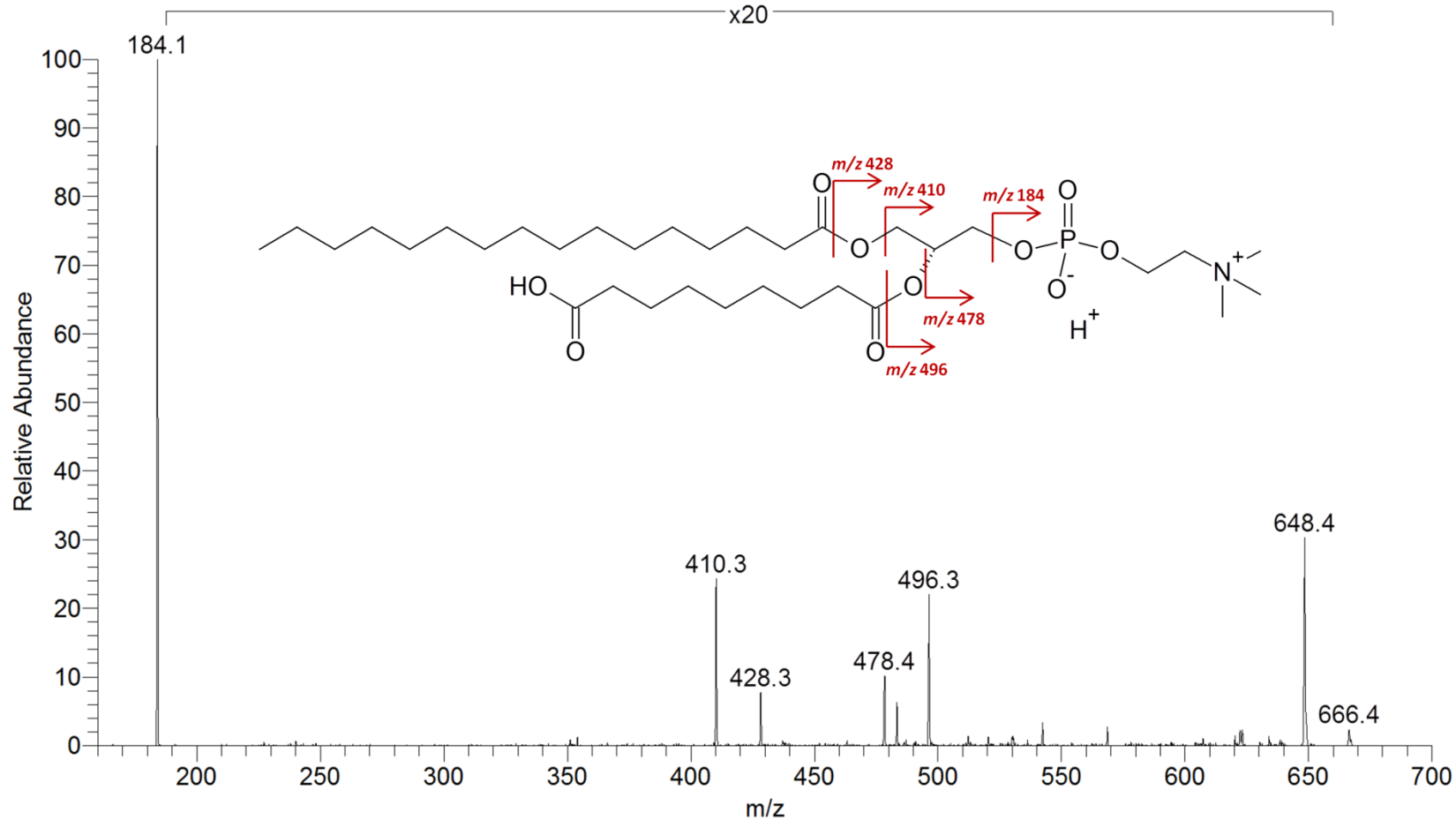


Figure 2-1. MS<sup>2</sup> product ion spectrum of  $m/z$  666, the  $[M+H]^+$  ion of PAzPC. The structure and proposed fragmentation of the ion at  $m/z$  666 are also shown.

Table 2-3. Product ions observed in MS<sup>2</sup> spectra of [M+Na]<sup>+</sup> ions of PAzPC, PONPC, PGPC, POVPC, and KOdiAPC.<sup>a</sup>

	PAzPC <i>m/z</i> 688	PONPC <i>m/z</i> 672	PGPC <i>m/z</i> 632	POVPC <i>m/z</i> 616	KOdiAPC <i>m/z</i> 686
-N(CH <sub>3</sub> ) <sub>3</sub>	629 (100)	613 (100)	573 (100)	557 (100)	627 (100)
-HPO <sub>4</sub> (CH <sub>2</sub> ) <sub>2</sub> N(CH <sub>3</sub> ) <sub>3</sub>	505 (12.2)	489 (7.5)	449 (15.1)	433 (10.5)	503 (7.2)
-R <sub>2</sub> 'COONa	478 (0.3)	478 (0.1)	478 (0.2)	478 (0.3)	478 (0.2)
-R <sub>1</sub> COOH	432 (0.2)	416 (0.1)	376 (0.1)	360 (0.1)	430 (0.1)
-R <sub>2</sub> 'COOH	500 (0.1)	500 (0.1)	500 (0.3)	500 (0.2)	500 (0.2)
-R <sub>1</sub> COOH & N(CH <sub>3</sub> ) <sub>3</sub>	373 (0.1)	357 (0.1)	317 (0.1)	301 (0.1)	371 (0.1)
-R <sub>2</sub> 'COOH & N(CH <sub>3</sub> ) <sub>3</sub>	441 (0.1)	NA	441 (0.4)	441 (0.3)	441 (0.2)
-R <sub>2</sub> '=C=O	NA	NA	518 (0.6)	NA	518 (0.1)

<sup>a</sup> Relative abundances (%) for each product ion are given in parentheses. The abundance was rounded to the nearest tenth of a percent. NA=relative abundances ≤0.05%.

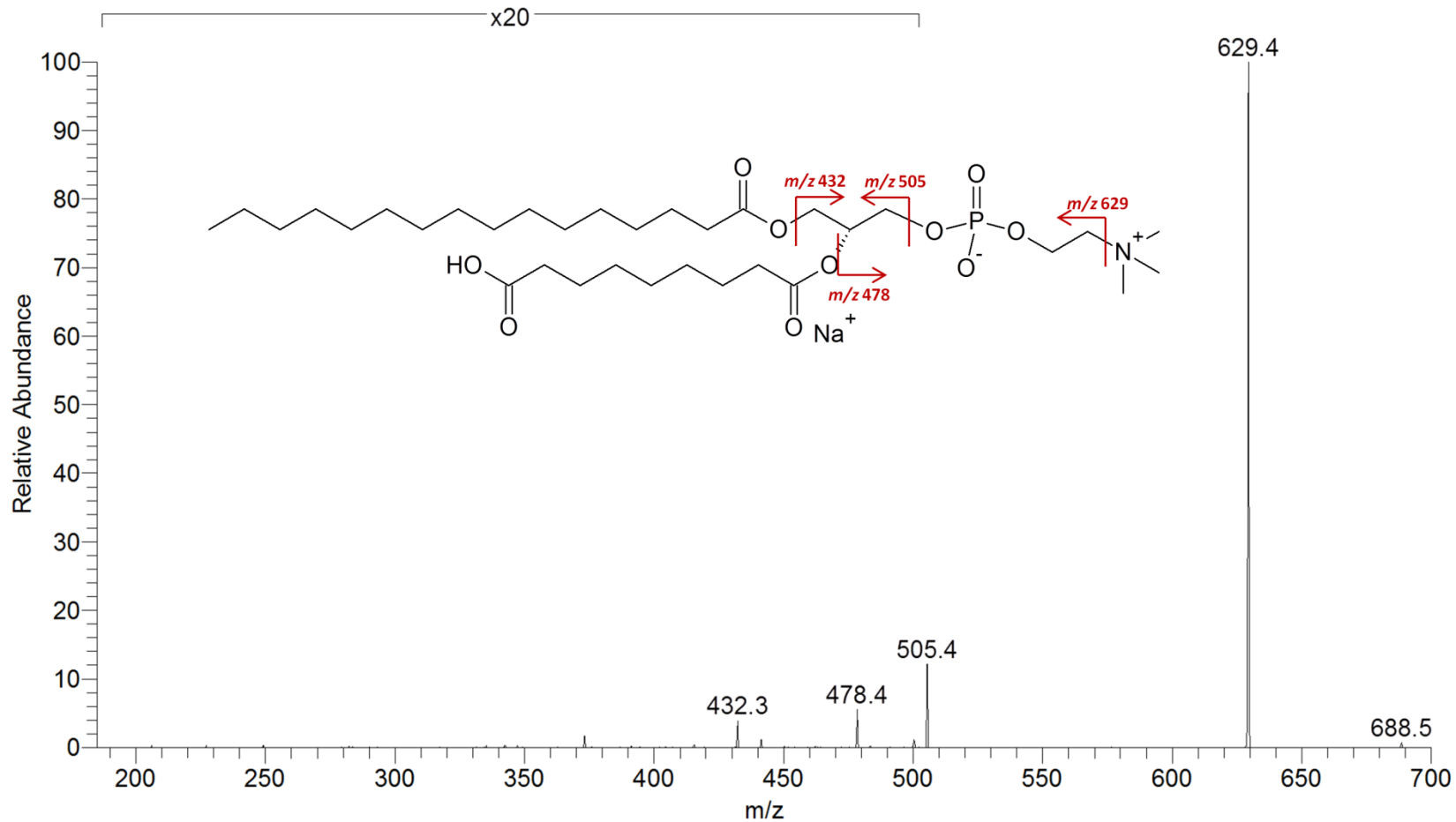


Figure 2-2. MS<sup>2</sup> product ion spectrum of  $m/z$  688, the  $[M+Na]^+$  ion of PAzPC. The structure and proposed fragmentation of the ion at  $m/z$  688 are also shown.

Table 2-4. Product ions observed in MS<sup>3</sup> spectra of [M+Na-N(CH<sub>3</sub>)<sub>3</sub>]<sup>+</sup> ions of PAzPC, PONPC, PGPC, POVPC, and KOdiAPC.<sup>a</sup>

	PAzPC <i>m/z</i> 629	PONPC <i>m/z</i> 613	PGPC <i>m/z</i> 573	POVPC <i>m/z</i> 557	KOdiAPC <i>m/z</i> 627
-HPO <sub>4</sub> (CH <sub>2</sub> ) <sub>2</sub>	505 (100)	489 (100)	449 (100)	433 (100)	503 (100)
-HPO <sub>4</sub> (CH <sub>2</sub> ) <sub>2</sub> & Na	483 (0.3)	467 (0.4)	427 (0.4)	411 (1)	481 (0.5)
-R <sub>2</sub> 'COOH	441 (0.5)	441 (0.7)	441 (2.5)	441 (2.5)	441 (2.6)
-R <sub>2</sub> 'COOH & C≡C	415 (0.1)	415 (0.1)	415 (0.1)	415 (0.2)	415 (0.2)
-R <sub>1</sub> COOH	373 (0.4)	357 (0.5)	317 (0.5)	301 (0.5)	371 (0.4)
-R <sub>1</sub> COOH & HPO <sub>4</sub> (CH <sub>2</sub> ) <sub>2</sub>	249 (0.8)	NA	NA	NA	NA
-R <sub>1</sub> COOH & HPO <sub>4</sub> (CH <sub>2</sub> ) <sub>2</sub> & Na	227 (0.3)	NA	NA	NA	NA
-CO <sub>2</sub>	585 (0.1)	NA	529 (0.1)	NA	583 (0.1)
- C <sub>6</sub> H <sub>6</sub> O <sub>3</sub> & HPO <sub>4</sub> (CH <sub>2</sub> ) <sub>2</sub> <sup>b</sup>	NA	NA	NA	NA	377 (1.1)

<sup>a</sup> Relative abundances (%) for each product ion are given in parentheses. The abundance was rounded to the nearest tenth of a percent. NA=relative abundances ≤0.05%.

<sup>b</sup> Fragmentation resulting from proposed intramolecular retro-ene reaction discussed later in the text.

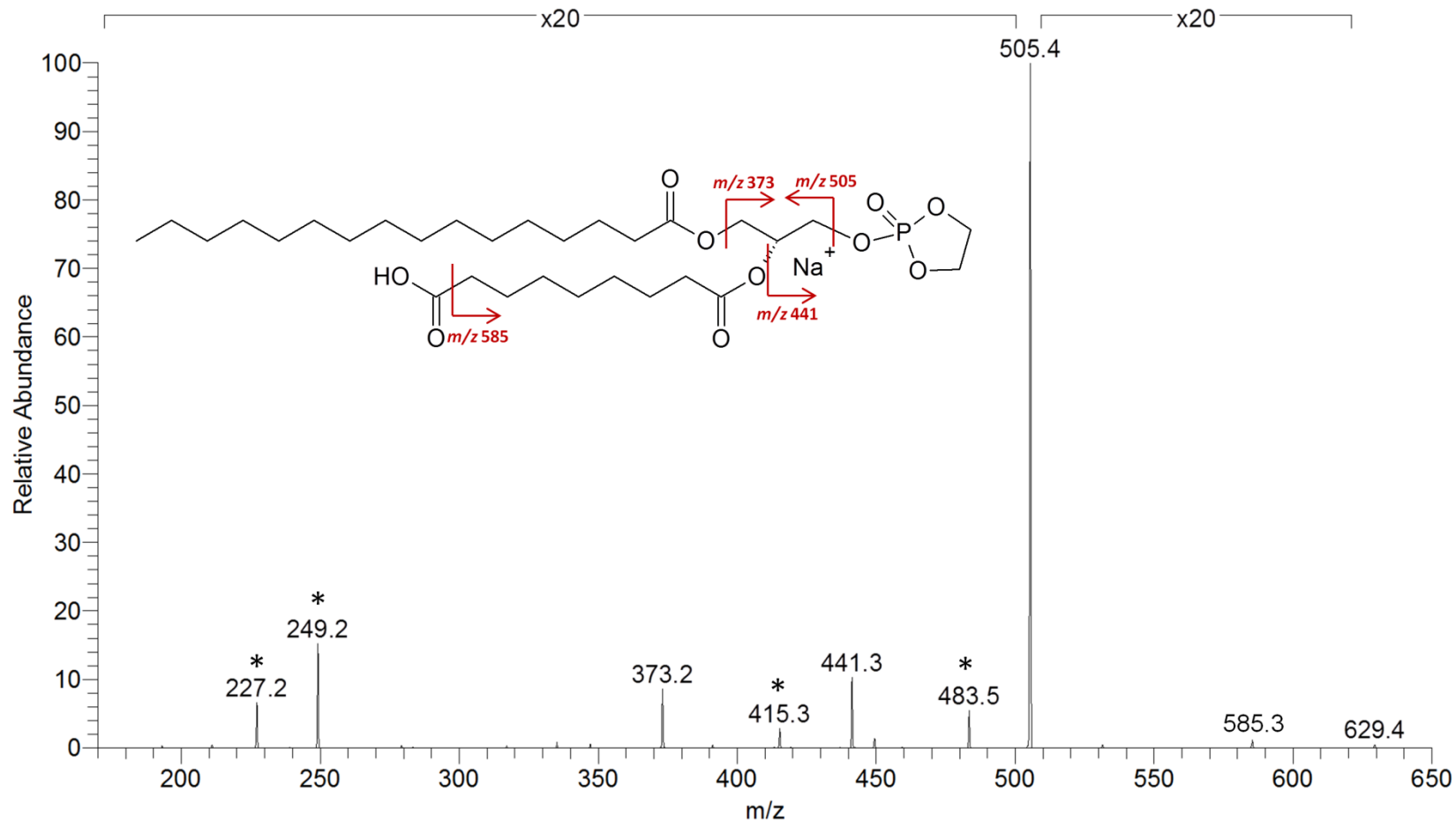


Figure 2-3. MS<sup>3</sup> product ion spectrum of  $m/z$  688→629, the  $[M+Na-N(CH_3)_3]^+$  ion of PAzPC. The structure and proposed fragmentation of the ion at  $m/z$  629 are also shown. Fragmentation pathways leading to the product ions marked with an asterisk are discussed in the text.

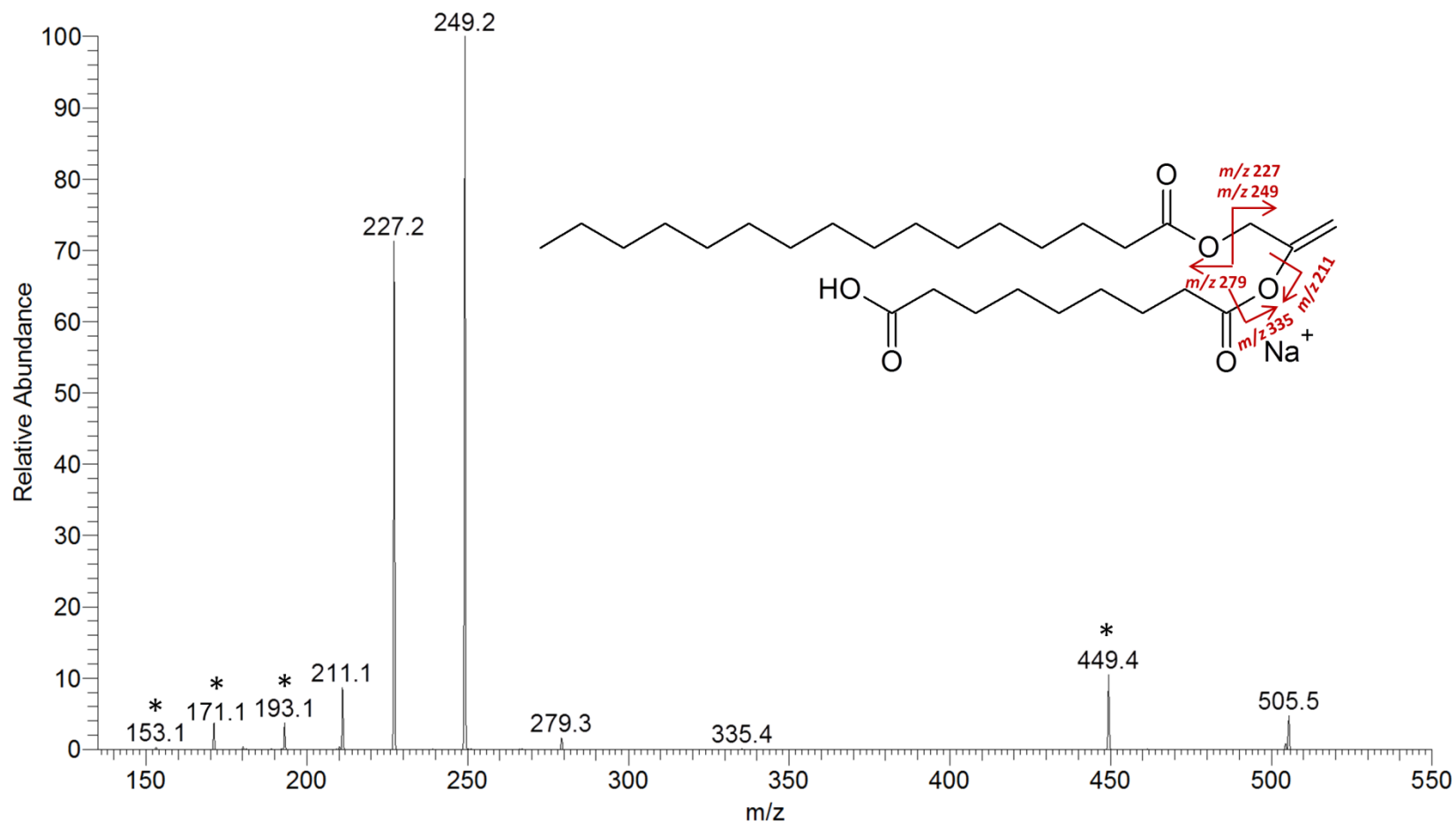


Figure 2-4. MS<sup>4</sup> product ion spectrum of  $m/z$  688→629→505, the  $[M+Na-HPO_4(CH_2)_2N(CH_3)_3]^+$  ion of PAzPC. The proposed structure and fragmentation of the ion at  $m/z$  505 are also shown. Product ions marked with an asterisk are discussed in the text.

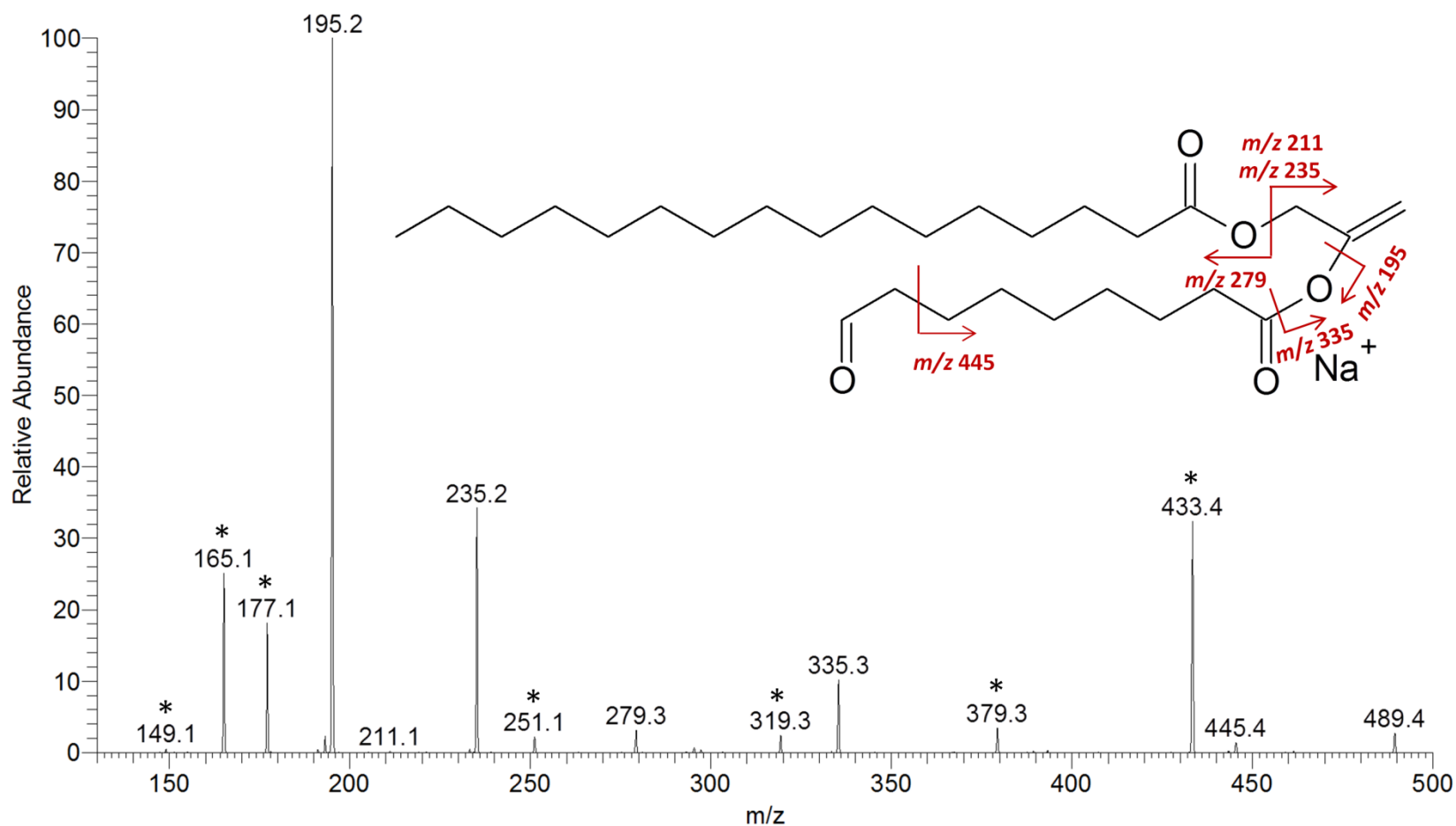


Figure 2-5. MS<sup>4</sup> product ion spectrum of  $m/z$  672→613→489, the  $[M+Na-HPO_4(CH_2)_2N(CH_3)_3]^+$  ion of PONPC. The proposed structure and fragmentation of the ion at  $m/z$  489 are also shown. Product ions marked with an asterisk were identified as follows. The ion at  $m/z$  433 results from the loss of  $C_3H_4O$  from either the terminal portion of the *sn*-2 tail or from the glycerol backbone as previously reported.<sup>13</sup> The ion at  $m/z$  379 likely results from the loss of  $C_7H_{16}$ , potentially from the *sn*-1 fatty acid tail. The product ions resulting from the NL of  $R_2'COOH$  and  $R_1=C=O$  were also observed at  $m/z$  319 and  $m/z$  251, respectively. Furthermore, the product ions at  $m/z$  177, 165, and 149 are believed to correspond to  $[R_2'COOH+Na-H_2O]^+$ ,  $[R_2'COOH+Na-CH_2O]^+$ , and  $[R_2'COOH+Na-HCOOH]^+$ , respectively.

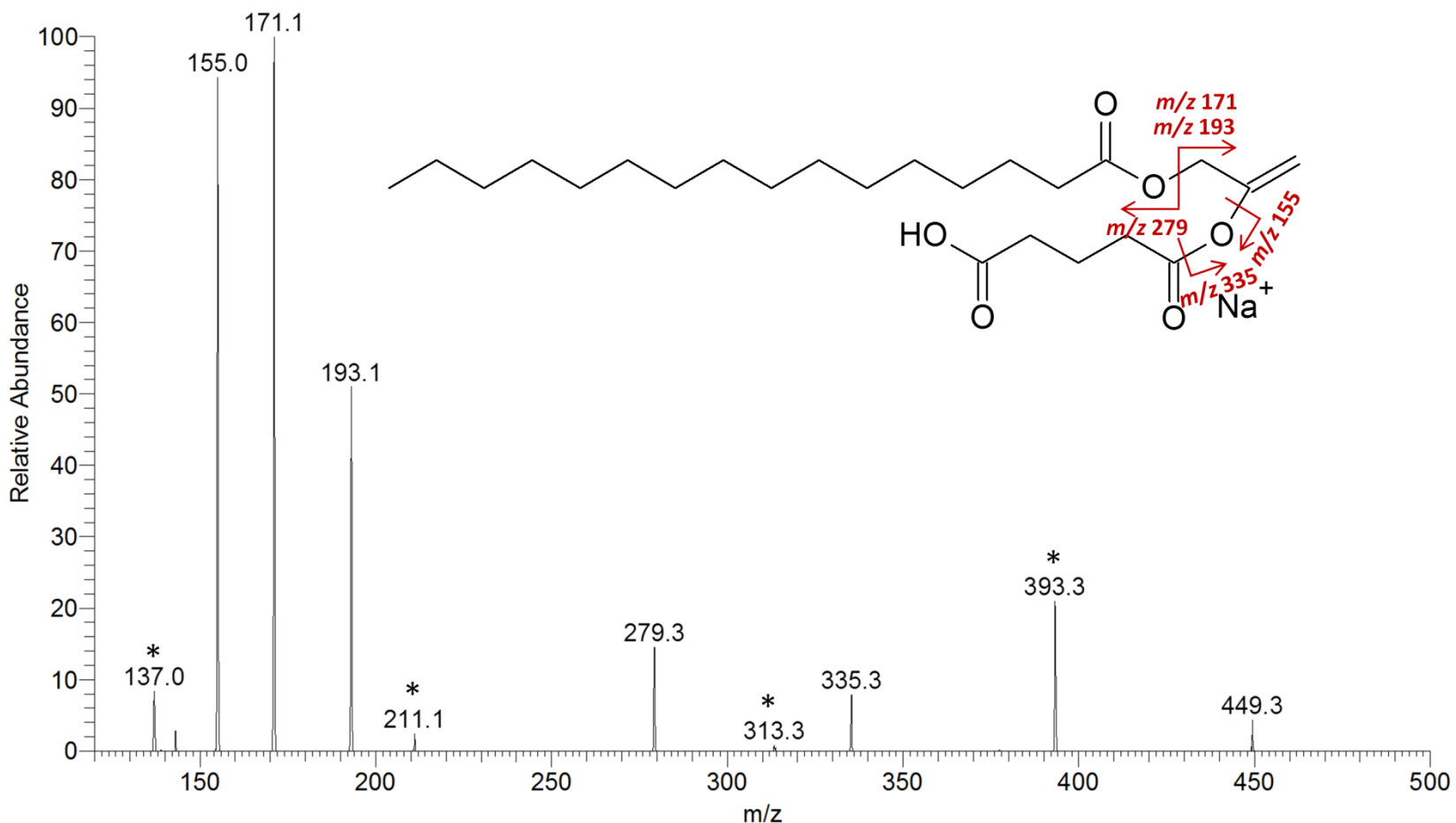


Figure 2-6. MS<sup>4</sup> product ion spectrum of  $m/z$  632→573→449, the  $[M+Na-HPO_4(CH_2)_2N(CH_3)_3]^+$  ion of PGPC. The proposed structure and fragmentation of the ion at  $m/z$  449 is also shown. Product ions marked with an asterisk were identified as follows. The ion at  $m/z$  393 results from the loss of  $C_3H_4O$  most likely from the glycerol backbone as previously reported.<sup>13</sup> The ion at  $m/z$  313 likely results from the combined NL of  $R_2'=C=O$  and Na and the ion at  $m/z$  211 results from the NL of  $R_1=C=O$ . Lastly,  $m/z$  137 corresponds to  $[R_2'COOH+Na-H_2O]^+$ .

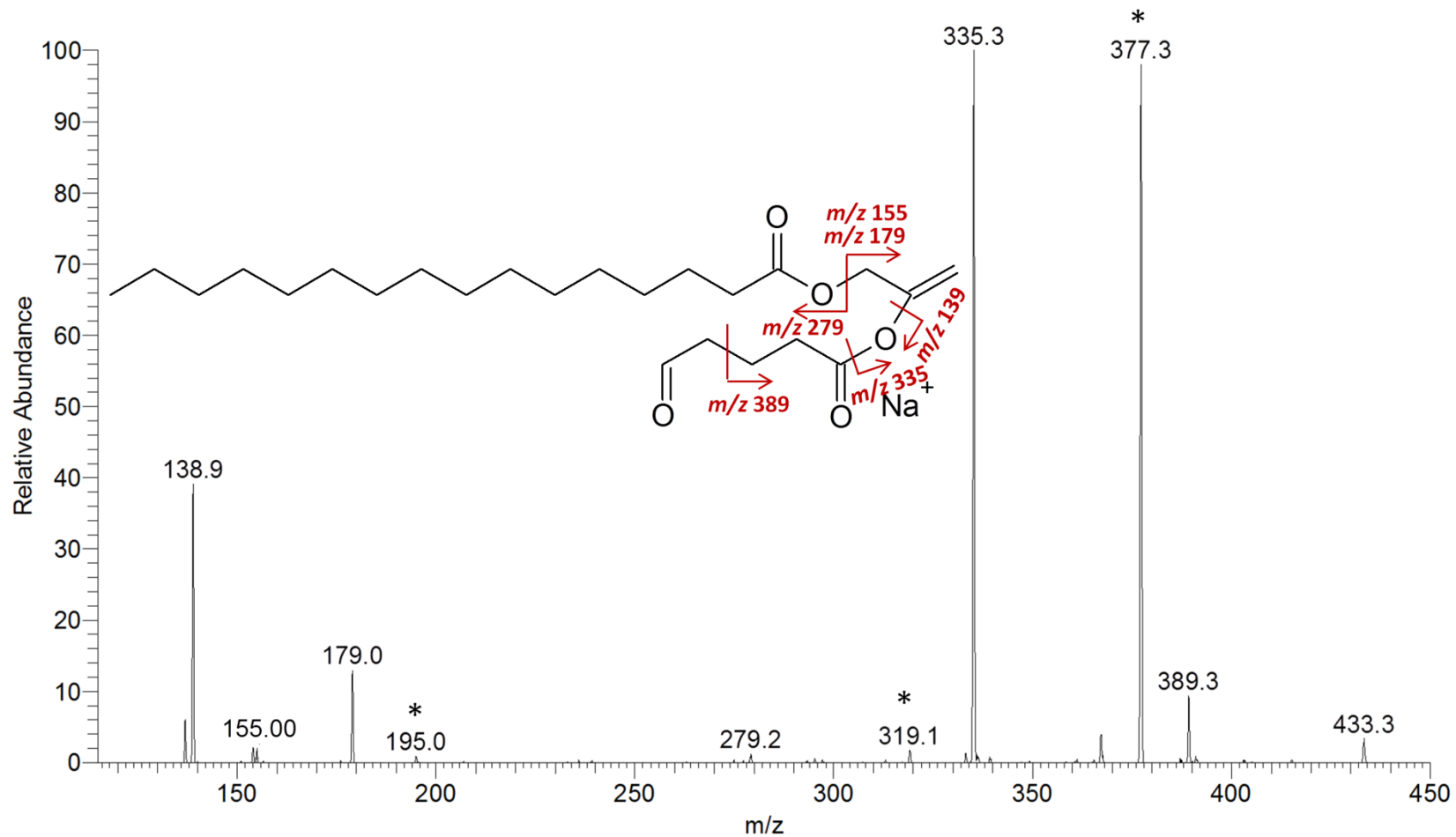


Figure 2-7. MS<sup>4</sup> product ion spectrum of  $m/z$  616→557→433, the  $[M+Na-HPO_4(CH_2)_2N(CH_3)_3]^+$  ion of POVPC. The proposed structure and fragmentation of the ion at  $m/z$  433 is also shown. Product ions marked with an asterisk were identified as follows. The ion at  $m/z$  377 results from the loss of  $C_3H_4O$  from either the terminal portion of the *sn*-2 tail or from the glycerol backbone as previously reported.<sup>13</sup> The product ions at  $m/z$  319 and 195 result from the NL of  $R_2'COOH$  and the NL of  $R_1=C=O$ , respectively.

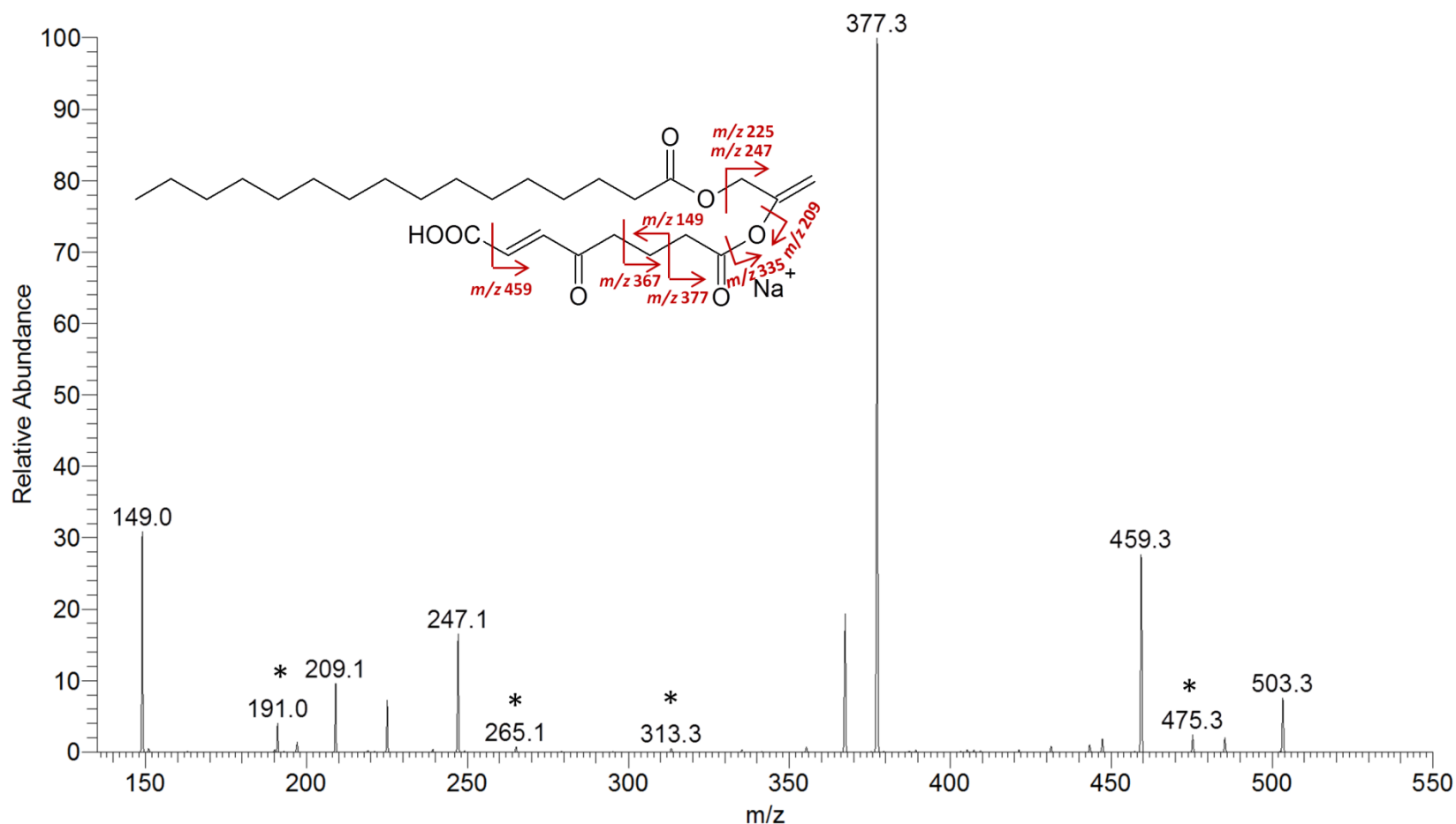
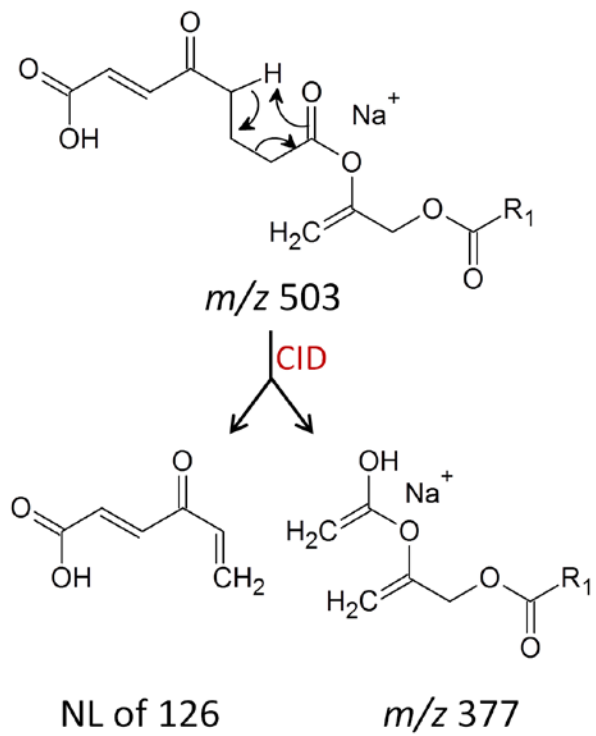


Figure 2-8. MS<sup>4</sup> product ion spectrum of  $m/z$  686→627→503, the  $[M+Na-HPO_4(CH_2)_2N(CH_3)_3]^+$  ion of KOdiAPC. The proposed structure and fragmentation of the ion at  $m/z$  503 are also shown. Product ions marked with an asterisk were identified as follows. The NL of 28 u ( $m/z$  475) likely results from the NL of  $C_2H_4$ ; however, the exact site of fragmentation is unknown. Although low in abundance,  $m/z$  447 is observed and is likely produced by the NL of  $C_3H_4O$  from the glycerol backbone as previously reported.<sup>13</sup> The ion at  $m/z$  313 is proposed to result from the combined NL of  $R_2'=C=O$  and Na and the ion at  $m/z$  265 from the NL of  $R_1=C=O$ . Lastly,  $m/z$  191 corresponds to  $[R_2'COOH+Na-H_2O]^+$ .

**Scheme 1.**



**Scheme 2.**

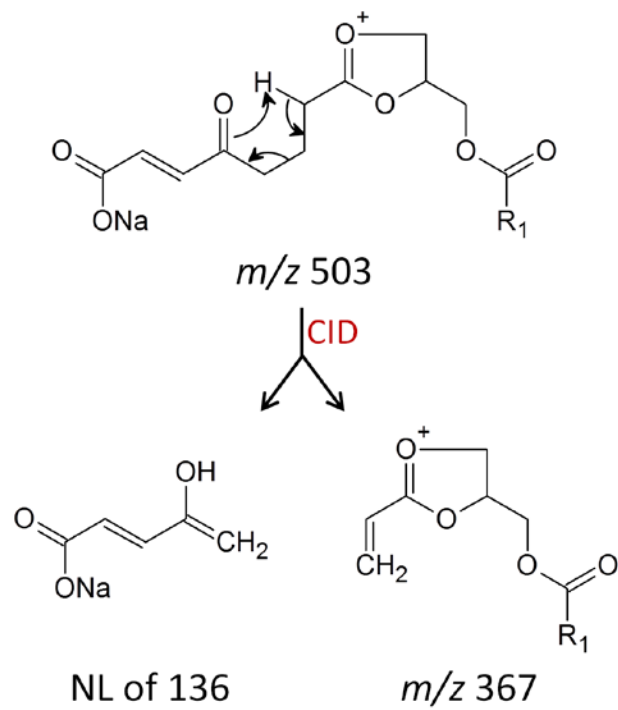


Figure 2-9. Schemes for the proposed intramolecular retro-ene mechanism.

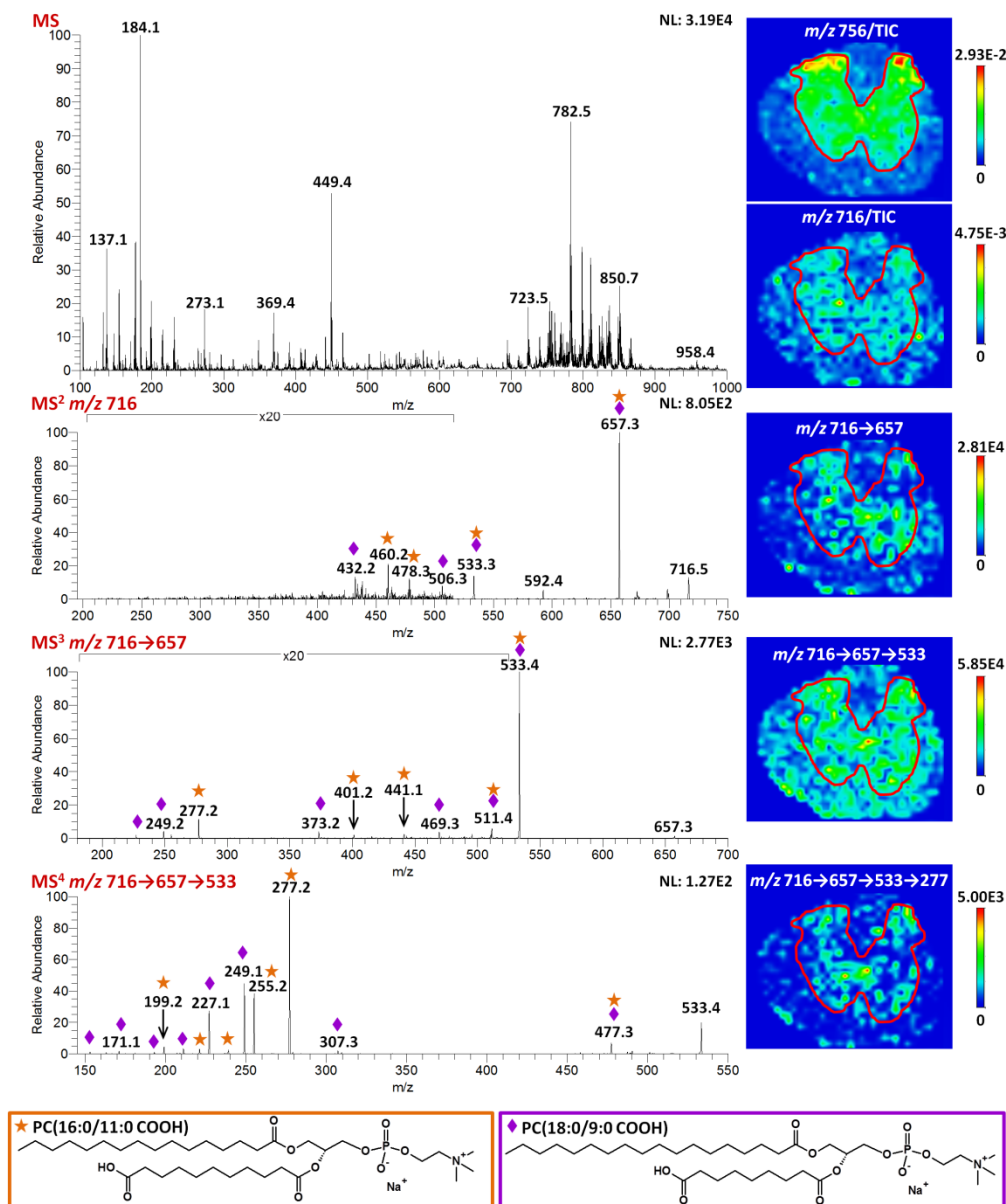


Figure 2-10. Identification and imaging of two proposed OxPCs at  $m/z$  716. The MS spectrum illustrates the complex mixture of biomolecules observed in tissue. MS<sup>2</sup>, MS<sup>3</sup>, and MS<sup>4</sup> spectra and images demonstrate the feasibility of identifying and localizing OxPCs in biological tissues using the MALDI MS<sup>n</sup> methods developed in this work. Based on the product ions observed, two isobaric OxPCs were identified, PC(16:0/11:0 COOH) and PC(18:0/9:0 COOH). The proposed structures are displayed in the orange and purple boxes and the product ions specific to each of these OxPCs are indicated by orange stars and purple diamonds for PC(16:0/11:0 COOH) and PC(18:0/9:0 COOH), respectively. Furthermore, upon comparison of the MS<sup>n</sup> images of  $m/z$  716 ([PC(16:0/11:0 COOH)+Na]<sup>+</sup> and [PC(18:0/9:0 COOH)+Na]<sup>+</sup>) to the MS image of  $m/z$  756 ([PC(16:0/16:0)+Na]<sup>+</sup>, a PL known to localize in the gray matter of rat spinal cord), the ions related to the OxPCs appear mostly in the gray matter (outlined in red).

## CHAPTER 3 MALDI MS<sup>n</sup> CHARACTERIZATION OF PHOSPHATIDYLETHANOLAMINE OXIDATION PRODUCTS

### **Introduction**

Under oxidative conditions, unsaturated phospholipids undergo structural modifications that result in alterations to the fluidity, permeability, and integrity of cellular membranes.<sup>14</sup> In addition to phosphatidylcholines (PCs), phosphatidylethanolamines (PEs) are a major class of phospholipids found within the bilayer of cellular membranes.<sup>109</sup> PEs are extremely abundant in the retina, where photoreceptor cell membranes are expected to be highly susceptible to oxidative damage as these membranes contain the most unsaturated fatty acids found in vertebrate tissues; greater than 50% of the total retinal fatty acids are unsaturated.<sup>35</sup> Furthermore, photoreceptor membrane disks are also regularly exposed to light and oxygen making them prone to photogenerated free radical-induced oxidative modification.<sup>35</sup>

Although the high susceptibility of retinal tissue to oxidative damage has led to the implication of phospholipid oxidation in diseases such as age-related macular degeneration (AMD),<sup>5,35,117</sup> there is only limited information regarding the lipid composition of normal and diseased retinal tissue.<sup>118</sup> However, one specific PE oxidation product, 4-hydroxy-7-oxohept-5-enoic acid phosphatidylethanolamine (HOHA-PE), is thought to play a central role in promoting the most devastating form of AMD, choroidal neovascularization (CNV) which causes irreversible loss of vision in elderly humans.<sup>35</sup> Therefore, there is growing interest in investigating PE oxidation products (OxPEs) and developing methods to identify these products in biological tissues such as the retina.

Recently, there have been several published studies reporting the direct analysis of OxPEs by MS using soft-ionization techniques, such as ESI and MALDI.<sup>14,15</sup> In 1998, Khaselev and Murphy reported the use of ESI MS<sup>2</sup> for the investigation of plasmenyl OxPEs resulting from in vitro oxidation of a bovine brain PE mixture.<sup>119</sup> Gugiu et al. also used ESI MS and MS<sup>2</sup> in combination with RP-HPLC to investigate short-chain OxPEs produced by in vitro oxidation of unsaturated PEs and to identify these OxPEs in retinal extracts.<sup>35</sup> Another recent study used ESI MS in combination with thin-layer chromatography (TLC) to monitor autoxidation of various PLs including 1-palmitoyl-2-arachidonoyl-*sn*-glycero-3-phosphoethanolamine (PAPE) prior to investigating lipopolysaccharide inhibition by these OxPLs.<sup>120</sup> Furthermore, oxidative modifications to one specific unsaturated PE, 1-palmitoyl-2-linoleoyl-*sn*-glycero-3-phosphoethanolamine (PLPE), were studied by RP-HPLC ESI MS<sup>2</sup>.<sup>103</sup>

Although most studies have employed ESI MS as the method of choice for analysis of OxPLs, Stübiger et al. published in 2010 the first study investigating sample preparation techniques for MALDI MS analysis of OxPCs, OxPEs, and OxPSs.<sup>45</sup> Additionally, TLC-MALDI MS methods for monitoring oxidation products of PCs and PEs have also been recently reported.<sup>108</sup> To build upon these works, this study investigates the MALDI MS<sup>n</sup> (where n = 2, 3, and 4) fragmentation of several short-chain OxPEs. Four different unsaturated PE standards were exposed to 48 h of autoxidation in ambient air and light. The observed oxidation products were then identified by MALDI MS<sup>n</sup> utilizing a linear ion trap (LIT) mass analyzer. Up to four stages of mass analysis (MS<sup>4</sup>) were used to fully characterize these OxPEs. This work illustrates the feasibility of MS<sup>n</sup> experiments for obtaining valuable structural information on OxPEs.

## Experimental Section

### Chemicals

Fisher Scientific (Fair Lawn, NJ) was the supplier of chloroform ( $\text{CHCl}_3$ ), methanol (MeOH), and sodium acetate trihydrate (NaOAc). All lipid standards, which are summarized in Table 3-1, were purchased in  $\text{CHCl}_3$  (10 mg/mL) from Avanti Polar Lipids (Alabaster, AL). These standards were further diluted in  $\text{CHCl}_3$  to a final concentration of 100 ppm. MALDI matrix, 2,5-dihydroxybenzoic acid (DHB), was purchased from Acros Organics (Geel, Belgium). A matrix solution of 40 mg/mL was prepared in a solvent system of 50:50  $\text{CHCl}_3$ :MeOH with a final concentration of 10 mM NaOAc.

### Oxidation Procedure

The unsaturated PEs listed in Table 3-1 were autoxidized to produce OxPEs. The reported method for autoxidation of lipids<sup>3</sup> was modified by performing the reaction directly on the stainless-steel MALDI plate rather than in glass vials, thereby simplifying sample preparation. For the 0 h time point, 1  $\mu\text{L}$  aliquots of each of the 100 ppm PE standards were pipetted atop individual sample wells on the MALDI target plate, immediately followed by 1  $\mu\text{L}$  of the MALDI matrix solution. For the 48 h autoxidation, 1  $\mu\text{L}$  aliquots of each of the 100 ppm PE standards were pipetted atop individual sample wells on the MALDI target plate, the solvent was evaporated under a gentle stream of nitrogen, and the lipid residue was exposed to ambient air and light for 48 h. Immediately following autoxidation, 1  $\mu\text{L}$  of the MALDI matrix solution was deposited atop the autoxidized PE standards.

## **MS<sup>n</sup> Experimental Parameters**

All mass spectra were acquired in positive ion mode using a Thermo Scientific MALDI LTQ XL (San Jose, CA) with an intermediate-pressure MALDI source (75 mTorr) and a LIT mass analyzer. The MALDI source was equipped with a nitrogen laser ( $\lambda = 337$  nm) with a 60-Hz repetition rate and 100- $\mu$ m laser spot diameter. For these experiments, laser energies between 3 and 10  $\mu$ J per laser shot and 3 laser shots per raster spot were used. Furthermore, all mass spectra were collected in profile mode.

MS<sup>2</sup> experiments were performed using a precursor ion isolation width of 1.2 u. For MS<sup>3</sup> analysis, the precursor ion isolation width for the first and second isolation events were adjusted to 1.5 and 2.0 u, respectively. For MS<sup>4</sup>, isolation widths for the first, second, and third isolation events were 1.5, 2.0, and 2.5 u, respectively. Each mass spectrum presented in this work represents an average of 50 analytical scans.

Collision-induced dissociation (CID) was used to perform MS<sup>2</sup>, MS<sup>3</sup>, and MS<sup>4</sup> experiments. Normalized collision energies were optimized to achieve maximum product ion intensity and ranged from 29–45%. In general, the precursor ion intensity was decreased to ca. 1–10% of the most intense fragment ion.

## **Results and Discussion**

### **Autoxidation of POPE, PLPE, PDPE, and SDPE**

Table 3-2 summarizes the oxidation products observed following 48 h of autoxidation of the unsaturated PEs listed in Table 3-1. Due to prolonged storage, SDPE was already oxidized prior to the 48 h autoxidation method. Thus, all other lipid standards were autoxidized and analyzed within one month of purchasing. The most abundant oxidation products observed for each PE resulted from oxidative modification at the first double bond position in the *sn*-2 substituent, as previously reported.<sup>35</sup> For

POPE and PLPE, the most abundant OxPEs resulted from cleavage between C<sub>9</sub> and C<sub>10</sub> of the unsaturated *sn*-2 substituent (PONPE and PAzPE). PDPE and SDPE, on the contrary, yielded OxPEs resulting primarily from cleavage between C<sub>4</sub> and C<sub>5</sub> of the unsaturated *sn*-2 substituent; PDPE autoxidation produced POBPE and PSuPE and SDPE autoxidation produced SOBPE and SSuPE.

The mass spectrum obtained before and after 48 h autoxidation of POPE is depicted in Figure 3-1. Although two ions corresponding to PONPE (*m/z* 630 and 652) are observed prior to oxidation (Figure 3-1A), the relative abundances of ions corresponding to the proposed oxidation products, including PAzPE at *m/z* 646 and 668 are higher following autoxidation (Figure 3-1B). Additionally, the relative abundances of the [M+H]<sup>+</sup>, [M+Na]<sup>+</sup>, and [M-H+2Na]<sup>+</sup> ions of intact POPE, observed at *m/z* 718, 740 and 762, respectively, decreased following autoxidation. Although low in intensity due to the addition of sodium acetate to the matrix, the [M+H]<sup>+</sup> ions of each of the short-chain OxPEs were observed; however, MS<sup>n</sup> of most of these ions did not yield informative fragmentation. Thus, fragmentation of the monosodiated ([M+Na]<sup>+</sup>) and disodiated ([M-H+2Na]<sup>+</sup>) ions were investigated in this work.

### **MS<sup>n</sup> of [M+Na]<sup>+</sup> Ions of OxPEs**

MS<sup>n</sup> fragmentation of OxPEs was dependent on the type of modification to the *sn*-2 substituent (terminal aldehyde or carboxylic acid) and the length of the oxidatively modified *sn*-2 substituent. Following MS<sup>2</sup> of the [M+Na]<sup>+</sup> ion of each of the OxPEs, the most abundant MS<sup>2</sup> product ion was isolated and fragmented by CID to produce MS<sup>3</sup> spectra. MS<sup>4</sup> was acquired by selecting the most abundant MS<sup>3</sup> product ion for further fragmentation. By performing multiple stages of MS, characteristic fragmentation pathways were determined for each of the OxPEs investigated.

Figure 3-2 depicts the MS<sup>n</sup> fragmentation of the [M+Na]<sup>+</sup> ion of PAzPE produced from autoxidation of POPE. Following CID, [PAzPE+Na]<sup>+</sup> (*m/z* 646) fragmented similarly to the [M+Li]<sup>+</sup> ions of unoxidized PEs,<sup>121</sup> yielding MS<sup>2</sup> product ions resulting from NLs of aziridine (C<sub>2</sub>H<sub>5</sub>N; 43 u), dehydrated phosphoethanolamine (C<sub>2</sub>H<sub>6</sub>NO<sub>3</sub>P; 123 u) phosphoethanolamine (C<sub>2</sub>H<sub>8</sub>NO<sub>4</sub>P; 141 u) and the *sn*-1 moiety (C<sub>16</sub>H<sub>32</sub>O<sub>2</sub>; 256 u) at *m/z* 603, 523, 505, and 390, respectively (Figure 3-2A). MS<sup>3</sup> of [PAzPE+Na-C<sub>2</sub>H<sub>5</sub>N]<sup>+</sup> (*m/z* 646→603) resulted in one predominant product ion (*m/z* 505) resulting from a NL of phosphoric acid (H<sub>3</sub>PO<sub>4</sub>; 98 u) (Figure 3-2B). MS<sup>4</sup> of [PAzPE+Na-C<sub>2</sub>H<sub>8</sub>NO<sub>4</sub>P]<sup>+</sup> (*m/z* 646→603→505) produced structurally informative product ions that included *m/z* 279 ([*sn*-1+Na]<sup>+</sup>), 249 (NL of *sn*-1; 256 u), 227 (NL of *sn*-1 and Na; 278 u), and 211 ([*sn*-2+Na]<sup>+</sup>) (Figure 3-2C). These MS<sup>4</sup> product ions allowed for identification of fatty acid substituents, providing confirmation of the oxidative modification to the *sn*-2 moiety.

Likewise, MS<sup>n</sup> of the [M+Na]<sup>+</sup> ions of PSuPE and SSuPE, which are the carboxylic acid-containing oxidation products of PDPE and SDPE, respectively, also yielded informative product ion spectra (Figure 3-3 and 3-4). MS<sup>2</sup> of [PSuPE+Na]<sup>+</sup> at *m/z* 576 (Figure 3-3A) and [SSuPE+Na]<sup>+</sup> at *m/z* 604 (Figure 3-4A) also yielded product ions analogous to those reported above for PAzPE; a predominant NL of 43 u was observed followed by NLs of 141 u and 123 u. As expected, MS<sup>3</sup> of [PSuPE+Na-C<sub>2</sub>H<sub>5</sub>N]<sup>+</sup> (*m/z* 576→533; Figure 3-3B) and [SSuPE+Na]<sup>+</sup> (*m/z* 604→561; Figure 3-4B) resulted in one predominant product ion corresponding to the NL of 98 u; however, an additional product ion corresponding to the NL of the oxidized *sn*-2 moiety (118 u) was observed in the MS<sup>3</sup> spectrum from PSuPE and SSuPE at *m/z* 415 and 443, respectively. Since this fragmentation pathway was not observed for PAzPE, the

NL of the *sn*-2 substituent in MS<sup>3</sup> appears to be dependent on the *sn*-2 acyl chain length.

MS<sup>4</sup> of [PSuPE+Na-C<sub>2</sub>H<sub>8</sub>NO<sub>4</sub>P]<sup>+</sup> (*m/z* 576→533→435; Figure 3-3C) and [SSuPE+Na-C<sub>2</sub>H<sub>8</sub>NO<sub>4</sub>P]<sup>+</sup> (*m/z* 604→561→463; Figure 3-4C) produced numerous structurally informative product ions related to the *sn*-1 and *sn*-2 moieties. In contrast to PAzPC, the predominant MS<sup>4</sup> product ions from PSuPE and SSuPE resulted from cleavage of the *sn*-2 substituent rather than the *sn*-1. These product ions resulted from the NL of 100 u (C<sub>4</sub>H<sub>4</sub>O<sub>3</sub>) and 122 u (C<sub>4</sub>H<sub>3</sub>NaO<sub>3</sub>) from the *sn*-2 substituents. Also, both of these OxPEs yielded an abundant MS<sup>4</sup> product ion at *m/z* 141 that was identified as the [*sn*-2+Na]<sup>+</sup> ion.

In addition to the carboxylic acid-containing OxPEs, aldehyde-containing OxPEs were also interrogated by MS<sup>n</sup>. MS<sup>2</sup>, MS<sup>3</sup>, and MS<sup>4</sup> spectra of the [PONPE+Na]<sup>+</sup>, a product of both POPE and PLPE autoxidation, are shown in Figure 3-5A, 3-5B, and 3-5C, respectively. Unexpectedly, MS<sup>2</sup> of the precursor ion at *m/z* 630 resulted in an abundant NL of 18 u (*m/z* 612) corresponding to the loss of water. Product ions resulting from the NLs of 43 (*m/z* 587) and 141 u (*m/z* 489) were also observed, but were of much lower abundance than *m/z* 612 (Figure 3-5A). This loss of water is proposed to result from the gas-phase reaction of the primary amine with the carbonyl carbon forming a macrocycle as shown in Figure 3-5B.

MS<sup>3</sup> was performed on the [PONPE+Na-C<sub>2</sub>H<sub>5</sub>N]<sup>+</sup> ion (*m/z* 630→612) and resulted in a dominant product ion at *m/z* 514 (NL of phosphoric acid; 98 u) and lower abundant product ions at *m/z* 492 (NL of sodium dihydrogen phosphate; 120 u), 415 (NL of *sn*-2 and C<sub>2</sub>H<sub>5</sub>N; 197 u), 374 (NL of *sn*-1 ketene; 238 u), and 356 (NL of *sn*-1 free

fatty acid; 256 u) as displayed in Figure 3-5B. The observed MS<sup>3</sup> product ion at  $m/z$  514 supported the proposed macrocycle formation as one would not expect the loss of phosphoric acid without the remaining portion of the ethanolamine headgroup from a non-cyclic structure. Additionally, the product ion at  $m/z$  415 supported the proposed reaction of the primary amine in the headgroup with the carbonyl carbon of the oxidized *sn*-2 substituent as the NL of 197 u corresponded to the loss of the remaining *sn*-2 moiety (less water) with C<sub>2</sub>H<sub>5</sub>N from the ethanolamine headgroup.

For further structural characterization, MS<sup>4</sup> was performed on the [PONPE+Na-C<sub>2</sub>H<sub>6</sub>NO<sub>4</sub>P]<sup>+</sup> ion ( $m/z$  630→612→514; Figure 3-5C). The product ions at  $m/z$  260 (NL of *sn*-1 moiety as a ketene; 254 u) and  $m/z$  220 ([*sn*-2-H<sub>2</sub>O+C<sub>2</sub>H<sub>5</sub>N]<sup>+</sup>) confirmed that the ion at  $m/z$  514 still contained the intact *sn*-1 moiety, the *sn*-2 moiety less H<sub>2</sub>O, and C<sub>2</sub>H<sub>5</sub>N. Additionally, the product ion at  $m/z$  220 ([*sn*-2-H<sub>2</sub>O+C<sub>2</sub>H<sub>5</sub>N]<sup>+</sup>) further corroborated the proposed reaction of the primary amine with the *sn*-2 carbonyl carbon expelling water.

Similar MS<sup>n</sup> fragmentation pathways were observed for the [M+Na]<sup>+</sup> ions of POBPE and SOBPE; however, both the NL of aziridine and water were observed as abundant MS<sup>2</sup> product ions. Thus, both fragmentation pathways were followed as depicted in Figures 3-6 and 3-7. MS<sup>2</sup> of the [POBPE+Na]<sup>+</sup> ion ( $m/z$  560; Figure 3-6A) and [SOBPE+Na]<sup>+</sup> ion ( $m/z$  588; Figure 3-7A) yielded abundant product ions corresponding to the NL of water ( $m/z$  542 and 570, respectively), C<sub>2</sub>H<sub>5</sub>N ( $m/z$  517 and 545, respectively), dehydrated phosphoethanolamine ( $m/z$  437 and 465, respectively), and phosphoethanolamine ( $m/z$  419 and 447, respectively).

MS<sup>3</sup> of [POBPE+Na-C<sub>2</sub>H<sub>5</sub>N]<sup>+</sup> (*m/z* 560→517; Figure 3-6B) and [SOBPE+Na-C<sub>2</sub>H<sub>5</sub>N]<sup>+</sup> (*m/z* 588→545; Figure 3-7B) resulted mainly in a NL of 98 u, as was observed for PONPE (Figure 3-5B). Additionally, MS<sup>3</sup> product ions resulting from a NL of sodium dihydrogen phosphate (NL of 120 u) and a NL of the *sn*-2 fatty acid substituent (NL of 102 u) were observed at *m/z* 397 and 415, respectively, for POBPE and *m/z* 425 and 443, respectively, for SOBPE.

MS<sup>4</sup> of *m/z* 560→517→419 (Figure 3-6C) and *m/z* 588→545→447 (Figure 3-7C) resulted in similar fragmentation pathways and product ions that confirmed the identification of these precursor ions. Several NLs related to the *sn*-1 and *sn*-2 substituents were observed. The most abundant MS<sup>4</sup> product ion in these two spectra resulted from the NL of 84 u from the *sn*-2 substituent at *m/z* 335 and 363 for POBPE and SOBPE, respectively. Additionally, the loss of the entire *sn*-2 moiety was observed as a NL of 100 u at *m/z* 319 and 347 for POBPE and SOBPE, respectively.

Following the fragmentation pathway initiated by the loss of water in MS<sup>2</sup>, MS<sup>3</sup> of [POBPE+Na-H<sub>2</sub>O]<sup>+</sup> (*m/z* 560→542; Figure 3-6D) and [SOBPE+Na-H<sub>2</sub>O]<sup>+</sup> (*m/z* 588→570; Figure 3-7D) revealed multiple product ions that resulted from various cross-ring cleavages of the proposed macrocycle, similar to the proposed fragmentation pathways for PONPE. The most abundant MS<sup>3</sup> product ion, proposed to result from concurrent loss of part of the *sn*-2 moiety and C<sub>2</sub>H<sub>5</sub>N (*m/z* 433 for POBPE and *m/z* 461 for SOBPE), was further interrogated by MS<sup>4</sup>. MS<sup>4</sup> of *m/z* 560→542→433 (Figure 3-6E) and *m/z* 588→570→461 (Figure 3-7E) yielded various product ions that confirmed the assignment of the ions at *m/z* 433 and 461, respectively.

## MS<sup>n</sup> of [M-H+2Na]<sup>+</sup> Ions of OxPEs

CID of the [M-H+2Na]<sup>+</sup> ions of OxPEs resulted in numerous structurally informative product ions. As more comprehensive fragmentation coverage was observed for these disodiated ions, only two stages of MS (MS<sup>2</sup>) were required to identify the fatty acid composition. Ions corresponding to the NL of each of the fatty acid substituents were observed in addition to product ions corresponding to the disodiated oxidized *sn*-2 substituent. Figures 3-8 and 3-9 illustrate the MS<sup>2</sup> spectrum from [PAzPE-H+2Na]<sup>+</sup> (*m/z* 668) and [PONPE-H+2Na]<sup>+</sup> (*m/z* 652), respectively.

As evident in these two figures, MS<sup>2</sup> fragmentation pathways were dependent on the type of modification to the *sn*-2 moiety. CID of the carboxylic acid-containing OxPE, PAzPE (*m/z* 668), yielded dominant product ions resulting from the NL of aziridine (43 u), dehydrated phosphoethanolamine (123 u), and the *sn*-1 substituent concurrently with C<sub>2</sub>H<sub>5</sub>N (299 u). Conversely, CID of the aldehyde-containing OxPE (PONPE; *m/z* 652) yielded one dominant product ion resulting from the loss of the *sn*-1 fatty acid substituent (256 u). In addition to these product ions, CID of both [PAzPE-H+2Na]<sup>+</sup> and [PONPE-H+2Na]<sup>+</sup> resulted in a NL of dehydrated phosphoethanolamine and Na (C<sub>2</sub>H<sub>6</sub>NNaO<sub>3</sub>P; 145 u), NL of the *sn*-2 substituent (NL 188 u for PAzPE and NL of 172 u for PONPE), and a product ion corresponding to the disodiated *sn*-2 substituent (*m/z* 233 and 217 for PAzPE and PONPE, respectively). The product ions marked with asterisks in Figures 3-8 and 3-9 indicate the concurrent NL of one of the fatty acid substituent and 43 u from the PE headgroup.

Furthermore, product ions at lower relative abundances suggested more than one potential structure for the ion at *m/z* 652. Again, the presence of a terminal aldehyde led to product ions corresponding to the loss of phosphoric acid (NL of 98 u)

(without the remainder of the PE headgroup) and the loss of the sodiated *sn*-2 substituent with C<sub>2</sub>H<sub>5</sub>N (NL of 237 u). Thus, the PONPE ion at *m/z* 652 likely has two conformations: one cyclic and one non-cyclic.

Figures 3-10 and 3-11 illustrate the MS<sup>2</sup> spectrum from [PSuPE-H+2Na]<sup>+</sup> (*m/z* 598) and [POBPE-H+2Na]<sup>+</sup> (*m/z* 582), respectively. These spectra again illustrate the effect of the terminal *sn*-2 functional group on the fragmentation pathways observed and, upon comparison with Figures 3-8 and 3-9, indicate that the *sn*-2 acyl chain length has a direct impact upon fragmentation. As described above for the [M+Na]<sup>+</sup> ions, CID of the shorter-chain OxPEs (PSuPE and POBPE) resulted in a greater number of cleavages related to the *sn*-2 substituent rather than the *sn*-1 substituent as observed for the 9-carbon-containing OxPEs (PAzPE and PONPE). The primary difference in the MS<sup>2</sup> fragmentation pathways of carboxylic acid-containing OxPE (PSuPE) and the aldehyde-containing OxPE (POBPE) was the site of cleavage of the oxidized *sn*-2 substituent. CID of [POBPE-H+2Na]<sup>+</sup> resulted in a primary product ion at *m/z* 480, corresponding to the NL of the *sn*-2 as the free fatty acid. In contrast, CID of [PSuPE-H+2Na]<sup>+</sup> resulted in a primary production ion at *m/z* 498, corresponding to the NL of the *sn*-2 from the other side of the glycerol oxygen.

These same trends were observed for the analogous precursor ions of SSuPE (*m/z* 626; Figure 3-12) and SOBPE (*m/z* 610; Figure 3-13). Namely, the most abundant product ions resulted from cleavage of the *sn*-2 moiety rather than *sn*-1. Furthermore, the aldehyde-containing OxPE (SOBPE) preferentially lost the *sn*-2 as the free fatty acid whereas the carboxylic acid-containing OxPE (SOBPE) lost the *sn*-2 moiety without the glycerol oxygen.

## Conclusions

MALDI MS of autoxidized PE standards revealed two major oxidation products for each of the unsaturated PEs studied, and MS<sup>n</sup> fragmentation patterns allowed for structural characterization of these oxidation products. For the [M+Na]<sup>+</sup> a NL of water in MS<sup>2</sup> and NL of the *sn*-2 moiety concurrently with C<sub>2</sub>H<sub>5</sub>N in MS<sup>3</sup> were only observed for PE oxidation products containing a terminal aldehyde and not those containing a terminal carboxylic acid. Thus, a novel fragmentation pathway resulting in the formation of a macrocycle is proposed for oxidized PEs containing a terminal aldehyde on the *sn*-2 fatty acid substituent.

Additionally, the relative abundance of the macrocyclic structure increased as a function of *sn*-2 chain length, as demonstrated by the MS<sup>2</sup> fragmentation of PONPE and POBPE. This trend correlates with previously reported observations for b<sub>n</sub> peptide ions, in which the relative abundance of the macrocyclic structure increased as a function of fragment size.<sup>122</sup> Lastly, MS<sup>2</sup> of the disodiated oxidized PE ions provided better fragmentation coverage than MS<sup>2</sup> of singly sodiated oxidized PE ions.

The MALDI MS<sup>n</sup> technique developed in this work for identifying OxPEs resulting from autoxidation is expected to be directly applicable to detecting and identifying in situ OxPEs in biological tissues such as the retina. Future studies will aim to identify and quantify OxPEs in retina tissue by MALDI MS<sup>n</sup> and mass spectrometric imaging. These studies may potentially provide insight into the involvement of lipid oxidation, specifically OxPEs, in aging of the retina and diseases such as AMD.

Table 3-1. PE standards autoxidized and analyzed.<sup>a</sup>

Chemical Name [Shorthand]	Monoisotopic Mass	R <sub>1</sub>	R <sub>2</sub>
1-palmitoyl-2-oleoyl- <i>sn</i> -glycero-3-phosphoethanolamine [POPE]	717.53	16:0	18:1
1-palmitoyl-2-linoleoyl- <i>sn</i> -glycero-3-phosphoethanolamine [PLPE]	715.52	16:0	18:2
1-palmitoyl-2-docosahexaenoyl- <i>sn</i> -glycero-3-phosphoethanolamine [PDPE]	763.52	16:0	22:6
1-stearoyl-2-docosahexaenoyl- <i>sn</i> -glycero-3-phosphoethanolamine [SDPE]	791.55	18:0	22:6

<sup>a</sup> Nomenclature according to the LIPID MAPS systematic naming is used ([www.lipidmaps.org](http://www.lipidmaps.org)). R<sub>1</sub> and R<sub>2</sub> represent the number of carbons and double bonds (#C:#DB) in the fatty acid substituents esterified to the *sn*-1 and *sn*-2 position of the glycerol backbone, respectively.

Table 3-2. Nomenclature of the observed PE oxidation products.<sup>a</sup>

Observed Oxidation Products [Shorthand]	Monoisotopic Mass	R <sub>1</sub>	R <sub>2</sub> '	Products of: <sup>b</sup>
1-palmitoyl-2-(9-oxo-nonanoyl)- <i>sn</i> -glycero-3-phosphoethanolamine [PONPE]	607.38	16:0	9:0 (CHO)	POPE, PLPE
1-palmitoyl-2-azelaoyl- <i>sn</i> -glycero-3-phosphoethanolamine [PAzPE]	623.38	16:0	9:0 (COOH)	POPE, PLPE
1-palmitoyl-2-(4-oxo-butyroyl)- <i>sn</i> -glycero-3-phosphoethanolamine [POBPE]	537.31	16:0	4:0 (CHO)	PDPE
1-palmitoyl-2-succinoyl- <i>sn</i> -glycero-3-phosphoethanolamine [PSuPE]	553.30	16:0	4:0 (COOH)	PDPE
1-stearoyl-2-(4-oxo-butyroyl)- <i>sn</i> -glycero-3-phosphoethanolamine [SOBPE]	565.34	18:0	4:0 (CHO)	SDPE
1-stearoyl-2-succinoyl- <i>sn</i> -glycero-3-phosphoethanolamine [SSuPE]	581.33	18:0	4:0 (COOH)	SDPE

<sup>a</sup> R<sub>1</sub> represents the number of carbons and double bonds (#C:#DB) in the fatty acid substituents esterified to the *sn*-1 position of the glycerol backbone. R<sub>2</sub>' represents the number of carbons and double bonds in the oxidatively truncated *sn*-2 fatty acid substituent.

<sup>b</sup> These PE oxidation products are produced from oxidative cleavage along the unsaturated *sn*-2 fatty acid of POPE, PLPE, PDPE, or SDPE and result in addition of a terminal aldehyde (CHO) or carboxyl group(COOH).

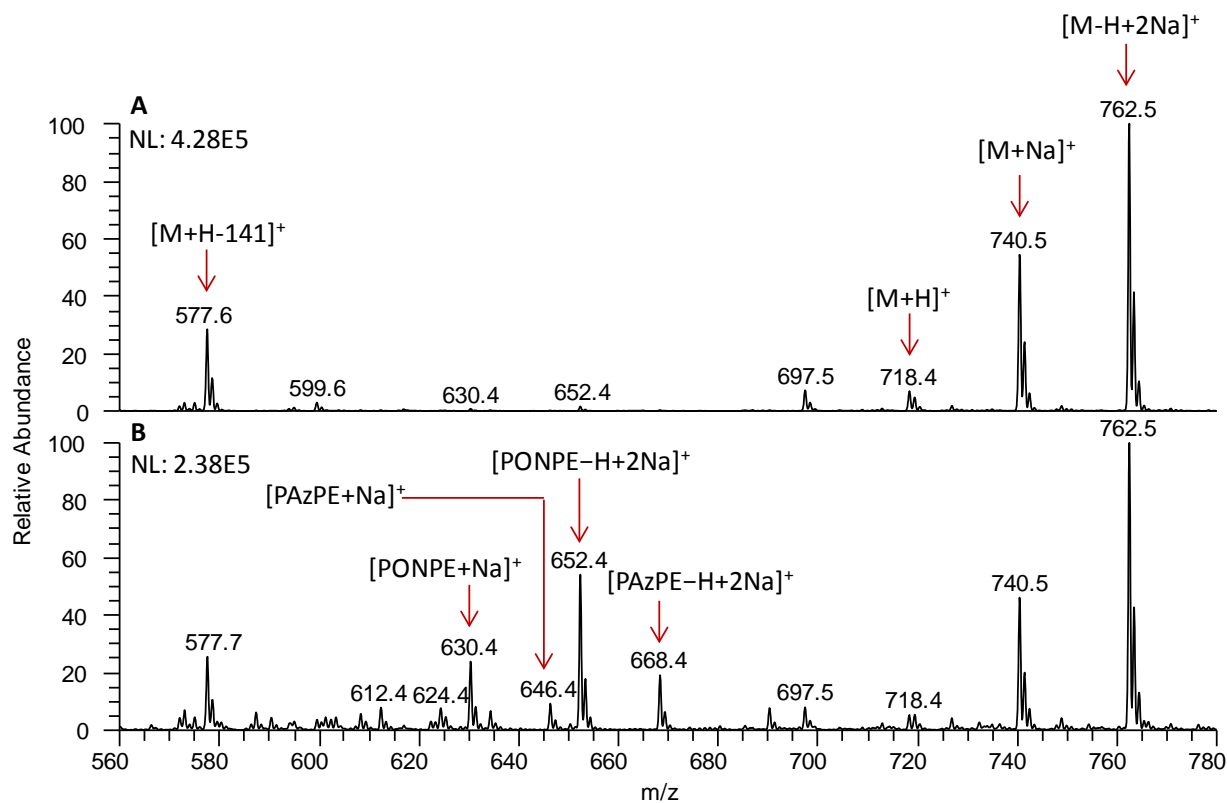


Figure 3-1. MS spectrum of POPE A) before and B) after autoxidation. A decrease in the relative abundances of ions corresponding to intact POPE and an increase in the relative abundances of POPE oxidation products were observed.

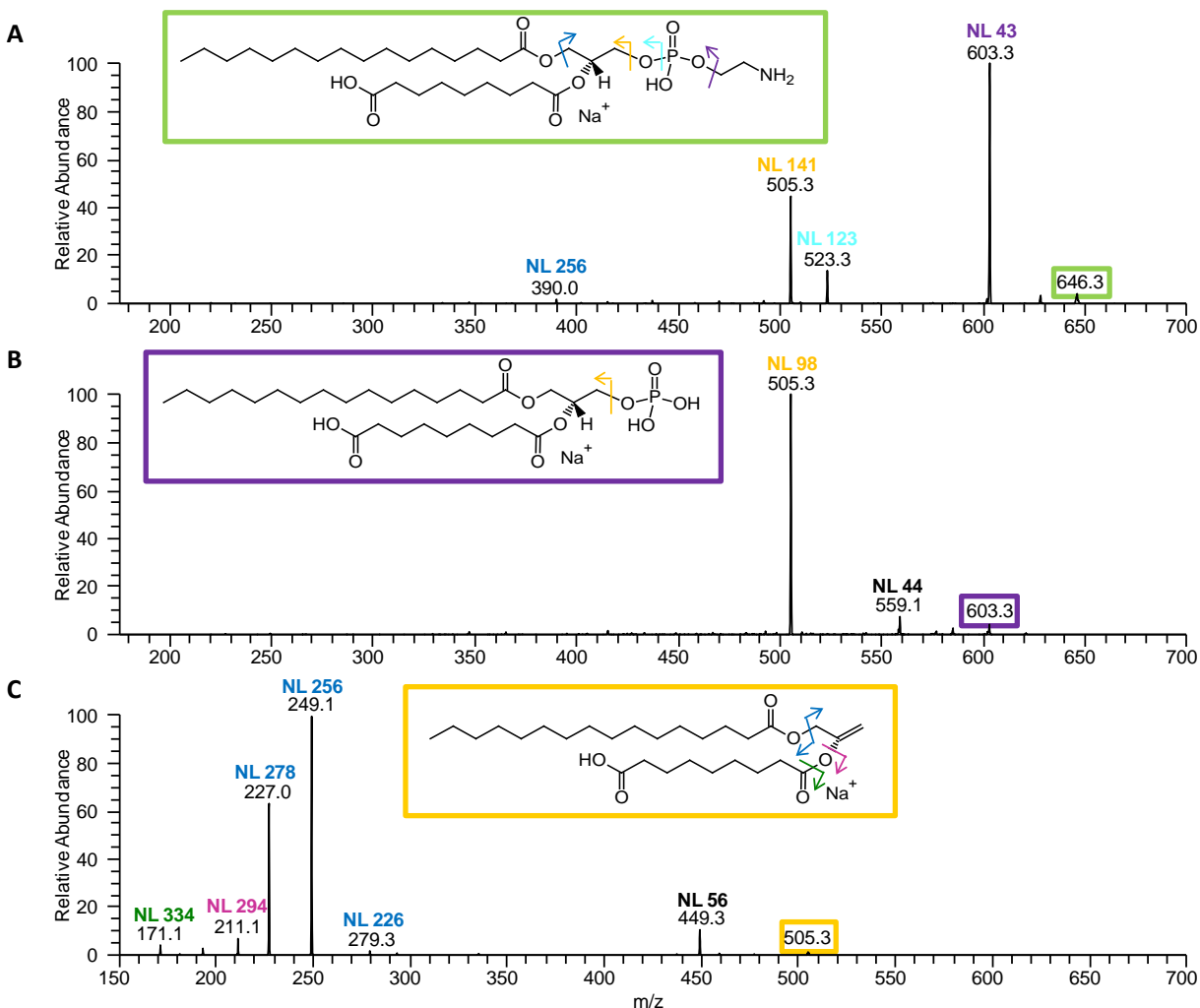


Figure 3-2. Fragmentation pattern of  $[PAzPE+Na]^+$  from autoxidized POPE. A)  $MS^2$  of  $m/z$  646 results in a NL of 43 u ( $m/z$  603) corresponding to the loss of aziridine, which is typically the most abundant loss observed from sodiated PEs. B) Fragment ions observed in  $MS^3$  of  $m/z$  646 $\rightarrow$ 603, and C)  $MS^4$  of  $m/z$  646 $\rightarrow$ 603 $\rightarrow$ 505 support the identification of  $m/z$  646 as  $[PAzPE+Na]^+$ . The proposed structures of the ions undergoing fragmentation and the sites of fragmentation are also shown.

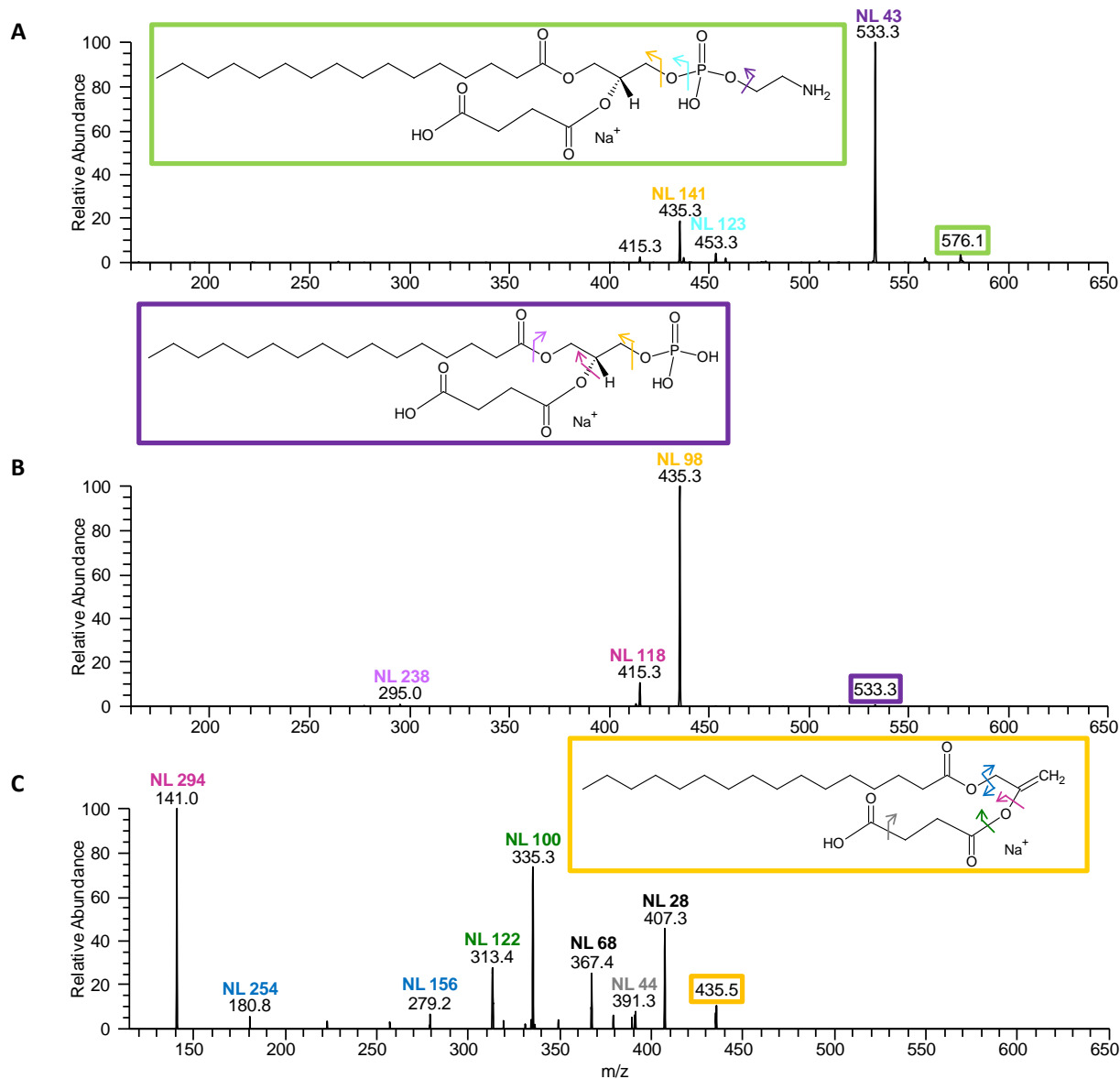


Figure 3-3. Fragmentation pattern of  $[\text{PSuPE}+\text{Na}]^+$  from autoxidized PDPE. A)  $\text{MS}^2$  of  $m/z$  576 results in a NL of 43 u ( $m/z$  533) corresponding to the loss of aziridine, which is typically the most abundant loss observed from sodiated PEs. B) Fragment ions observed in  $\text{MS}^3$  of  $m/z$  576 $\rightarrow$ 533 and C)  $\text{MS}^4$  of  $m/z$  576 $\rightarrow$ 533 $\rightarrow$ 435 support the identification of  $m/z$  576 as  $[\text{PSuPE}+\text{Na}]^+$ . The proposed structures of the precursor ions and the sites of fragmentation are also shown.

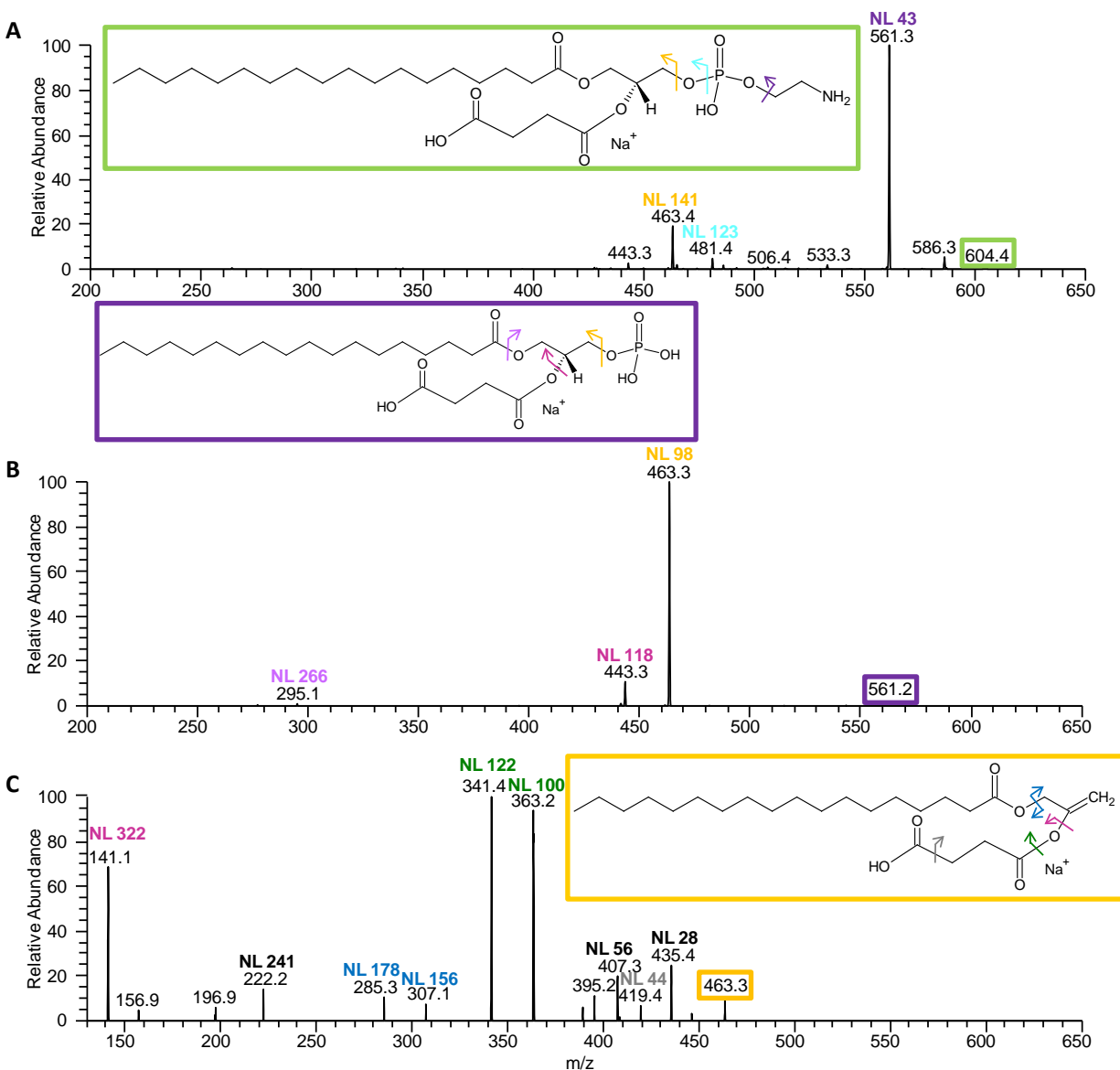


Figure 3-4. Fragmentation pattern of  $[\text{SSuPE}+\text{Na}]^+$  from autoxidized SDPE. A)  $\text{MS}^2$  of  $m/z$  604 results in a NL of 43 u ( $m/z$  561) corresponding to the loss of aziridine, which is typically the most abundant loss observed from sodiated PEs. B) Fragment ions observed in  $\text{MS}^3$  of  $m/z$  604 $\rightarrow$ 561 and C)  $\text{MS}^4$  of  $m/z$  604 $\rightarrow$ 561 $\rightarrow$ 463 support the identification of  $m/z$  604 as  $[\text{SSuPE}+\text{Na}]^+$ . The proposed structures of the precursor ions and the sites of fragmentation are also shown.

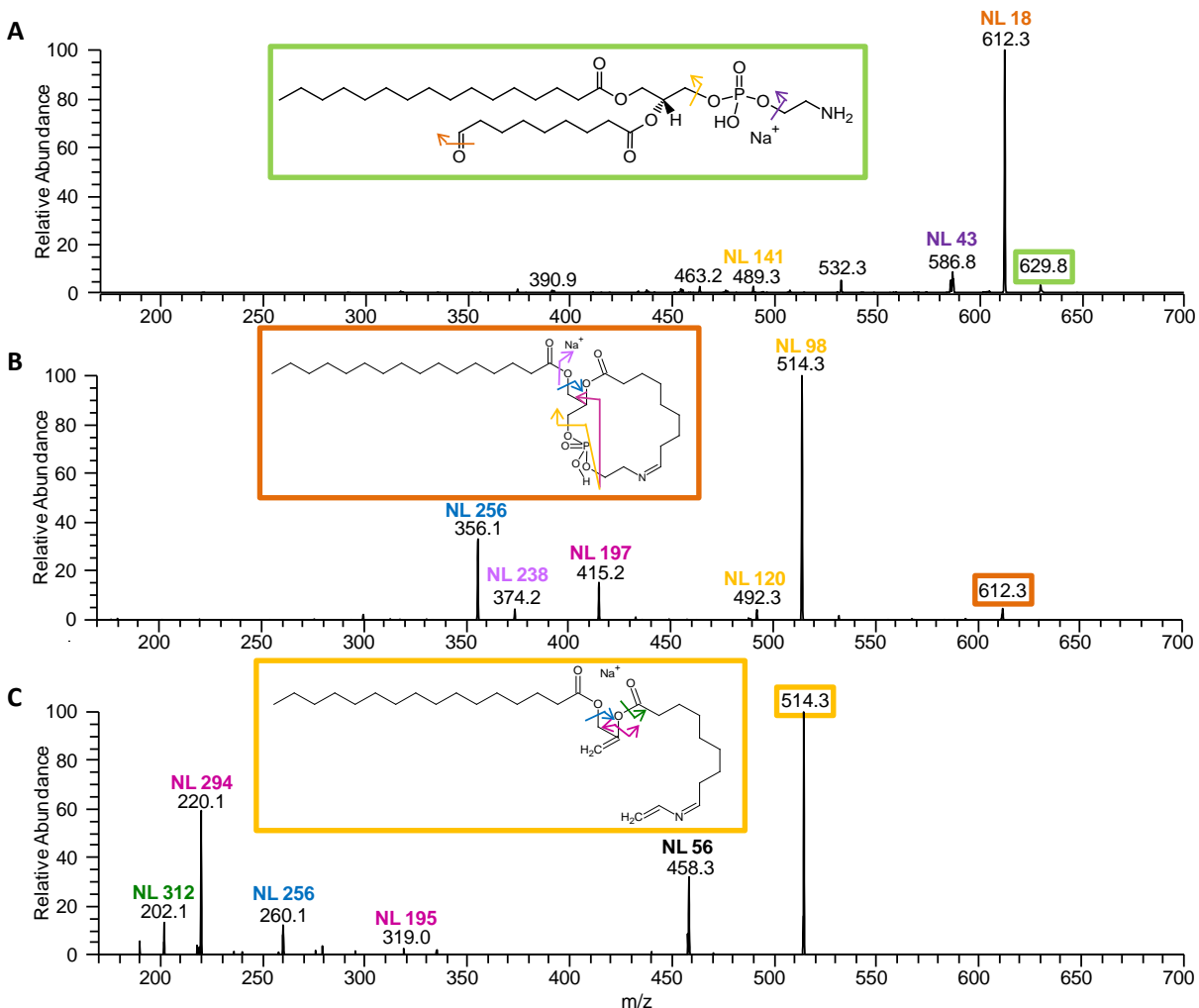


Figure 3-5. Fragmentation pattern of  $[PONPE+Na]^+$  from autoxidized POPE. A)  $MS^2$  of  $m/z$  630 results in an abundant NL of 18 u ( $m/z$  612) corresponding to a loss of water, which suggests the reaction of the primary amine with the carbonyl carbon resulting in the formation of a macrocycle. B) Fragment ions observed in  $MS^3$   $m/z$  630 $\rightarrow$ 612 and C)  $MS^4$   $m/z$  630 $\rightarrow$ 612 $\rightarrow$ 514 support this hypothesis. The proposed structures of the ions undergoing fragmentation and the sites of fragmentation are also shown.

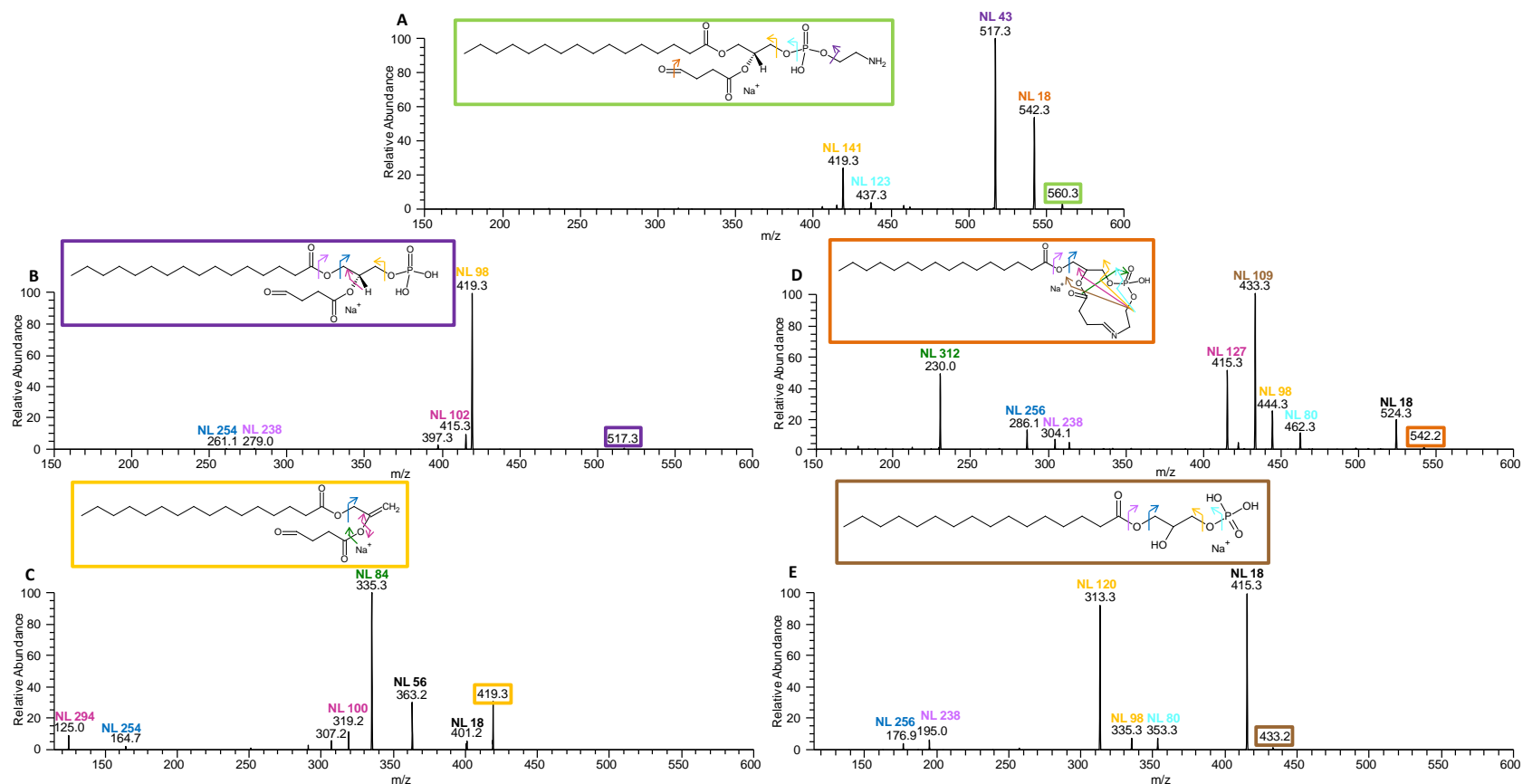


Figure 3-6. Fragmentation pattern of  $[\text{POBPE}+\text{Na}]^+$  ( $m/z$  560) from autoxidized PDPE. A)  $\text{MS}^2$  of  $m/z$  560 yields fragment ions typically observed for sodiated PEs (NLs of 43, 123, 141, and 256 u); however, the ion resulting from a loss of water (NL of 18 u) is also an abundant fragment suggesting POBPE may form a macrocycle similar to PONPE. B)  $\text{MS}^3$  of  $m/z$  560  $\rightarrow$  517 results mainly in a NL of 98 u, typical for a sodiated PE. C)  $\text{MS}^4$  of  $m/z$  560  $\rightarrow$  517  $\rightarrow$  419 results in NLs from the *sn*-1 and *sn*-2 tails confirming the identification of this ion. D)  $\text{MS}^3$  of  $m/z$  560  $\rightarrow$  542 yields fragmentation pathways similar to those proposed for PONPE, many of which are cross-ring cleavages of the macrocycle. E)  $\text{MS}^4$   $m/z$  560  $\rightarrow$  542  $\rightarrow$  433 confirms the assignment of  $m/z$  433; NLs corresponding to the *sn*-2 tail are not observed. The proposed structures of the precursor ions and the sites of fragmentation are shown.

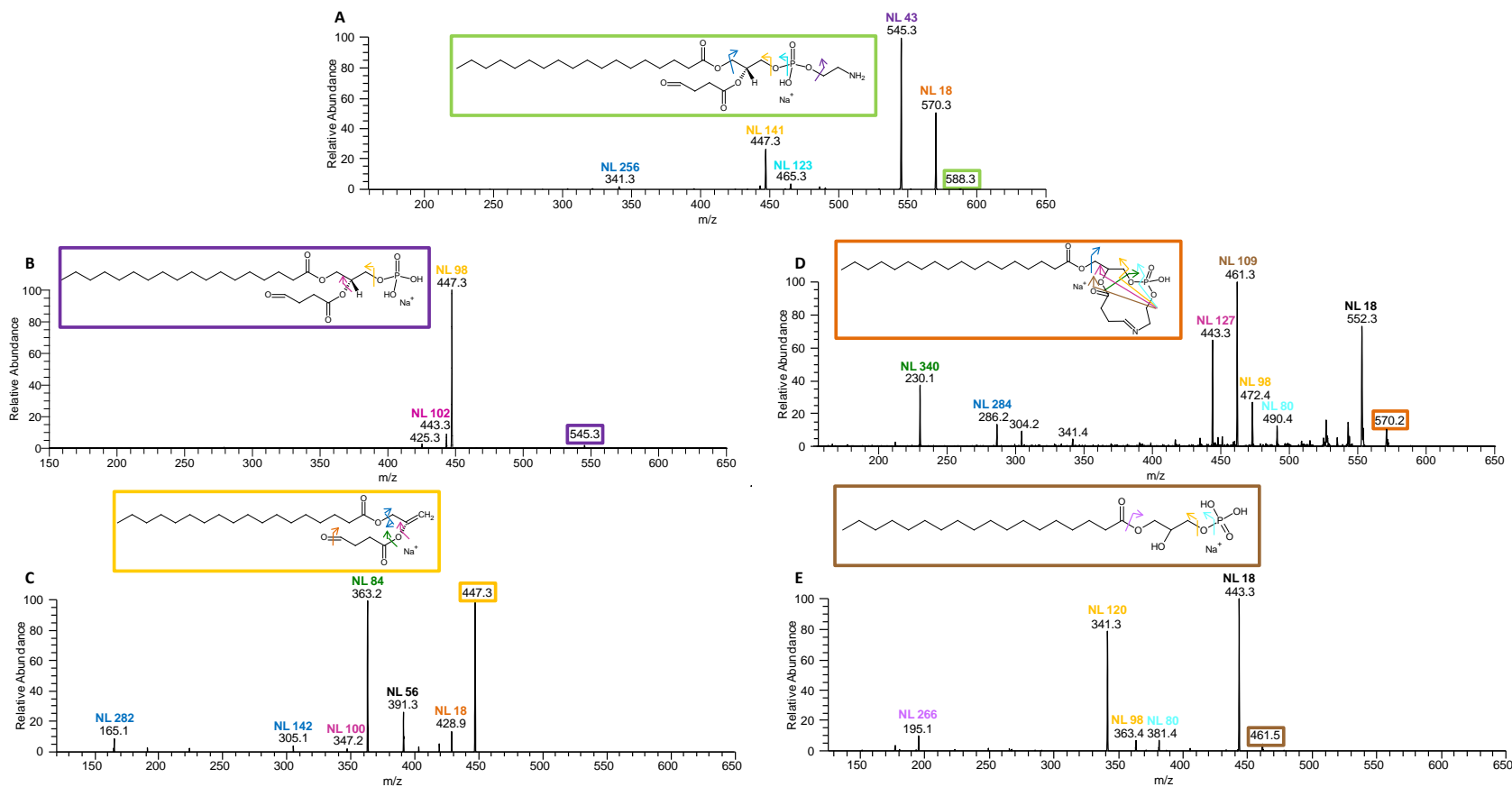


Figure 3-7. Fragmentation pattern of  $[\text{SOBPE}+\text{Na}]^+$  ( $m/z$  588) from autoxidized SDPE. A)  $\text{MS}^2$  of  $m/z$  588 yields fragment ions typically observed for sodiated PEs (NL of 43, 123, 141, 256 u); however, the ion resulting from a loss of water (NL of 18 u) is also an abundant fragment suggesting SOBPE may form a macrocycle similar to PONPE. B)  $\text{MS}^3$  of  $m/z$  588  $\rightarrow$  545 results mainly in a NL of 98 u, typical for a sodiated PE. C)  $\text{MS}^4$  of  $m/z$  588  $\rightarrow$  545  $\rightarrow$  447 results in neutral losses from the *sn*-1 and *sn*-2 tails confirming the identification of this ion. D)  $\text{MS}^3$  of  $m/z$  588  $\rightarrow$  570 yields fragmentation pathways similar to those proposed for PONPE, many of which are cross-ring cleavages of the macrocycle. E)  $\text{MS}^4$   $m/z$  588  $\rightarrow$  570  $\rightarrow$  461 confirms the assignment of  $m/z$  461; NLS corresponding to the *sn*-2 tail are not observed. The proposed structures of the ions undergoing fragmentation and the sites of fragmentation are shown.

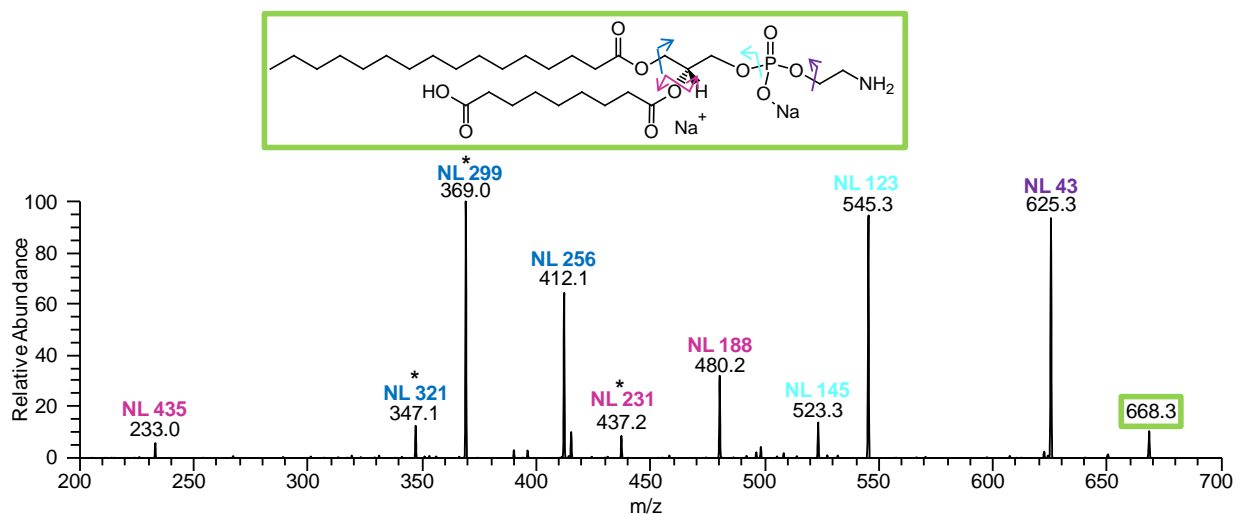


Figure 3-8. MS<sup>2</sup> fragmentation of [PAzPE-H+2Na]<sup>+</sup> (*m/z* 668) from autoxidized POPE. The proposed structure and sites of fragmentation are also shown. Product ions marked with an asterisk indicate the concurrent NL of one of the fatty acid substituents and part of the PE headgroup (C<sub>2</sub>H<sub>5</sub>N; 43 u).

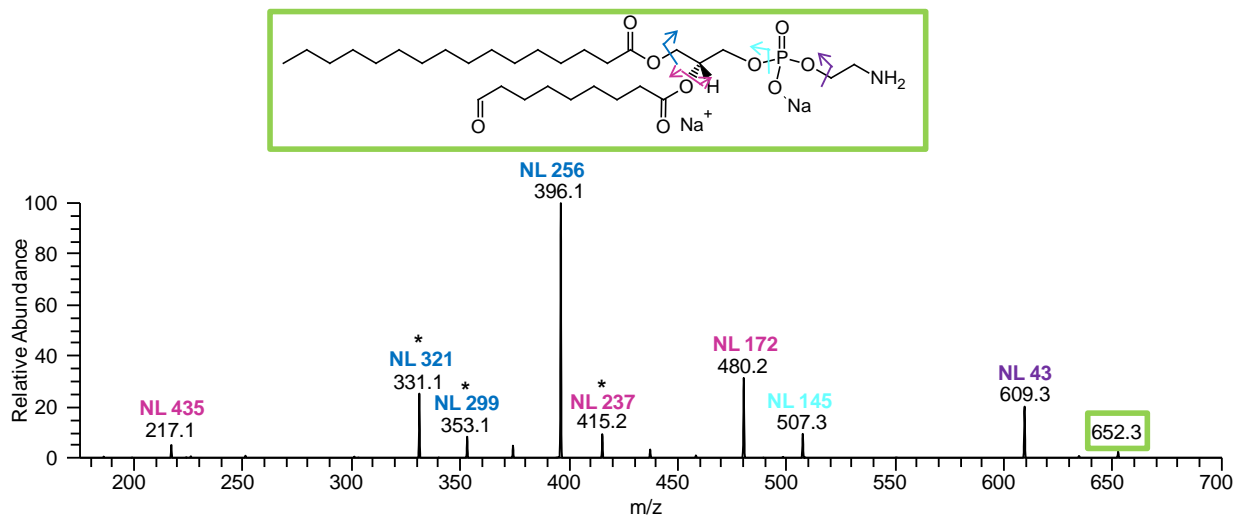


Figure 3-9. MS<sup>2</sup> fragmentation of [PONPE-H+2Na]<sup>+</sup> (*m/z* 652) from autoxidized POPE. The proposed structure and sites of fragmentation are also shown. Product ions marked with an asterisk indicate the concurrent NL of one of the fatty acid substituents and part of the PE headgroup (C<sub>2</sub>H<sub>5</sub>N; 43 u).

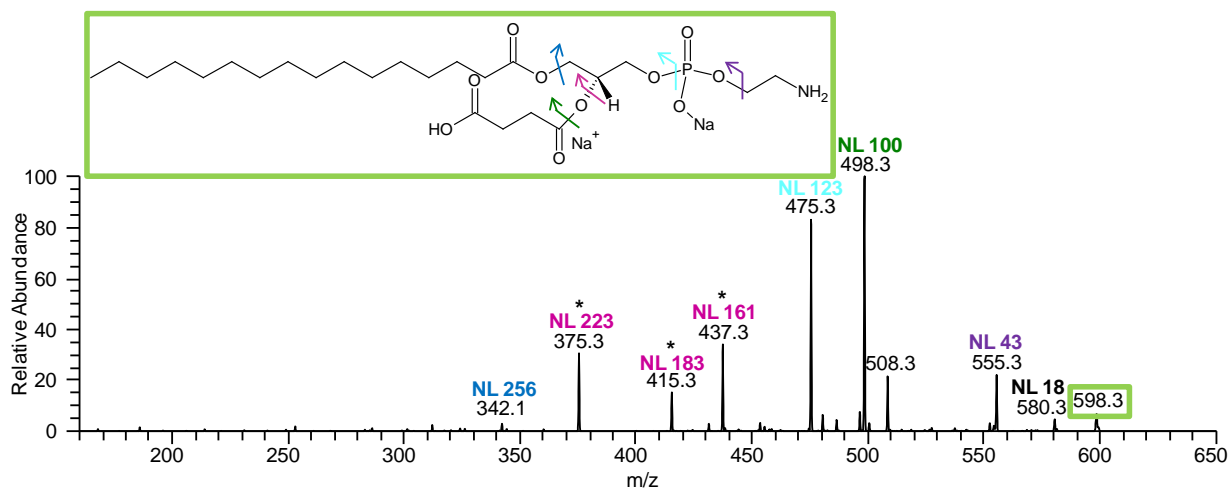


Figure 3-10. MS<sup>2</sup> fragmentation of [PSuPE-H+2Na]<sup>+</sup> (*m/z* 598) from autoxidized PDPE. The proposed structure and sites of fragmentation are also shown. Product ions marked with an asterisk indicate the concurrent NL of one of the fatty acid substituents and part of the PE headgroup (C<sub>2</sub>H<sub>5</sub>N; 43 u).

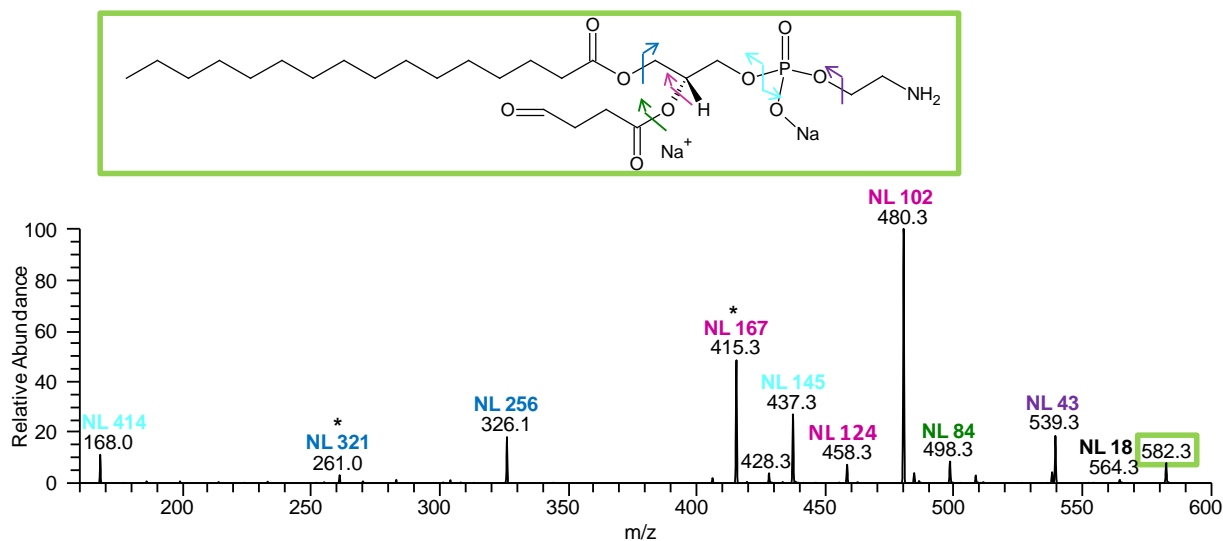


Figure 3-11. MS<sup>2</sup> fragmentation of [POBPE-H+2Na]<sup>+</sup> (*m/z* 582) from autoxidized PDPE. The proposed structure and sites of fragmentation are also shown. Product ions marked with an asterisk indicate the concurrent NL of one of the fatty acid substituents and part of the PE headgroup (C<sub>2</sub>H<sub>5</sub>N; 43 u).

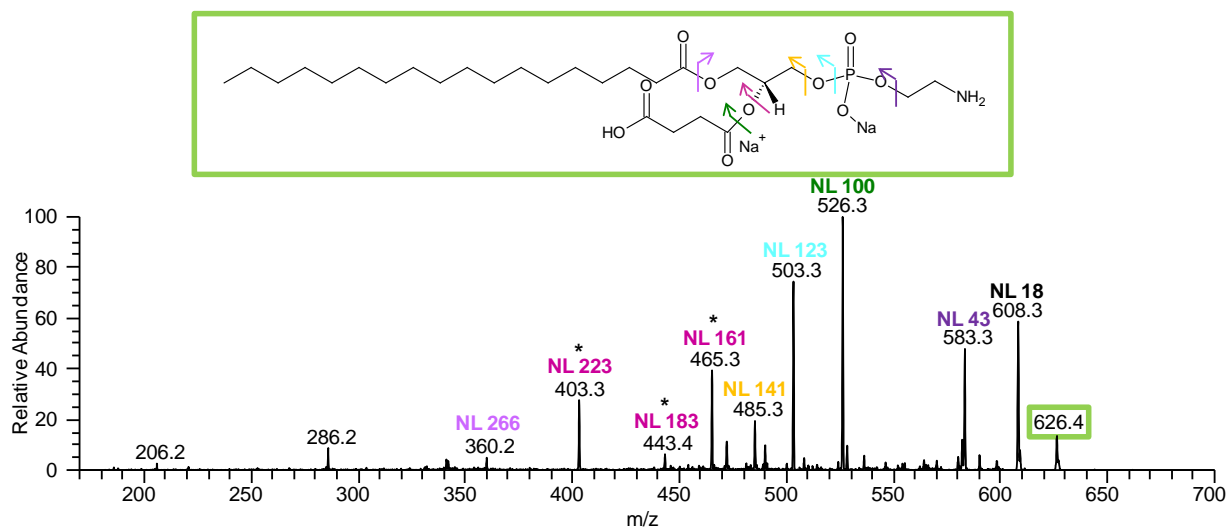


Figure 3-12. MS<sup>2</sup> fragmentation of [SSuPE-H+2Na]<sup>+</sup> (*m/z* 626) from autoxidized SDPE. The proposed structure and sites of fragmentation are also shown. Product ions marked with an asterisk indicate the concurrent NL of one of the fatty acid substituents and part of the PE headgroup (C<sub>2</sub>H<sub>5</sub>N; 43 u).

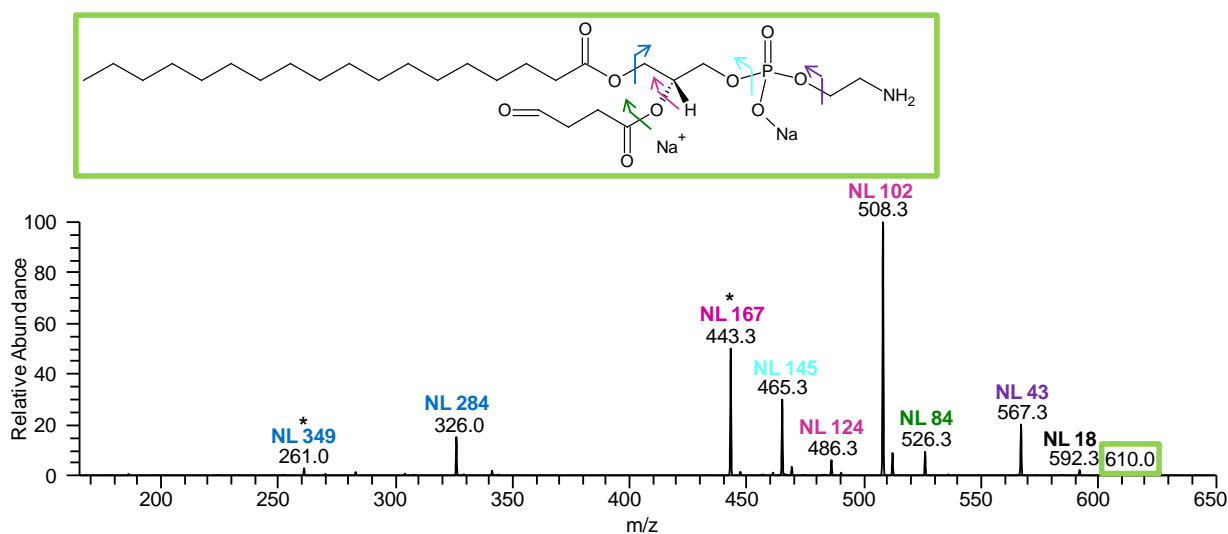


Figure 3-13. MS<sup>2</sup> fragmentation of [SOBPE-H+2Na]<sup>+</sup> (*m/z* 610) from autoxidized SDPE. The proposed structure and sites of fragmentation are also shown. Product ions marked with an asterisk indicate the concurrent NL of one of the fatty acid substituents and part of the PE headgroup (C<sub>2</sub>H<sub>5</sub>N; 43 u).

## CHAPTER 4 IDENTIFYING AND IMAGING PHOSPHOLIPID OXIDATION PRODUCTS BY MALDI MS<sup>n</sup>

### Introduction

Oxidative stress has been implicated in the pathogenesis of various human diseases.<sup>2-6</sup> In addition to DNA and proteins, unsaturated lipids are known targets of oxidative modification.<sup>123</sup> Following oxidative stress, numerous lipid oxidation products, with diverse biological activities, are formed.<sup>1,124</sup> These activities (e.g., inflammatory vs anti-inflammatory) are dependent on the chemical structure of the oxidized species.<sup>88</sup> Furthermore, free-radical production and lipid oxidation have been shown to occur in localized regions of biological tissues such as ischemic rat brain.<sup>125</sup> Thus, there is growing interest in developing methods to identify and determine the spatial distributions of individual lipid oxidation products in biological tissues.<sup>13,15</sup>

Although techniques for measuring lipid oxidation have been reported,<sup>37</sup> many of these techniques (e.g., the thiobarbituric acid assay<sup>38</sup>) suffer from poor selectivity, and are therefore ill-suited for analysis of complex biological samples.<sup>39</sup> For greater selectivity, mass spectrometric techniques have become increasingly utilized for the analysis of intact lipid oxidation products in complex sample matrices.<sup>14,37,101,126</sup> Of these techniques, reversed-phase high-performance liquid chromatography (RP-HPLC) coupled to electrospray ionization mass spectrometry (ESI MS) has become the most widely utilized, permitting both separation and selective detection of intact lipid oxidation products.<sup>15</sup> Despite these advantages, conventional ESI MS requires extraction from tissue, precluding the analysis of these oxidation products in situ. Conversely, this work demonstrates that matrix-assisted laser desorption/ionization mass spectrometry

(MALDI MS) offers the ability to perform in situ analysis and imaging of oxidized lipids in biological tissues.

Although mass spectrometric imaging (MSI) is a powerful technique for obtaining spatially-resolved chemical distributions of biomolecules in tissue, MSI typically generates large datasets that are time-consuming to process. Therefore, multivariate data analysis techniques such as principal component analysis have been employed to reduce the dimensionality of MSI datasets, allowing for unsupervised data mining.<sup>50,127,128</sup> In many cases, various regions of tissue can be differentiated using a single principal component, thereby reducing analysis time and allowing for rapid extraction of relevant information.<sup>50</sup>

In this work, in vitro oxidation was performed on thin tissue sections. Although several methods of in vitro oxidation were tested (e.g., the addition of the photosensitizer methylene blue), UV-light exposure in ambient air was found to produce lipid oxidation without requiring the addition of any chemicals (excluding the MALDI matrix) to the tissue. Following oxidation, principal component analysis (PCA) in combination with MALDI MS<sup>n</sup> and mass spectrometric imaging (MSI) was utilized to discover, identify, and localize lipid oxidation products in thin tissue sections following in vitro oxidation. As illustrated in this work, several phospholipid oxidation products are nominally isobaric, some even isomeric, with both oxidized and unoxidized phospholipids; thus, the need for the enhanced selectivity of MS<sup>n</sup> is demonstrated.

## **Experimental Methods**

### **Chemicals**

The MALDI matrix 2,5-dihydroxybenzoic acid (DHB) was purchased from Acros Organics (Geel, Belgium). Sodium acetate trihydrate (NaOAc) and HPLC-grade

methanol and water were obtained from Fisher Scientific (Fair Lawn, NJ). The MALDI matrix solution was prepared by dissolving DHB in 70:30 methanol:water to a final concentration of 40 mg/mL. To promote sodiation, NaOAc (10 mM final concentration) was added to the matrix solution.

### **Tissue Preparation**

Spinal cords from adult female Sprague-Dawley rats (Harlan, San Diego, CA) were used in these experiments. Animal studies were performed in an AAALAC-approved vivarium and were approved by the local IACUC at the University of California, San Diego. Following euthanasia, excised tissue was immediately flash-frozen in liquid nitrogen and stored at  $-80\text{ }^{\circ}\text{C}$  until sectioned at  $-25\text{ }^{\circ}\text{C}$  using a Microm HM 505E cryostat (Walldorf, Germany). Cross-sections (10  $\mu\text{m}$  thick) were obtained from the cervical region of the spinal cord and were thaw-mounted atop glass microscope slides. To remove excess water from the tissue prior to in vitro oxidation, these slides were dried in a vacuum desiccator for approximately 10 min. Although tissue is typically dried for ca. 30 min to 1 h, these longer drying times were not needed since the tissues were not coated with MALDI matrix directly after vacuum desiccation.

### **In Vitro Oxidation**

Following vacuum desiccation, the right half of the tissue was covered with an aluminum foil-wrapped microscope slide to prevent light exposure and oxidation. The glass microscope slide containing the spinal cord sections was then placed ca. 1 cm below a shortwave ( $\lambda = 254\text{ nm}$ ) mineralight lamp (model UVG 1; 1 UVP, Inc., San Gabriel, CA) and the left half was UV-irradiated in ambient air for 4 h. Immediately following this in vitro oxidation procedure, the aluminum foil was removed from the right

side of the microscope slide and MALDI matrix solution was deposited atop the tissue with a Meinhard Type A3 glass nebulizer (Golden, CO).

### **Mass Spectrometry**

All MS and MS<sup>n</sup> spectra were acquired using a Thermo Scientific MALDI LTQ XL (San Jose, Ca). This instrument was equipped with a 337-nm nitrogen laser with a 60-Hz repetition rate and a 100- $\mu$ m laser spot diameter. In these experiments, laser energies of 2.8–7.0  $\mu$ J per laser shot and 3 laser shots per raster spot were used. Additionally, MS and MS<sup>n</sup> spectra were collected in profile mode using a raster step size of 100  $\mu$ m. For MS<sup>n</sup> experiments, which were performed by collision induced dissociation (CID) with helium as the collision gas, instrumental parameters were adjusted as follows: 1.2 u isolation width for MS<sup>2</sup>, 1.5 and 2.0 u isolation widths for the first and second isolation events of MS<sup>3</sup>, 1.5, 2.0, and 2.5 u isolation widths for the first, second, and third isolation events of MS<sup>4</sup>, and normalized collision energies of 29–45%. All mass spectra were processed using Thermo Scientific QualBrowser. Following MS and MS<sup>n</sup> data collection, images were generated using Thermo Scientific ImageQuest 1.0.1 software. To account for the inherent signal variability in MALDI MS analysis of tissue, MS images were normalized to the total ion current (TIC); however, MS<sup>n</sup> images were not normalized.

### **Statistical Analysis**

Prior to MS<sup>n</sup> analysis, PCA was performed to determine *m/z* values that distinguished the UV-exposed and unexposed sides of the tissue. PCA was conducted on the MALDI MSI datasets using the ChemomeTricks toolbox developed at FOM Institute AMOLF (Amsterdam, Netherlands). MS imaging files collected on the Thermo LTQ XL were first converted to .NetCDF using the Roadmap file converter provided in

Xcalibur. Software developed at FOM Institute AMOLF was then employed to extract the data from the .NetCDF files and create Matlab compatible files (.MAT). To reduce the size of the dataset, the collected profile data were converted to centroid data using PEAPI software, which also performed peaking picking and spectral alignment.<sup>129</sup> Prior to performing PCA, the data were normalized to the TIC, mean-centered, and divided by the standard deviation of each respective variable's intensity. Additionally, *m/z* values known to be related to DHB were removed from the dataset. Following mean-centering and standardization, each pixel in the MS image was treated as a separate sample, and PCA was performed. Scores images were plotted for the first 20 principal components and 1-dimensional loadings plots were generated for principal components that demonstrated discrimination between the oxidized and control regions of the tissue.

## **Results and Discussion**

### **MS Analysis of UV-exposed and Unexposed Spinal Cord**

Presented in Figure 4-1 are representative mass spectra from the left half of the tissue, exposed to UV light for 4 h (top), and from the right half of the tissue, which was not exposed to UV light (bottom). Each spectrum was produced by averaging 20 analytical scans acquired from the respective sides of the tissue. The optical image, photographed after matrix deposition but prior to MS analysis, depicts the division in the tissue, as the UV-exposed side of the tissue appears slightly darker (Figure 4-1). Furthermore, the gray matter (butterfly shape) and white matter (area surrounding the gray matter) of the spinal cord are evident in the optical image.

Although these studies were aimed at targeting phospholipid oxidation, one overt difference in the spectra relates to the oxidation of cholesterol. Specifically, cholesterol, which is observed as the  $[M+H-18]^+$  ion (*m/z* 369) as previously reported,<sup>130</sup> was lower

in relative abundance on the UV-exposed side of the tissue. Moreover, the reported oxidation products of cholesterol, such as the oxysterols that were observed at  $m/z$  367 ( $[M+H-2H_2O]^+$ ) and  $m/z$  385 ( $[M+H-H_2O]^+$ ) and 7-ketocholesterol that was observed at  $m/z$  401 ( $[M+H]^+$ ),<sup>130,131</sup> were all higher in relative abundance on the UV-exposed side of the tissue. This difference in localization is further illustrated by the MS images in Figure 4-1; after extracting the intensity of  $m/z$  369 and  $m/z$  367 and normalizing each image to the TIC, opposite spatial distributions were observed for these two ions (Figure 4-1). Additionally, several ions corresponding to ceramides ( $m/z$  630 and 648) were lower in intensity on the UV-exposed portion of the tissue.

As hypothesized, a decrease in the relative abundance for a number of ions in the phospholipid region (ca.  $m/z$  700–900) was observed following in vitro oxidation. Despite this decrease in signal, the hypothesized oxidation products of these phospholipids (as discussed in Chapters 2 and 3) were not readily apparent above the baseline. This lack of abundant oxidation products is not unexpected, as previous studies have suggested that each unsaturated phospholipid precursor may produce at least 50 oxidation products,<sup>6</sup> effectively diluting the MS signal from each individual oxidation product. Furthermore, the inherent spectral complexity associated with tissue analysis makes identifying targets for MS<sup>n</sup> analysis challenging. Thus, PCA was employed to determine potential phospholipid oxidation products.

### **PCA of UV-exposed and Unexposed Spinal Cord**

PCA was performed on the MSI dataset using the ChemomeTricks toolbox. As illustrated in Figure 4-2, scores images from principal component 1, accounting for ca. 33% of the variance, distinguished the UV-exposed (oxidized) and unexposed (control) halves of the tissue. Accordingly, a 1-dimensional loadings plot for this principal

component was generated (Figure 4-2) to determine which ions exhibited appreciable loadings coefficients on principal component 1—the loadings coefficients provided information concerning the relative contribution of each  $m/z$  value to the separation along a principal component. Thus, ions loading positively on principal component 1 demonstrated a positive correlation with this principal component as displayed in the scores images (Figure 4-2), and are therefore expected to be higher in intensity on the UV-exposed half of the tissue. Conversely, ions loading negatively on principal component 1 demonstrate a negative correlation with principal component 1 and are therefore expected to be higher in intensity on the unexposed side of the tissue.

Several ions dictating separation between the UV-exposed and unexposed portions of the tissue were also ions that were identified as potential oxidation products based on the extracted MS spectra and MS images detailed in Figure 4-1. For example, the proposed oxidation products of cholesterol at  $m/z$  367, 385, and 401 were positively loaded on principal component 1 and demonstrated elevated intensity on the left side of the scores image (Figures 4-2). Conversely, the  $[M+H-H_2O]^+$  ion of cholesterol at  $m/z$  369 loaded negatively on principal component 1 and appeared on the right side of the scores image. Furthermore, unsaturated phospholipids, including  $[PC(16:0/18:1)+Na]^+$  ( $m/z$  782) and  $[PC(18:0/18:1)+Na]^+$  ( $m/z$  810), were negatively loaded on principal component 1 and ions 32 u higher at  $m/z$  814 and 842, respectively, were positively loaded on principal component 1. The latter two ions, proposed to be the respective peroxidation products of PC (16:0/18:1) and PC (18:0/18:1), were targeted for  $MS^n$  analysis. In addition to these long-chain products, ions corresponding to known short-chain oxidation products of phosphatidylcholines (e.g.,  $m/z$  688 and 716) also

loaded positively on principal component 1 and were therefore targeted for interrogation by MS<sup>n</sup> as well.

### **MS<sup>n</sup> Analysis of Oxidized Phospholipids in the Spinal Cord**

Based on principal component 1 loadings values, ions were selected for MS<sup>n</sup> analysis. Multiple stages of mass analysis permitted identification and localization of many of these ions within the spinal cord. Furthermore, several of these ions were detected at the same nominal mass as other endogenous species in the tissue; in these instances MS<sup>n</sup> provided a selective method for differentiating isobaric and even isomeric species.

In the figures detailed below, the fragmentation of each ion is indicated by the colored boxes on the spectra and color-matched arrows on the structures. The direction of the arrow indicates the portion of the species that retains the charge after dissociation. In some cases, two or more product ions are outlined in the same colored box; typically, these product ions differ by 22 u, and therefore represent a NL with (less a proton) or without sodium. Also, for spectra containing product ions characteristic of more than one phospholipid, stars and diamonds were used to denote the respective product ions for each precursor ion. In these spectra, product ions boxed, but not marked with a star or diamond, were common to both precursor ions.

### **Unsaturated phosphatidylcholines**

One of the most abundant phospholipids observed by MALDI MS of spinal cord is PC(16:0/18:1) detected as the [M+Na]<sup>+</sup> ion at *m/z* 782. As *m/z* 782 exhibited an appreciable negative loadings coefficient on principal component 1, MS<sup>n</sup> was performed to confirm the identity of this ion (Figure 4-3). MS<sup>2</sup> of *m/z* 782 produced NLs of 59 u (*m/z* 723) and 183 u (*m/z* 599), which are characteristic NLs corresponding to alkali

metal adducts of PCs. As evident in the MS<sup>2</sup> image mapping the product ion at  $m/z$  723, this ion is localized on the control side of the tissue.

To confirm the fatty acid assignments, MS<sup>3</sup> of  $m/z$  782→723 was performed. Although the predominant product ions corresponded to NLs of cyclophosphane ( $m/z$  599) and sodiated cyclophosphane ( $m/z$  577) from the remaining portion of the PC headgroup, a NL of the *sn*-1 substituent ( $m/z$  467) was also observed. In MS<sup>4</sup>, product ions related to both fatty acid substituents are observed; the product ions at  $m/z$  305 and 279 corresponded to the [*sn*-2+Na]<sup>+</sup> and [*sn*-1+Na]<sup>+</sup> ions, respectively. Although the MS image quality significantly declines between MS<sup>3</sup> and MS<sup>4</sup> due to the loss in ion signal, the characteristic ion at  $m/z$  305 does appear to be higher in intensity on the control side of the sample. The MS<sup>4</sup> product ions at  $m/z$  543 (NL of 56 u) and 568 (NL of 18 u) most likely correspond to the NLs of C<sub>3</sub>H<sub>4</sub>O and water, respectively. These fragment ions are commonly observed in the MS<sup>4</sup> analysis of both unmodified phosphatidylcholines. Furthermore, the fragmentation pathways yielding these ions were generally uninformative regarding fatty acid and headgroup assignment; thus, the fragmentation pathways leading to these product ions were not indicated in Figure 4-3.

In addition to  $m/z$  782, the ion at  $m/z$  810, proposed to be PC(18:0/18:1), was also interrogated by MS<sup>n</sup>. MS<sup>2</sup> and MS<sup>3</sup> spectra not only exhibited product ions corresponding to the 18:0 and 18:1 fatty acid substituents, but also product ions suggesting the presence of 16:0, 20:1, and 20:4 substituents. The product ions related to each of these PC species were mapped in tissue and were similarly localized on the control side of the tissue.

## Long-chain oxidation products

One of the ions exhibiting a positive loadings coefficient on principal component 1 was  $m/z$  814, which is 32 u higher than  $m/z$  782; thus this ion was targeted for MS<sup>n</sup> analysis. Based on the product ions observed and their spatial distributions, two potential phospholipids were proposed (Figure 4-4). The product ion at  $m/z$  755, which resulted from the NL of 59 u, indicated the presence of PC. The localization of this ion on the UV-exposed side of the sample suggested that the PC-containing species was potentially an oxidation product. In addition to the product ion at  $m/z$  755, an ion resulting from the loss of phosphocholine at  $m/z$  631 (NL of 183 u) was also localized on the UV-exposed side of the tissue. The product ion boxed in red ( $m/z$  690) may result from  $\alpha$ -cleavage relative to the hydroperoxide in the *sn*-2 substituent, although this claim is not yet confirmed. Also, the unmarked product ion at  $m/z$  796 resulted from the NL of water, most likely from the hydroperoxyl group, and was localized on the UV-exposed portion of the tissue.

In contrast to the aforementioned ions, product ions related to the isobaric PE were localized in the gray matter of the control side of the tissue;  $m/z$  771 (NL of 43 u) and 673 (NL of 141 u) corresponded to NLs of the PE headgroup. A lower intensity fragment ion at  $m/z$  530 (NL of 284) was hypothesized to arise from the NL of the *sn*-1 substituent (stearic acid; 18:0). This product ion also demonstrated colocalization with the more intense PE headgroup fragments in the gray matter of the unoxidized half of the spinal cord, thereby confirming this identification as the  $[M+Na]^+$  ion of PE(18:0/22:6).

To confirm the identification and spatial localization of the PC species at  $m/z$  814, the most abundant MS<sup>2</sup> product ion related to the PC,  $m/z$  755, was targeted for MS<sup>3</sup>

analysis (Figure 4-5). Upon CID, the most abundant MS<sup>3</sup> product ion ( $m/z$  631) resulted from the NL of the remaining portion of the PC headgroup (NL of 124 u; cyclophosphane). In addition to this dominant product ion, two other characteristic product ions are observed at much lower relative abundances: the first at  $m/z$  441, corresponding to the NL of the oxidatively modified *sn*-2 substituent, and the second at  $m/z$  499, corresponding to the NL of the *sn*-1 substituent. The MS<sup>3</sup> images demonstrating the localization of these three product ions on the UV-exposed side of the tissue are also displayed in Figure 4-5. Although not yet identified, the product ion at  $m/z$  291 appears to be characteristic of the 18:1 moiety containing a hydroperoxide.

To obtain further structural information, MS<sup>4</sup> was performed on the most abundant MS<sup>3</sup> product ion,  $m/z$  631 (Figure 4-6). The resulting MS<sup>4</sup> spectrum of  $m/z$  814→755→631 produced a number of different fragment ions from those observed from the unmodified PC described above ( $m/z$  782→723→599) and shown in Figure 4-3; notably, ions denoted in red are proposed to result from  $\alpha$ -cleavage relative to the hydroperoxide group with concomitant loss of water (Hock fragmentation<sup>132</sup>). Based on the observed product ions, this fragmentation pathway was responsible for the ions observed at  $m/z$  475, 489, 503, and 517, which corresponded to the C8, C9, C10, and C11 isomers, respectively, of the hydroperoxide-containing PC. In addition to these ions, product ions corresponding to the NL of the *sn*-1 moiety ( $m/z$  377) and the [M+Na]<sup>+</sup> ions of the *sn*-2 free acid ( $m/z$  337) and *sn*-2 ketene ( $m/z$  319) confirmed the assignment of the PC fatty acid substituents as 16:0 and 18:1 hydroperoxide. Other product ions in the MS<sup>4</sup> spectrum, which will be the subject of future studies, may result from gas-phase rearrangement or from other isomeric ions at  $m/z$  631.

Another potential long-chain oxidation product observed at  $m/z$  842 was discovered by PCA and targeted for  $MS^n$  identification and imaging (Figure 4-7). Similar to  $m/z$  814,  $MS^2$  product ions were indicative of at least two isobaric phospholipids that had opposite spatial distributions, one related to a PC (product ions at  $m/z$  783 and 659, corresponding to the NL of trimethylamine and phosphocholine, respectively) and the other to PE (product ions  $m/z$  799 and 560, corresponding to the NL of aziridine and an 18:1 fatty acid moiety). However, the exact structure of the PE species could not be determined from the  $MS^3$  spectrum of  $m/z$  842 $\rightarrow$ 799, so the product ions related to the PE are outlined in black without corresponding fragmentation arrows. In addition to the isobaric PE, the  $MS^2$  spectrum of  $m/z$  842 also suggests the presence of a phosphatidylserine ( $m/z$  755, corresponding to a NL of 87 u from the PS headgroup).

To determine the fatty acid composition of the proposed PC oxidation product,  $MS^3$  was performed on the most abundant  $MS^2$  product ion related to the PC ( $m/z$  783) as displayed in Figure 4-8. Structurally informative product ions corresponding to the NLs of 124 u (cyclophosphane), 284 u (the *sn*-1 moiety), and 314 u (the oxidized *sn*-2 moiety) were observed. Moreover, the  $MS^3$  images of these product ions confirm the localization of this long-chain PC oxidation product on the UV-exposed side of the tissue. For added confirmation,  $MS^4$  was conducted on the  $MS^3$  product ion at  $m/z$  659. The fragmentation of this ion, as depicted in Figure 4-9, was analogous to that reported above for  $MS^4$  of  $m/z$  814 $\rightarrow$ 755 $\rightarrow$ 631 in Figure 4-6. Again, ions related to  $\alpha$ -cleavage relative to the hydroperoxides were detected at  $m/z$  503, 517, 531, and 545 and are proposed to result from Hock fragmentation. Additionally, the product ion resulting from the NL of the *sn*-1 moiety ( $m/z$  375) and ions corresponding to the  $[M+Na]^+$  ions of the

oxidized *sn*-2 free fatty acid ( $m/z$  337) and ketene ( $m/z$  319) were observed. As was mentioned above for the MS<sup>4</sup> spectrum from  $m/z$  814→755→631, numerous additional product ions were observed in the MS<sup>4</sup> spectrum of  $m/z$  842→783→659; the identity of these ions will be the subject of future experiments.

### Short-chain oxidation products

In addition to the long-chain oxidation products formed by the addition of oxygen(s) to the unsaturated phospholipids, several potential short-chain oxidation products (e.g.,  $m/z$  688 and 716) were discovered by PCA (Figure 4-2). These ions, which loaded positively on principal component 1 and were observed at lower  $m/z$  values than typical phospholipids, were subjected to MS<sup>n</sup> for identification. MS<sup>2</sup> of  $m/z$  688, proposed to be the [M+Na]<sup>+</sup> ion of the PC oxidation product 1-palmitoyl-2-azelaoyl-*sn*-glycero-3-phosphocholine (PAZPC), resulted in product ions indicative of an ion containing a PC headgroup (Figure 4-10); NLs of 59 u ( $m/z$  629) and 183 u ( $m/z$  505) were observed. As expected, the MS<sup>2</sup> image of  $m/z$  688→629 demonstrated localization of this ion on the UV-exposed portion of the tissue.

Furthermore, the MS<sup>3</sup> spectrum of  $m/z$  688→629 (Figure 4-11) contained product ions at  $m/z$  505 (NL of cyclophosphane; 124 u) and 249 (NL of the *sn*-1 moiety and cyclophosphane; 380 u). To obtain structural information related to the *sn*-2 moiety, MS<sup>4</sup> was performed on  $m/z$  688→629→505 as presented in Figure 4-12. The product ion at  $m/z$  211 corresponded to the [M+Na]<sup>+</sup> of the oxidized *sn*-2 substituent, thus confirming that  $m/z$  688 contained a 9:0 COOH moiety in addition to the 16:0 *sn*-1 fatty acid, which was also confirmed by the MS<sup>4</sup> product ions at  $m/z$  249 (NL of the *sn*-1 fatty acid; 256 u) and 227 (NL of the *sn*-1 fatty acid and sodium; 278 u). Figure 4-12 also illustrates the

potential of MS<sup>3</sup> imaging for enhanced selectivity, which is often required for identification of individual molecular species in complex samples such as tissue.

Another potential short-chain oxidation product that was discovered using PCA was *m/z* 716, an ion expected to correspond to two isobaric OxPCs based on the work presented in Chapter 2. The MS<sup>2</sup> spectrum of *m/z* 716, along with the proposed structures and fragmentation of these ions, are shown in Figure 4-13. As expected, the primary MS<sup>2</sup> product ions resulted from the NLs of trimethylamine (NL of 59 u) and phosphocholine (NL of 183 u). As these two species both contained a PC headgroup, these oxidation products were not differentiated by MS<sup>2</sup>; however, by performing multiple stages of mass analysis, product ions specific to each of these isomeric ions were observed.

Figures 4-14 and 4-15 demonstrated the MS<sup>3</sup> and MS<sup>4</sup> characterization of these isomers. Product ions specific to PC(16:0/11:0 COOH) and PC(18:0/9:0 COOH) are denoted by stars and diamonds, respectively; product ions common to both of these oxidized PCs are unmarked. In addition to product ions corresponding to the NL of cyclophosphane, MS<sup>3</sup> of *m/z* 716→657, yielded product ions at *m/z* 373 and 469 resulting from the NLs of the *sn*-1 and *sn*-2 substituents of PC(18:0/9:0 OOH) and product ions at *m/z* 401 and 441 corresponding to the analogous losses from PC(16:0/11:0 COOH). Also observed in the MS<sup>3</sup> spectrum were two product ions at *m/z* 249 and 277, which corresponded to the concomitant loss of the *sn*-1 moiety and cyclophosphane from PC(18:0/9:0 COOH) and PC(16:0/11:0 COOH), respectively. Thus, MS<sup>3</sup> provides significant evidence that *m/z* 716 corresponds to both of these oxidation products. Although potentially unnecessary for the identification of these ions

at  $m/z$  716, as fatty acid composition was determined in  $MS^3$ ,  $MS^4$  was performed on  $m/z$  716→657→533 for thoroughness. The  $MS^4$  product ions support the identification of these two isobaric oxidized PCs at  $m/z$  716, as product ions related to both of the fatty acid substituents for both of these products ( $m/z$  171, 193, 199, 211, 221, 227, 239, 249, 255, and 277) were assigned (Figure 4-15).

### **Conclusions**

This work demonstrates, for the first time, that PCA is a powerful tool for rapidly discovering potential biomarkers of oxidative stress in MALDI-MSI datasets and that  $MS^n$  provides a selective method for identifying and localizing these oxidation products in situ. The  $MS^n$  fragmentation pathways for several representative oxidation products, including long-chain and short-chain products of PCs were presented. Thus, this work provides the foundation for future studies that will investigate these and other oxidation products as potential biomarkers of disease or oxidative stress. Furthermore, the utility of  $MS^n$  imaging for differentiating isobaric and even isomeric molecular species was illustrated. Through this work the potential of MALDI  $MS^n$  for identifying individual molecular species, such as oxidized phospholipids, and localizing these individual species in situ, was realized.

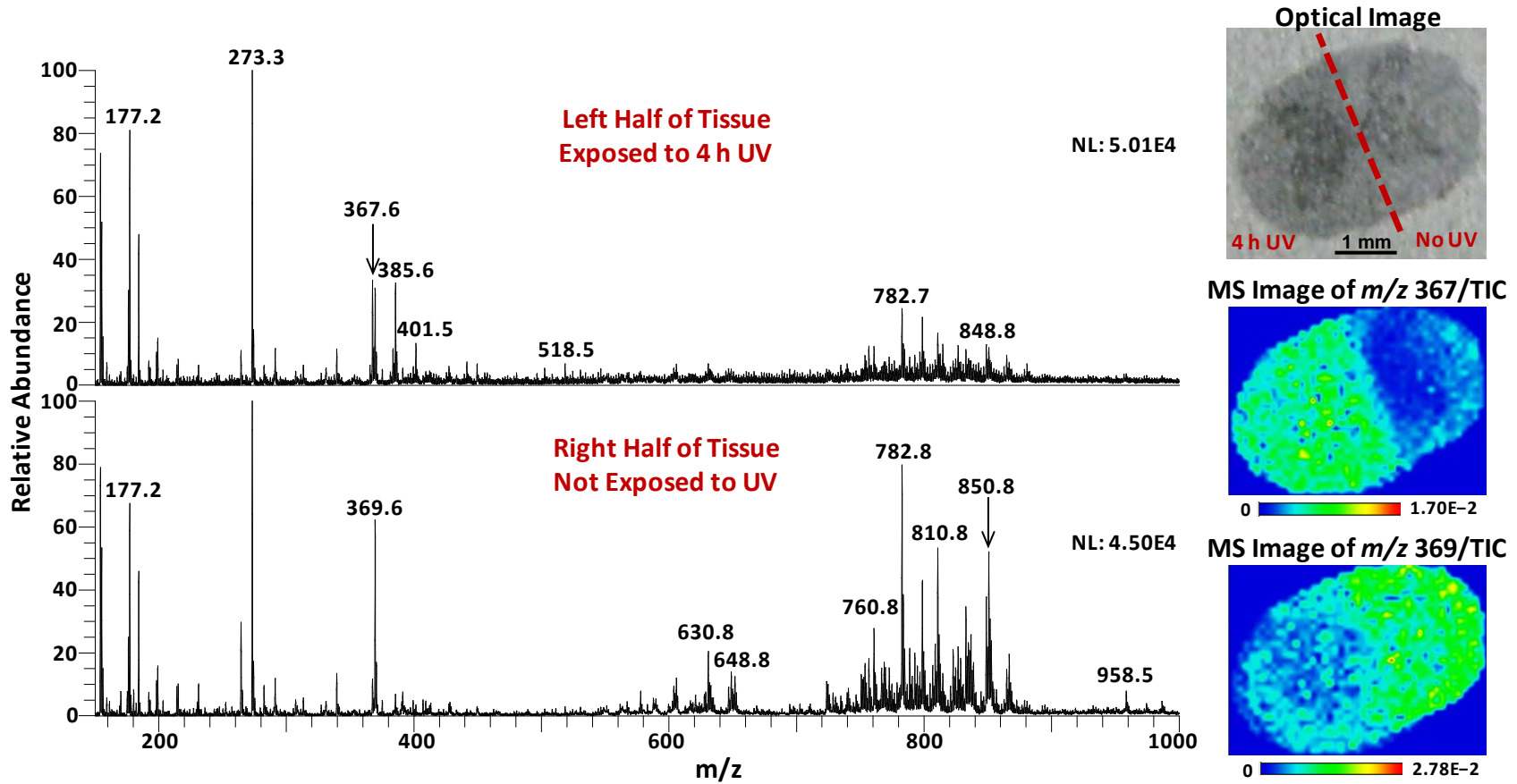


Figure 4-1. MALDI MS spectrum from the left half of the tissue, which was exposed to UV for 4 hours (top) and from the right half of the tissue, which was not exposed to UV (bottom). Each spectrum was produced by averaging 20 analytical scans. On the right, an optical image of tissue and MS images of an oxidation product of cholesterol ( $[\text{oxysterol}+\text{H}-2\text{H}_2\text{O}]^+$  at  $m/z$  367 normalized to the TIC; top) and cholesterol ( $[\text{chol}+\text{H}-\text{H}_2\text{O}]^+$  at  $m/z$  369 normalized to the TIC; bottom) are displayed.

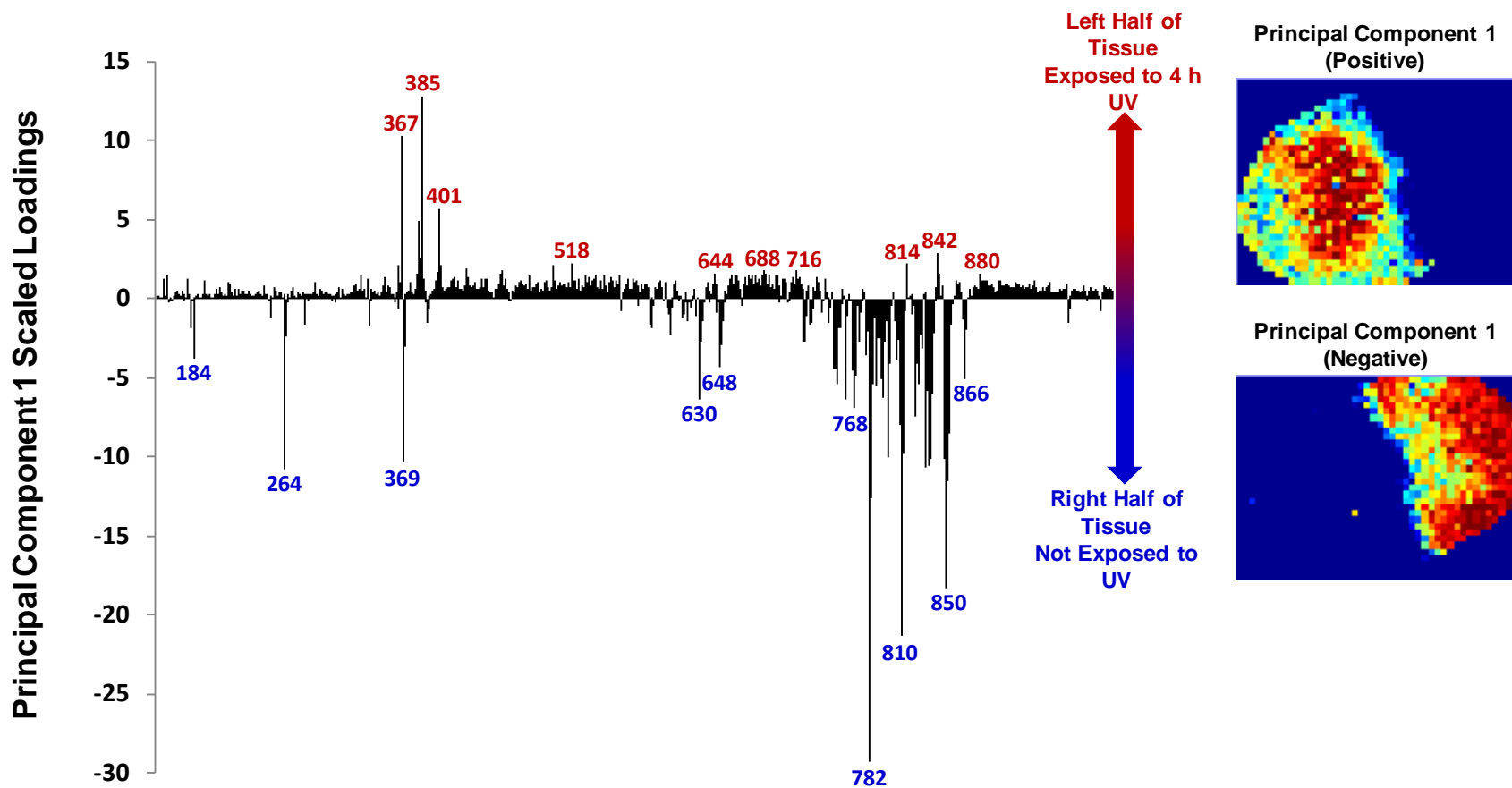


Figure 4-2. Principal component 1 scaled loadings plot (left) and scores images (right) from the MSI data set in Figure 4-1. Principal component 1 dictates separation of the oxidized (positive) and unoxidized (negative) sides of the spinal cord. Various  $m/z$  values with positive loadings on principal component 1, such as  $m/z$  814 and 716, were targeted for  $MS^n$  studies. The loadings were scaled by the standard deviation for each variable.

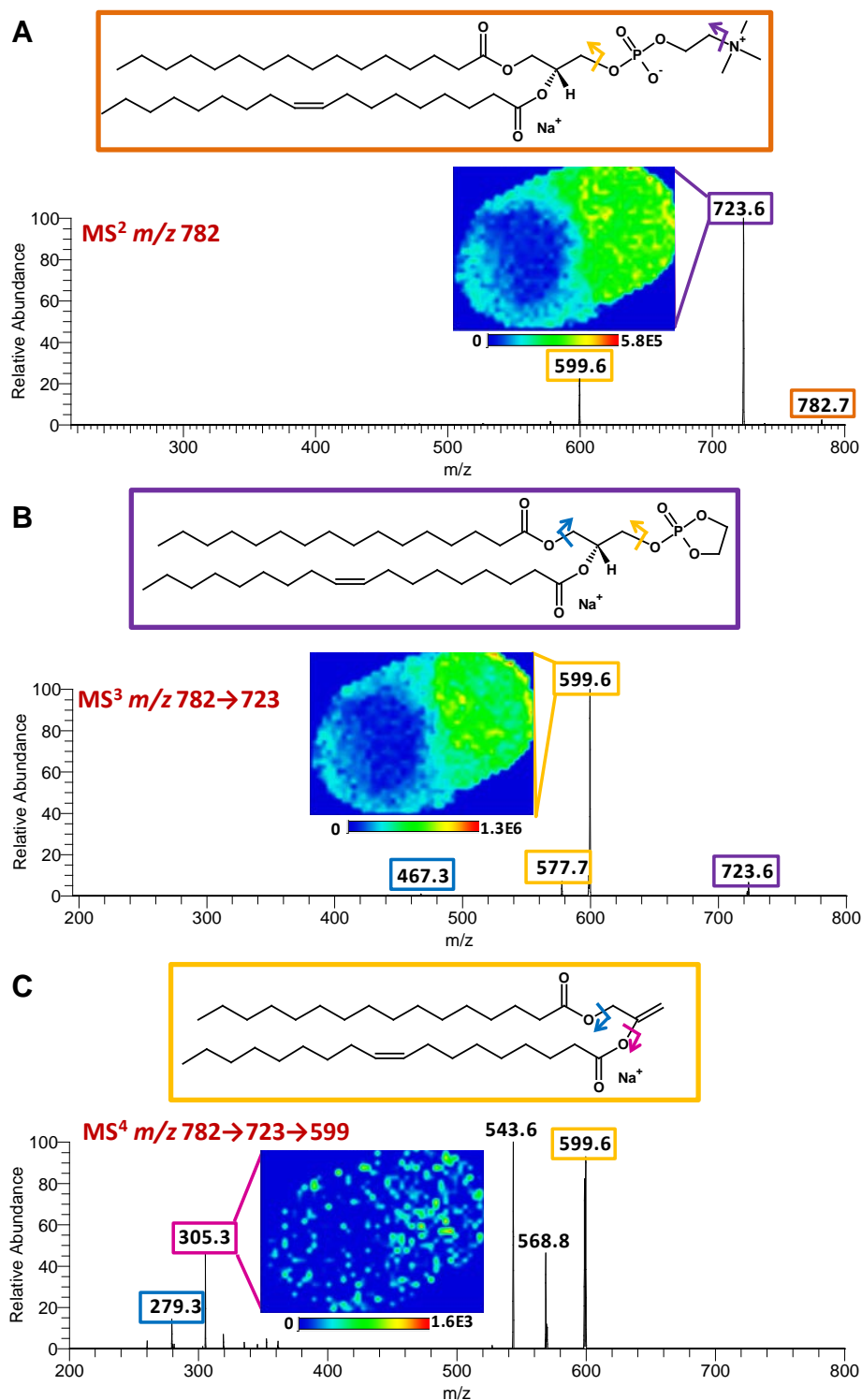


Figure 4-3. MS<sup>n</sup> of PC(16:0/18:1), an abundant unsaturated phospholipid in spinal cord tissue. A) MS<sup>2</sup> of *m/z* 782 ([PC(16:0/18:1)+Na]<sup>+</sup>) and MS image of the product ion at *m/z* 723. B) MS<sup>3</sup> of *m/z* 723 ([PC(16:0/18:1)+Na-N(CH<sub>3</sub>)<sub>3</sub>]<sup>+</sup>) and MS image of the product ion at *m/z* 599. C) MS<sup>4</sup> of *m/z* 599, ([PC(16:0/18:1)+Na-HPO<sub>4</sub>(CH<sub>2</sub>)<sub>2</sub>N(CH<sub>3</sub>)<sub>3</sub>]<sup>+</sup>) and MS image of the product ion at *m/z* 305.

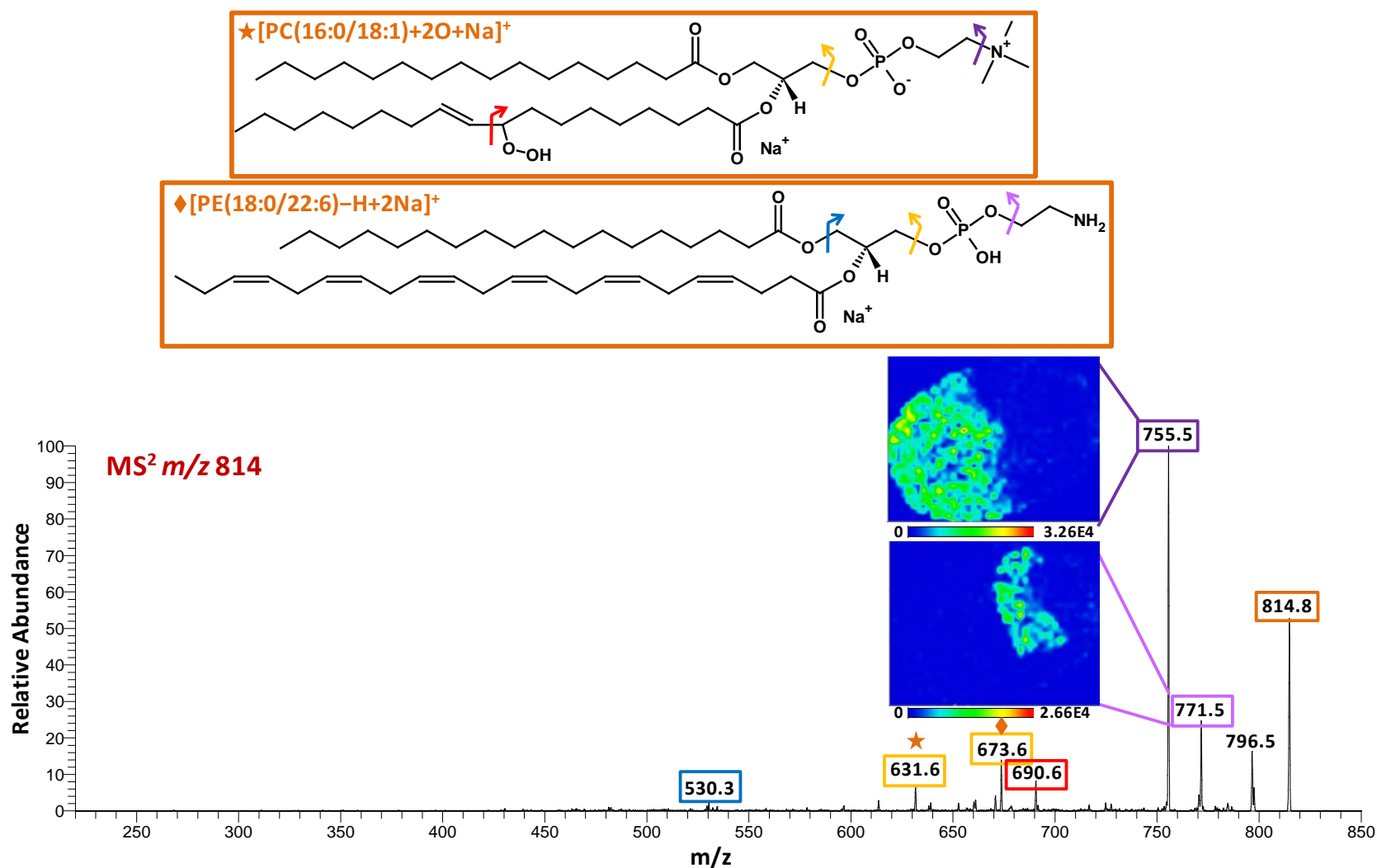


Figure 4-4. MS<sup>2</sup> product ion spectrum of *m/z* 814, a proposed long-chain oxidation product of phosphatidylcholine. Based on the observed fragmentation, two different phospholipids with opposite localization were present at *m/z* 814: one containing a PC headgroup and one containing a PE headgroup. The proposed structures and fragmentation pathways of these two phospholipids are shown. Additionally, MS<sup>2</sup> images of the characteristic product ions of the PC at *m/z* 755 (NL of 59 u) and the PE at *m/z* 771 (NL of 43 u) are depicted.

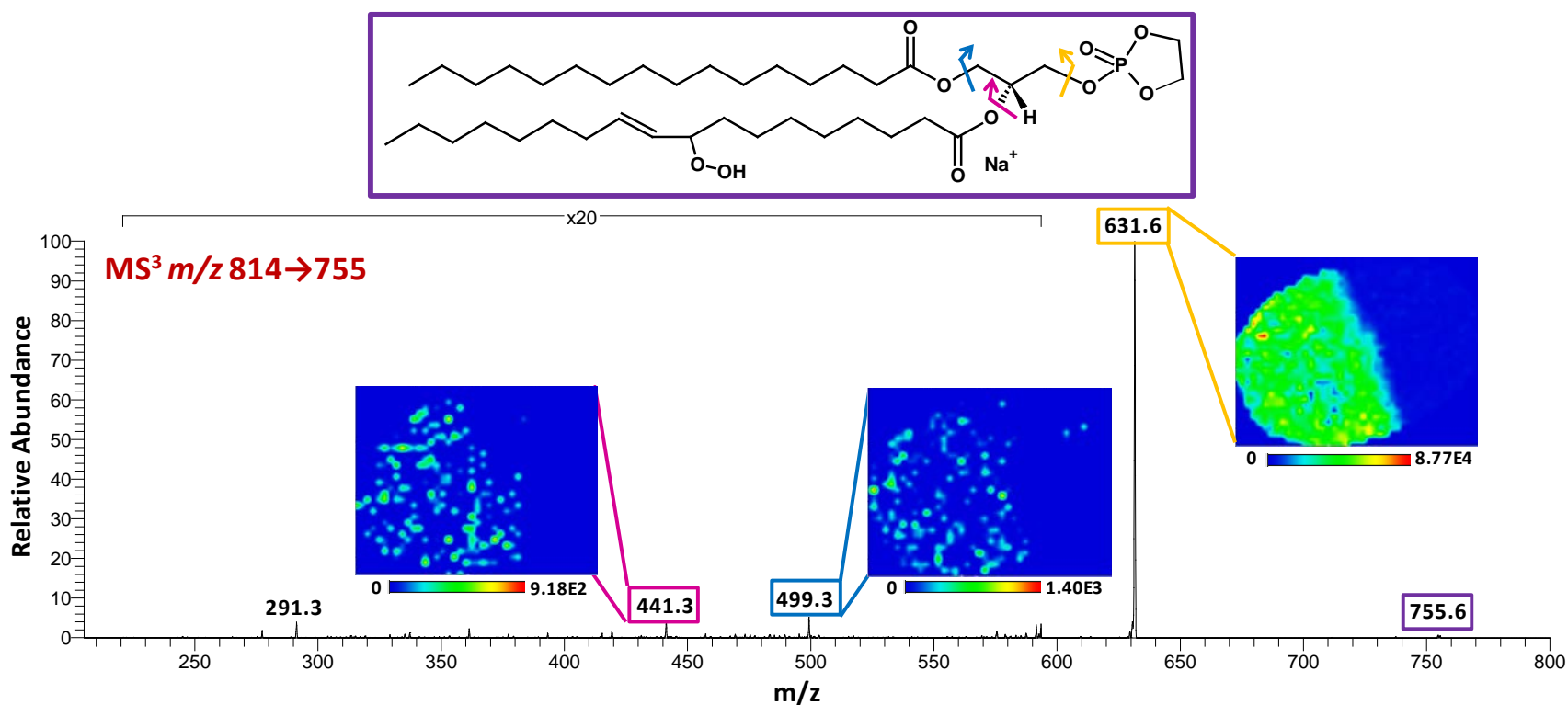


Figure 4-5. MS<sup>3</sup> product ion spectrum of  $m/z$  814→755. Images were generated by mapping the intensity of the product ions corresponding to the NLs of cyclophosphane (124 u), *sn*-1 moiety (256 u), and *sn*-2 moiety (314 u). The MS<sup>3</sup> images illustrate the localization of the proposed PC oxidation product on the UV-exposed side of the tissue.

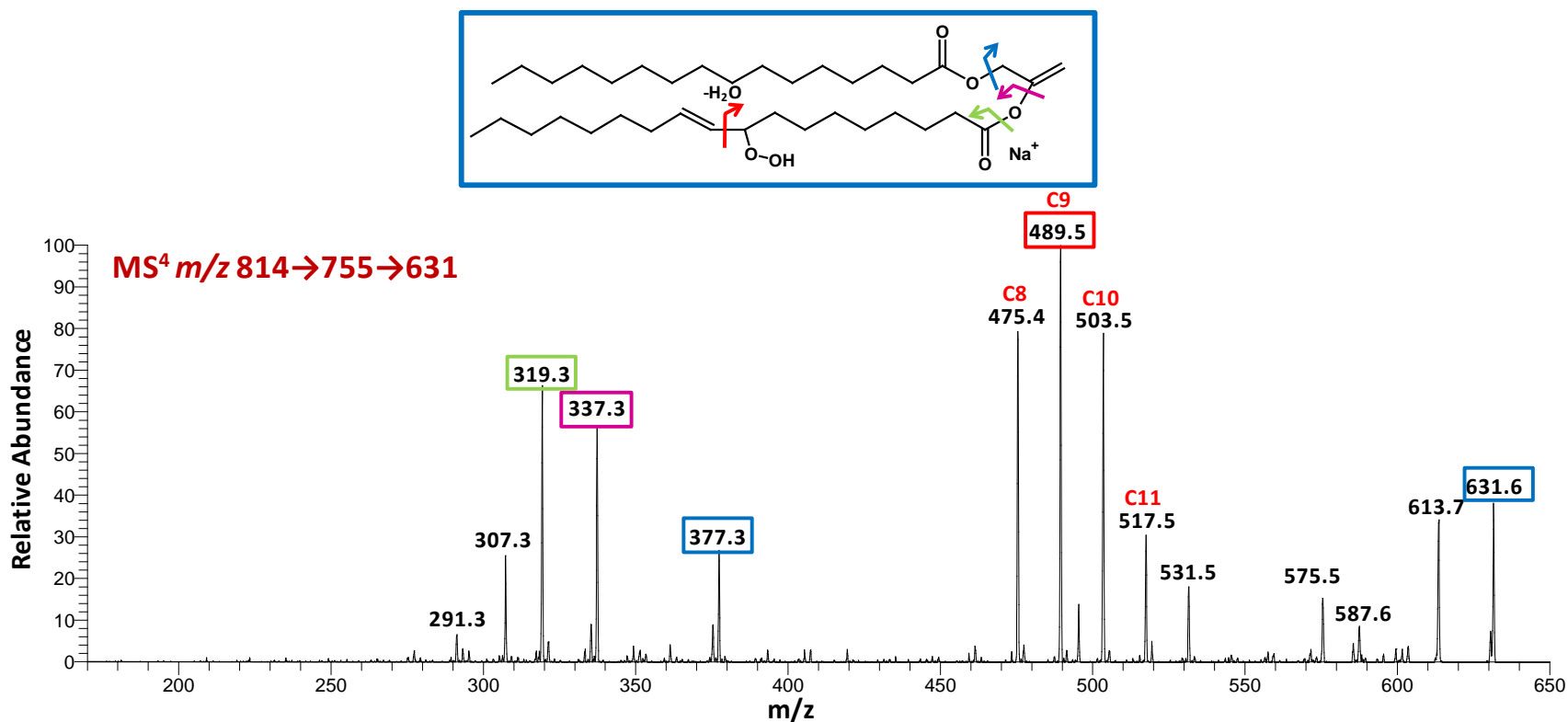


Figure 4-6. MS<sup>4</sup> product ion spectrum of  $m/z$  814→755→631. Product ions corresponding to the NLs of the *sn*-1 and oxidized *sn*-2 fatty acid substituents confirm the addition of two oxygens to the *sn*-2 moiety. Although the exact location of oxidative modification has not been confirmed, product ions indicated in red are proposed to correspond to α-cleavages relative to the hydroperoxide; thus, several isomers are probable.

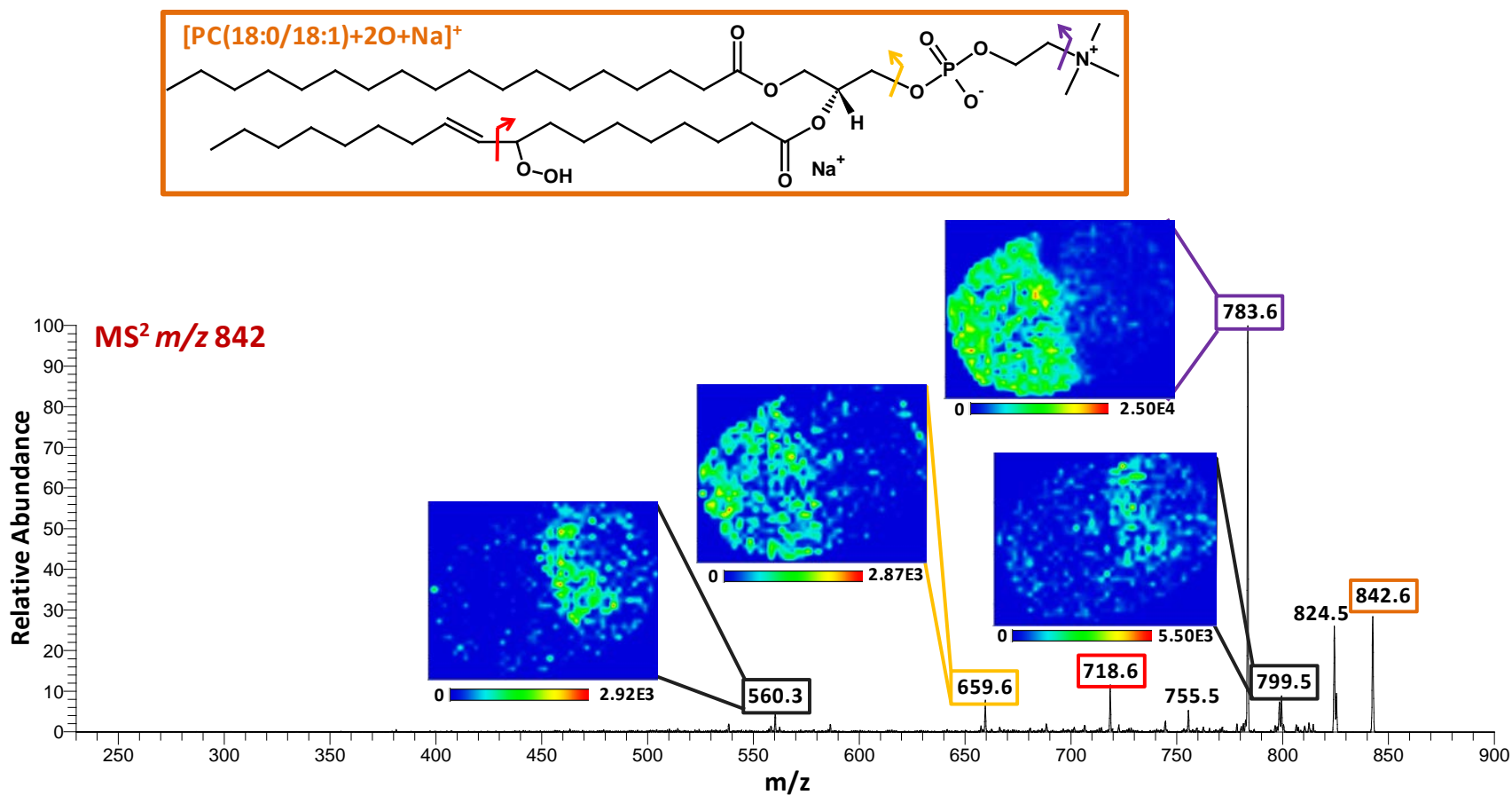


Figure 4-7. MS<sup>2</sup> product ion spectrum of *m/z* 842, a proposed long-chain oxidation product of phosphatidylcholine. Based on the observed fragmentation and MS<sup>2</sup> images, two different phospholipids with opposite localization were present at *m/z* 842, one containing a PC headgroup and the other containing a PE headgroup. The proposed structure and fragmentation pathways of the long-chain PC oxidation product are shown.

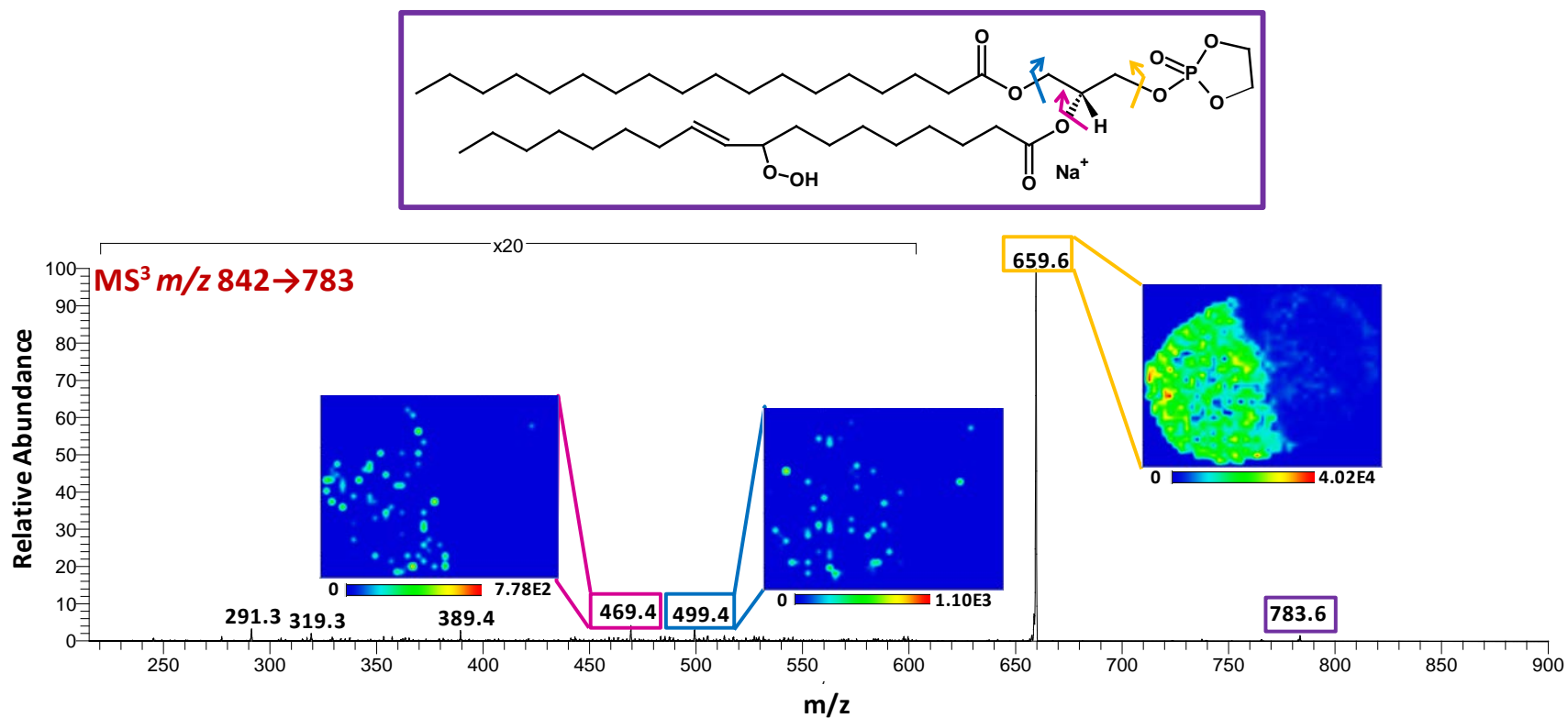


Figure 4-8. MS<sup>3</sup> product ion spectrum of  $m/z$  842→783. MS images were generated by mapping the intensity of the product ions corresponding to the NLs of cyclophosphane (124 u), *sn*-1 moiety (284 u), and *sn*-2 moiety (314 u). The MS<sup>3</sup> images illustrate the localization of the proposed PC oxidation product on the UV-exposed side of the tissue

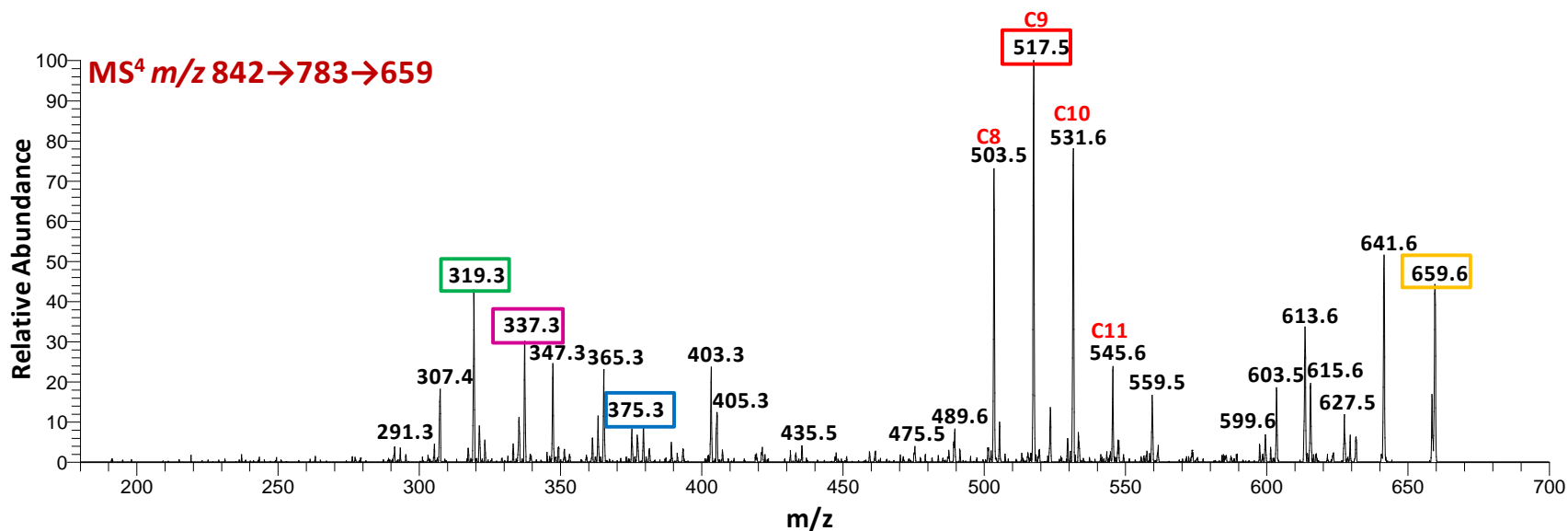
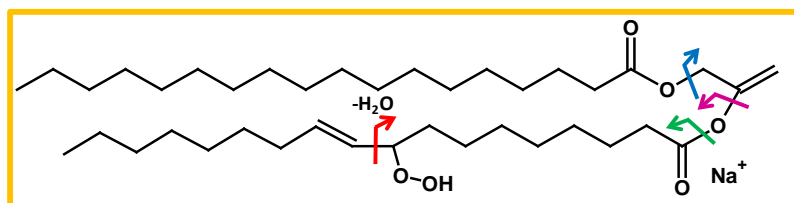


Figure 4-9. MS<sup>4</sup> product ion spectrum of  $m/z$  842→783→659. Product ions corresponding to the NLs of the *sn*-1 and oxidized *sn*-2 fatty acid substituents confirm the addition of two oxygens to the *sn*-2 moiety. Although the exact location of oxidative modification has not been confirmed, product ions indicated in red are proposed to correspond to  $\alpha$ -cleavages relative to the hydroperoxide; thus, several isomers are probable.

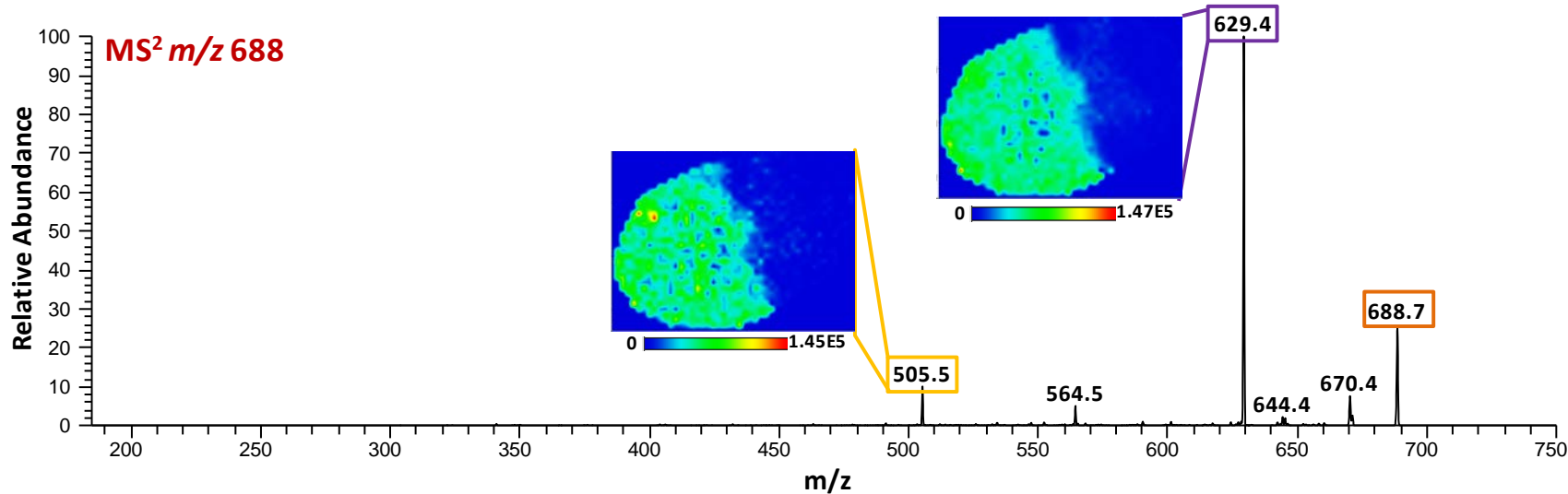
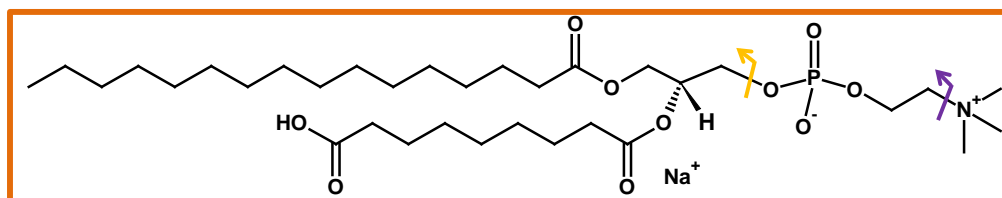


Figure 4-10. MS<sup>2</sup> product ion spectrum of *m/z* 688, a proposed short-chain oxidation product of phosphatidylcholine. The MS<sup>2</sup> images demonstrate localization on the UV-exposed side of the tissue, and the observed product ions confirm the presence of a phosphocholine headgroup. However, product ions related to the fatty acid substituents are not observed; therefore, further stages of mass analysis were performed.

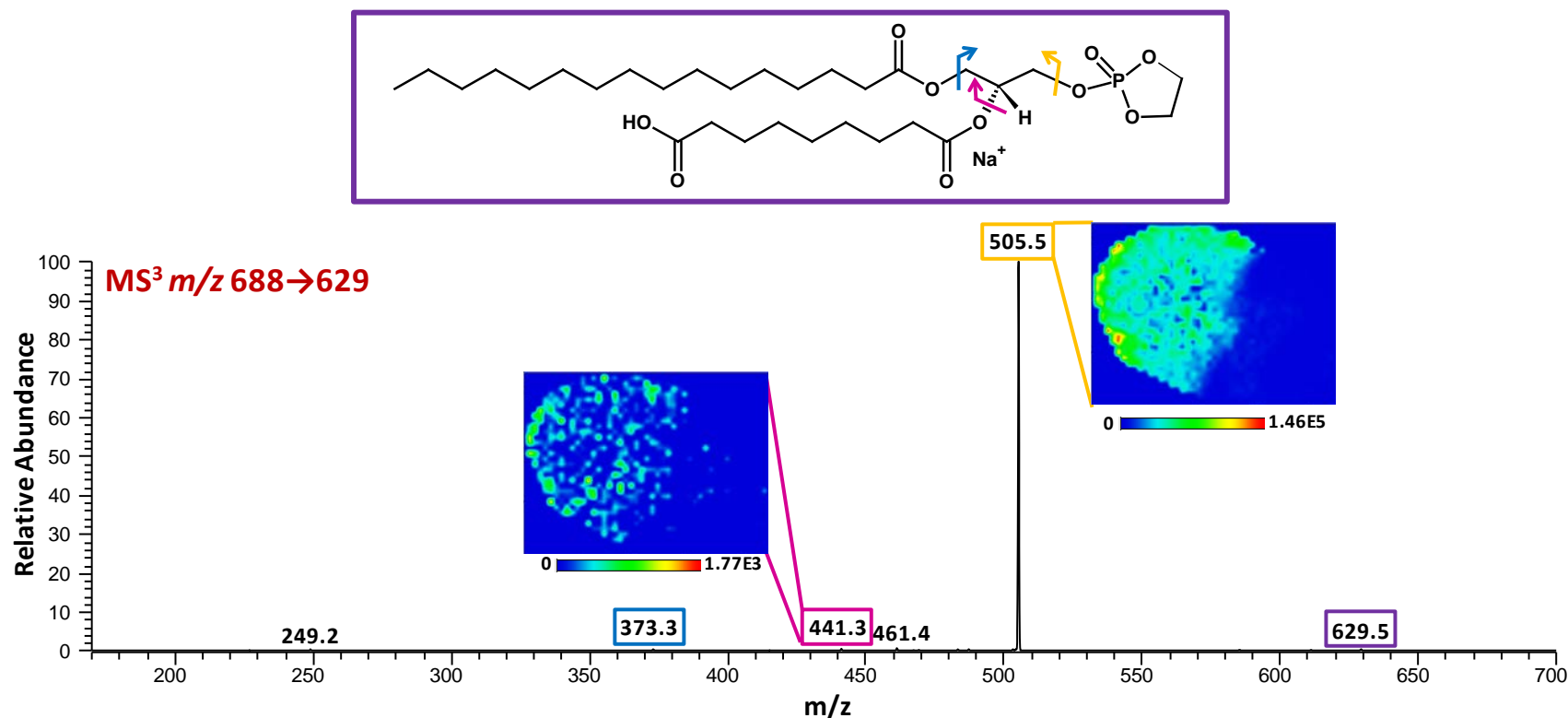


Figure 4-11. MS<sup>3</sup> product ion spectrum of  $m/z$  688→629. Based on the observed product ions, identified as indicated by the color-matched boxes and arrows, this ion contained a 16:0 fatty acid substituent and a 9:0 COOH fatty acid substituent, confirming the identity of the ion at  $m/z$  688. Furthermore, the MS<sup>3</sup> images illustrate the localization of this oxidation product on the UV-exposed side of the tissue.

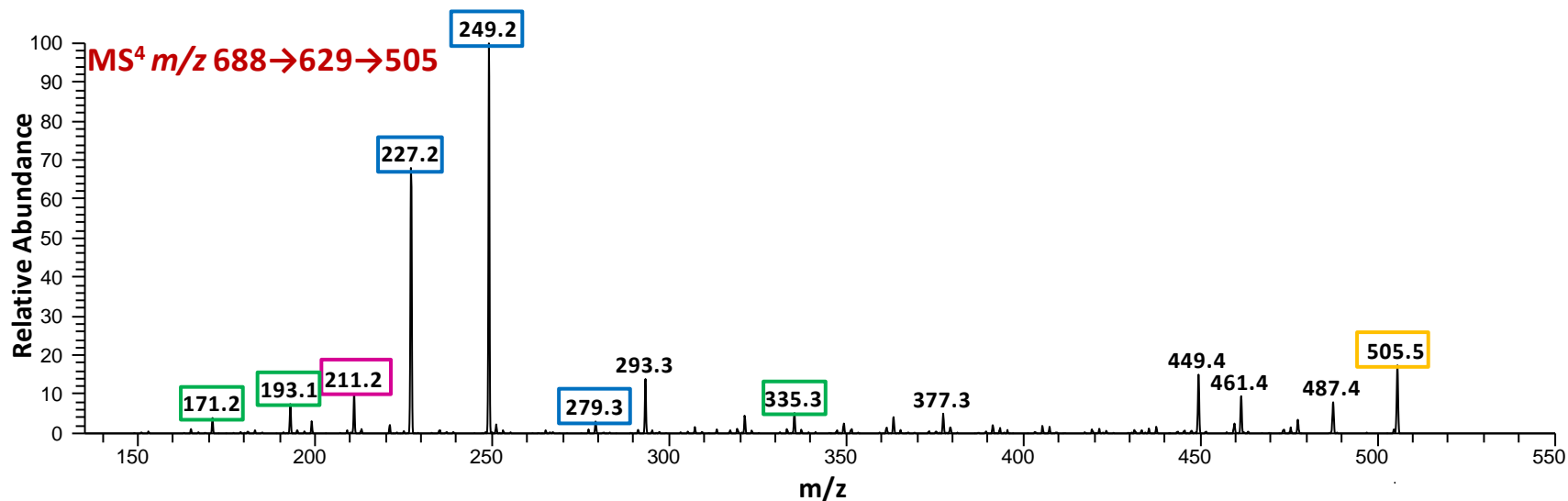
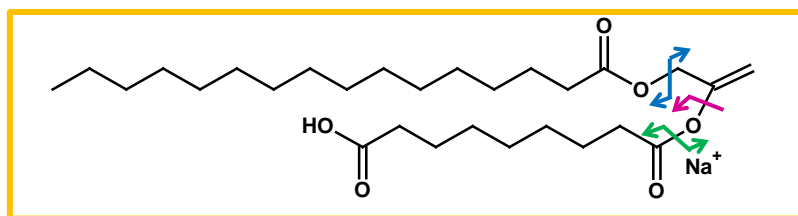


Figure 4-12. MS<sup>4</sup> product ion spectrum of  $m/z$  688→629→505. The observed product ions further substantiate the identification of this PC oxidation product, as multiple ions related to each of the fatty acid substituents were observed as indicated by the color-matched boxes and arrows.

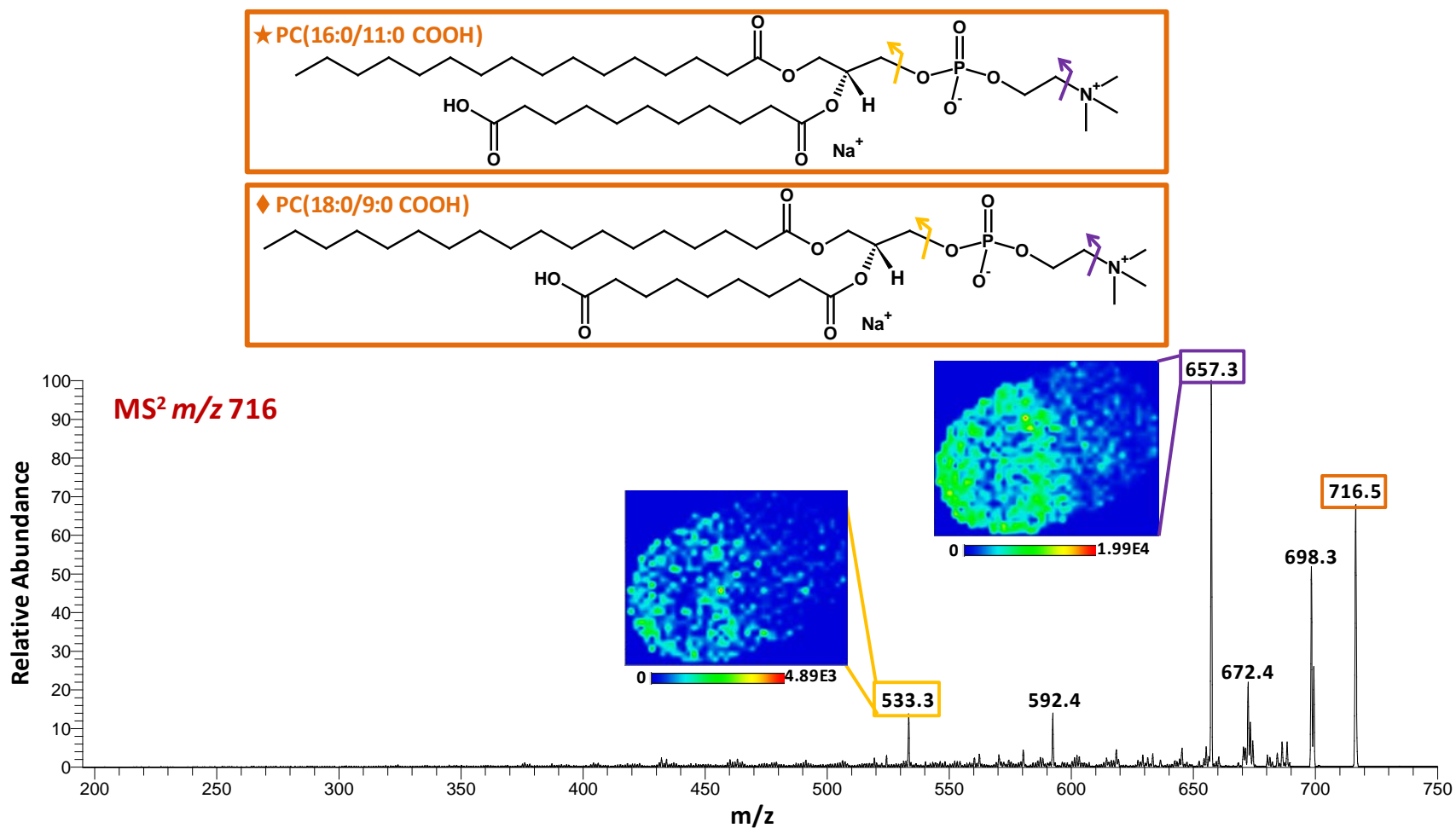


Figure 4-13. MS<sup>2</sup> product ion spectrum of  $m/z$  716. Two possible isomeric short-chain oxidation products of phosphatidylcholine occur at  $m/z$  716. The MS<sup>2</sup> images demonstrate localization on the UV-exposed side of the tissue, and the observed product ions confirm the presence of a phosphocholine headgroup. However, product ions related to the fatty acid substituents are not observed; therefore, further stages of mass analysis were performed.

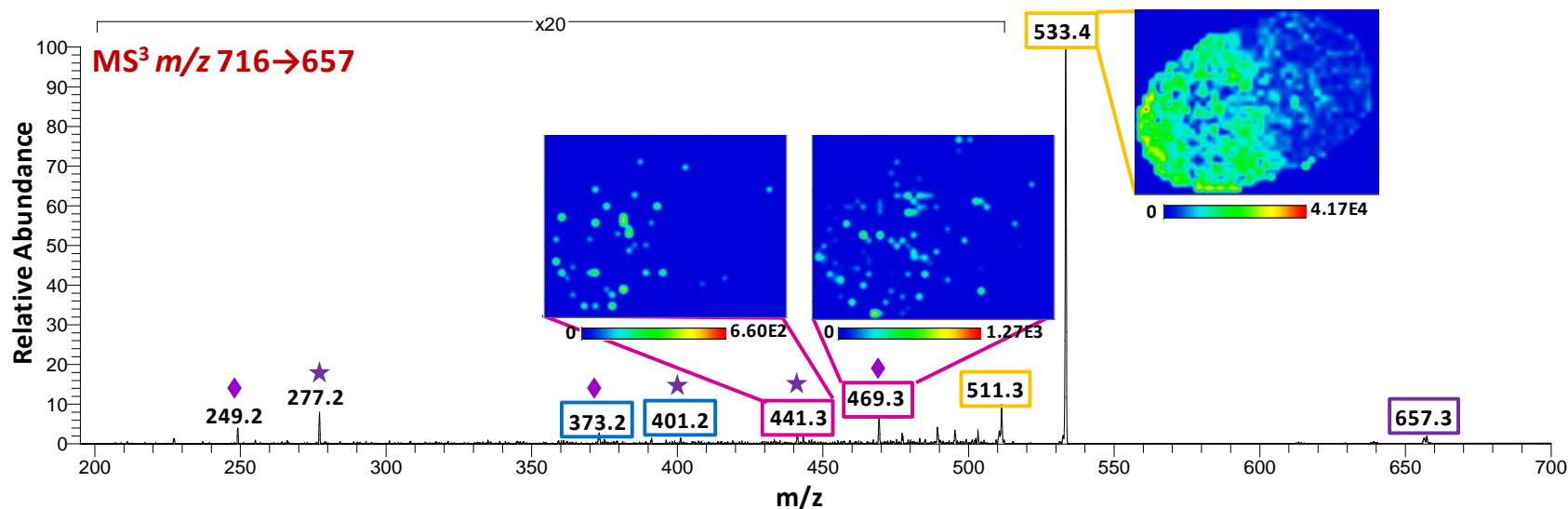
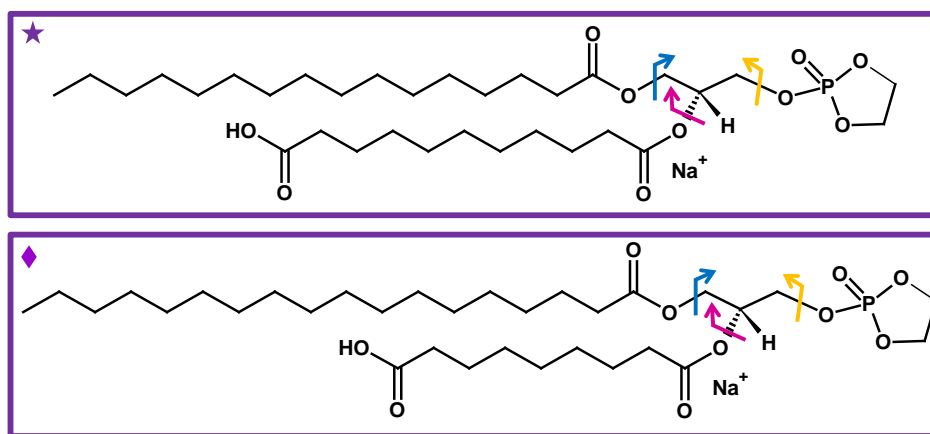


Figure 4-14. MS<sup>3</sup> product ion spectrum of  $m/z$  716→657. Product ions related to PC(16:0/11:0 COOH) and PC(18:0/9:0 COOH) are marked with stars and diamonds, respectively. Based on these observed product ions, the fatty acid composition of the two isomeric PCs was confirmed; the product ions at  $m/z$  401 and 441 corresponded to the NL of 16:0 and 11:0 COOH, respectively, whereas the product ions at  $m/z$  373 and 469 corresponded to the NL of 18:0 and 9:0 COOH, respectively. Furthermore, the MS<sup>3</sup> images illustrate the localization of both of these oxidation products on the UV-exposed side of the tissue.

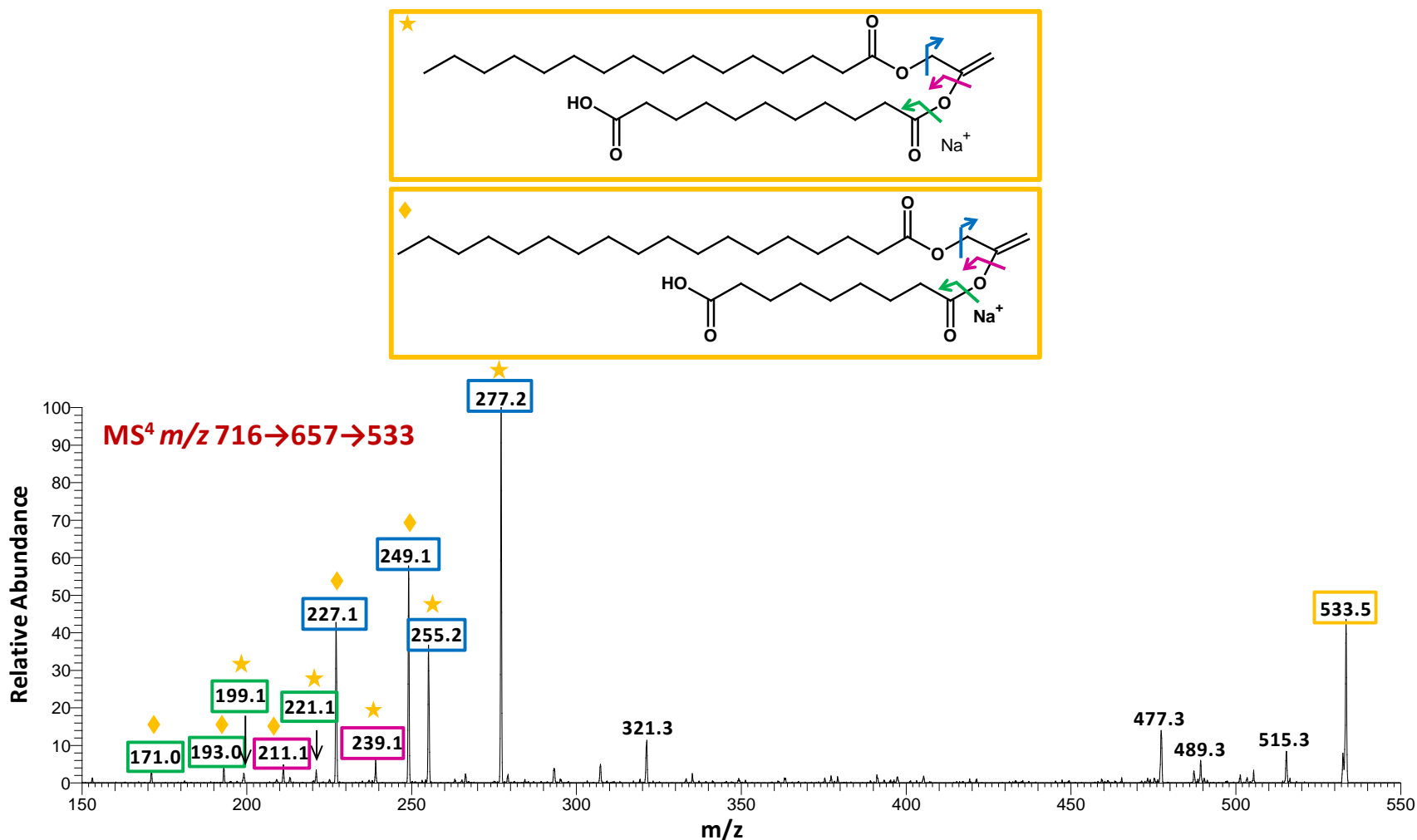


Figure 4-15. MS<sup>4</sup> product ion spectrum of  $m/z$  716→657→533. Based on the observed fragmentation, the presence of two isomeric oxidized PCs, PC(16:0/11:0 COOH) and PC(18:0/9:0 COOH), was confirmed. Analogous product ions related to PC(16:0/11:0 COOH) and PC(18:0/9:0 COOH) are indicated by the color-matched boxes and arrows; the product ions of PC(16:0/11:0 COOH) and PC(18:0/9:0 COOH) are marked with stars and diamonds, respectively.

## CHAPTER 5 CONCLUSIONS AND FUTURE WORK

### Conclusions

To gain a comprehensive understanding of the role of oxidized phospholipids (OxPLs) in disease, methods for detecting individual OxPLs in biological and clinical samples must first be developed. In this work, matrix-assisted laser desorption/ionization (MALDI) tandem mass spectrometry ( $MS^n$ ) techniques for characterizing, identifying, and imaging phospholipid oxidation products are described. The  $MS^n$  capabilities of the linear ion trap (LIT) were exploited for selective detection of individual phosphatidylcholine oxidation products (OxPCs) and phosphatidylethanolamine oxidation products (OxPEs). Up to four stages of mass analysis were used to obtain enhanced structural information and, hence, improve confidence in ion identification.

First, five different short-chain OxPC standards were characterized by MALDI  $MS^n$ . Ions of both  $[M+H]^+$  and  $[M+Na]^+$  for each of the OxPCs were interrogated. Although several product ions corresponding to the fatty acid substituent were observed following CID of the  $[M+H]^+$  ions, the  $[M+Na]^+$  ions yielded more structurally informative product ions that were targeted for further stages of mass analysis.  $MS^3$  of the  $[M+Na-N(CH_3)_3]^+$  ions yielded fragmentation indicative of the OxPC modification; specifically, a product ion corresponding to the neutral loss of  $CO_2$  (NL of 44) was observed for OxPCs containing a terminal carboxylic acid rather than an aldehyde.

Furthermore,  $MS^4$  of the  $[M+Na-HPO_4(CH_2)_2N(CH_3)_3]^+$  ions for each OxPCs resulted in fragmentation pathways dependent on the *sn*-2 fatty acid chain length and type of functional group(s). In  $MS^4$ , OxPCs with a terminal aldehyde yielded

fragmentation of the *sn*-1 fatty acid distinct from terminal carboxylic acid-containing OxPCs. Specifically, aldehyde-containing OxPCs with palmitic acid esterified to the *sn*-1 position of the glycerol backbone yielded a NL of 254 u, 2 u less than the nominal mass of palmitic acid, whereas the analogous terminal carboxylic acid-containing OxPCs demonstrated a NL of 256 u. Finally, the presence of a  $\gamma$ -ketone relative to the terminal carboxyl group resulted in C–C bond cleavages along the *sn*-2 substituent, providing diagnostic MS<sup>4</sup> product ions for keto-containing OxPCs; two intramolecular retro-ene reactions were proposed to explain these observed product ions.

The applicability of this developed MALDI MS<sup>n</sup> method for identifying short-chain OxPCs in biological tissue samples was demonstrated using control rat spinal cord tissue. The utility of MS<sup>n</sup> for distinguishing individual OxPLs in complex biological samples was also illustrated as two isomeric OxPCs were discerned based on the observed MS<sup>3</sup> and MS<sup>4</sup> product ions. Furthermore, MSI performed on these tissues illustrated localization of two isomeric OxPCs in the gray matter of spinal cord tissue from the cervical region.

The above MALDI MS<sup>n</sup> techniques were also employed to identify and characterize [M+Na]<sup>+</sup> and [M-H+2Na]<sup>+</sup> ions of short-chain PE oxidation products formed by autoxidation of various unsaturated PE standards. Six different OxPEs were investigated and the MS<sup>n</sup> (where n= 2, 3, or 4) fragmentation was shown to depend on the nature of the oxidative modification, as was the case for OxPCs. Specifically, OxPEs containing a terminal aldehyde at the *sn*-2 position yielded an abundant MS<sup>2</sup> product ion corresponding to the NL of water. This fragmentation pathway was proposed to result from a reaction between the primary amine of the ethanolamine head group and the

terminal carbonyl carbon of the *sn*-2 moiety, which resulted in the NL of water and the formation of a macrocyclic structure. Additionally, the relative abundance of the ion corresponding to the loss of water increased as a function of chain length of the *sn*-2 moiety containing the terminal aldehyde. Thus, the macrocyclic structure was preferentially formed during CID of PE(16:0/9:0 CHO), but was not as favorable for PE(16:0/4:0 COOH) or PE(18:0/4:0 CHO), the shorter chain aldehyde derivatives. These results correlate well with previous studies reporting the formation of macrocyclic structures in the gas phase following MS<sup>2</sup> of b<sub>n</sub> peptide ions; moreover, an analogous increase in the relative abundance of the macrocyclic structure as a function of fragment size was also reported.<sup>122</sup>

Following characterization of OxPL standards, *in vitro* oxidation was performed on spinal cord tissue to identify and image these oxidation products *in situ*. Select areas of thin tissue sections from the cervical region of control rat spinal cord were exposed to UV light and ambient air for 4 h. MSI was then performed on the tissue and principal component analysis (PCA) was used for data mining to determine *m/z* values to be targeted for MS<sup>n</sup> analysis. Several long-chain and short-chain OxPCs were discovered by PCA and identified based on characteristic MS<sup>n</sup> fragmentation. Furthermore, the MS<sup>n</sup> images illustrated localization of these OxPCs on the UV-exposed side of the tissue as expected. These studies demonstrate the potential for using PCA in combination with MALDI MS<sup>n</sup> imaging to identify and localize oxidized lipids in thin tissue sections. Thus, this work provides the foundation for future studies that will utilize MALDI MS<sup>n</sup> and MSI to gain a better understanding to OxPLs and their role in human disease.

## Future Work

Future studies will investigate the effects of in vitro oxidation on other lipid classes. Phosphatidylserine and cardiolipin have been shown to undergo extensive oxidation, which could be involved in the pathology of traumatic brain injury.<sup>13,133</sup> These oxidation products would be interesting to study by MS<sup>n</sup> as they are preferentially ionized in negative mode; thus, a more basic MALDI matrix such as 9-aminoacridine would need to be employed. MS<sup>n</sup> of oxidized cardiolipin would also likely yield extensive fragmentation as each cardiolipin has four fatty acid substituents, that are typically unsaturated;<sup>134</sup> therefore, one could potentially determine by MS<sup>n</sup> whether one or more of these fatty acids become oxidatively modified following in vitro oxidation. Lastly, cholesterol is another target of oxidation that could be studied using the MALDI MS<sup>n</sup> methods developed in this work. As presented in Chapter 4, cholesterol appears to be a primary target of oxidation in tissue exposed to UV light.

For in vitro oxidation experiments, this work primarily focused on autoxidation and UV light-induced oxidation; however, many other in vitro oxidation methods have been reported and could be utilized to investigate whether the mechanism of oxidation (e.g., free-radical vs singlet oxygen) has any effect on what oxidation products are formed. Additionally, oxidation products caused by enzymatic oxidation by either lipoxygenase or myeloperoxidase are expected to selectively oxidize unsaturated fatty acids at specific positions. All of these aforementioned in vitro methods are applicable to oxidation of phospholipid standards; however, in vitro oxidation of tissue would be more challenging from a method development standpoint. Issues involving the application of oxidant to the tissue without causing analyte migration would need to be considered.

In addition to studying oxidation of other phospholipid classes and investigating different in vitro oxidation methods, future studies will aim to identify OxPLs in biological samples from various disease models. Due to the high abundance of polyunsaturated phospholipids and exposure to UV light, the retina is an ideal model for studying in vivo lipid oxidation.<sup>35</sup> However, preliminary experiments with retina tissue from adult Rhesus monkeys suggested that better methods for preparation of retinal flat mounts must be developed before informative MS images can be obtained; thus, this work was not included in the previous chapters. Most notably, cracking of the tissue was observed which resulted in varied topography causing artifacts in the MS images.

Furthermore, brain, spinal cord, and sciatic nerve tissues from Sprague-Dawley rat models of two similar disease states, diabetic neuropathy and dichloroacetate (DCA)-induced neuropathy, hypothesized to involve oxidative damage to nervous tissue, will be studied.<sup>135,136,137</sup> Nervous tissues from healthy rats will also be analyzed as control samples for comparison. Since spatial information can be retained in MALDI, the distributions of oxidation products in various tissues will be investigated by MSI, which may lead to an improved understanding of the biological and physiopathological activities of OxPLs.

## LIST OF REFERENCES

- (1) Bochkov, V. N.; Oskolkova, O. V.; Birukov, K. G.; Levonen, A. L.; Binder, C. J.; Stockl, J. *Antioxid. Redox Signaling* **2010**, *12*, 1009-1059.
- (2) Markesbery, W. R.; Lovell, M. A. *Neurobiol. Aging* **1998**, *19*, 33-36.
- (3) Koppaka, V.; Axelsen, P. H. *Biochemistry* **2000**, *39*, 10011-10016.
- (4) Koppaka, V.; Paul, C.; Murray, I. V. J.; Axelsen, P. H. *J. Biol. Chem.* **2003**, *278*, 36277-36284.
- (5) Huang, L.; Estrada, R.; Yappert, M. C.; Borchman, D. *Free Radical Biol. Med.* **2006**, *41*, 1425-1432.
- (6) Berliner, J. A.; Leitinger, N.; Tsimikas, S. *J. Lipid Res.* **2009**, *50*, S207-S212.
- (7) Qin, J.; Goswami, R.; Balabanov, R.; Dawson, G. *J. Neurosci. Res.* **2007**, *85*, 977-984.
- (8) Baskol, G.; Demir, H.; Baskol, M.; Kilic, E.; Ates, F.; Karakukcu, C.; Ustidal, M. *Cell Biochem. Funct.* **2006**, *24*, 307-311.
- (9) Adibhatla, R. M.; Hatcher, J. F. *Antioxid. Redox Signaling* **2010**, *12*, 125-169.
- (10) Yamashita, M.; Fenn, J. B. *J. Phys. Chem.* **1984**, *88*, 4451-4459.
- (11) Tanaka, K.; Waki, H.; Ido, Y.; Akita, S.; Yoshida, Y.; Yoshida, T.; Matsuo, T. *Rapid Commun. Mass Spectrom.* **1988**, *2*, 151-153.
- (12) Karas, M.; Hillenkamp, F. *Anal. Chem.* **1988**, *60*, 2299-2301.
- (13) Sparvero, L. J.; Amoscato, A. A.; Kochanek, P. M.; Pitt, B. R.; Kagan, V. E.; Bayir, H. *J. Neurochem.* **2010**, *115*, 1322-1336.
- (14) Domingues, M. R. M.; Reis, A.; Domingues, P. *Chem. Phys. Lipids* **2008**, *156*, 1-12.
- (15) O'Donnell, V. B. *Biochim. Biophys. Acta, Mol. Cell Biol. Lipids* **2011**, *1811*, 818-826.
- (16) Fuchs, B.; Bresler, K.; Schiller, J. *Chem. Phys. Lipids* **2011**, *164*, 782-795.
- (17) Watson, A. D. *J. Lipid Res.* **2006**, *47*, 2101-2111.
- (18) Alberts, B.; Johnson, A.; Lewis, J.; Raff, M.; Roberts, K.; Walter, P. *Molecular Biology of the Cell*, 4 ed.; Garland Science: New York, 2002.

- (19) Berg, J. M.; Tymoczko, J. L.; Stryer, L. *Biochemistry*, 5th ed.; W H Freeman: New York, 2002.
- (20) Lehninger, A. L.; Nelson, D. D. L.; Cox, M. M. *Lehninger Principles of Biochemistry*, 4th ed.; W.H. Freeman: New York, 2005.
- (21) Vance, J. E.; Vance, D. E. *Biochemistry of Lipids, Lipoproteins and Membranes*, 5th ed.; Elsevier Science: Oxford, 2008.
- (22) Farooqui, A. A.; Horrocks, L. A.; Farooqui, T. *Chem. Phys. Lipids* **2000**, *106*, 1-29.
- (23) Prasad, R. *Manual on membrane lipids*; Springer-Verlag: New York, 1996.
- (24) Beckerman, M. In *Molecular and Cellular Signaling*; Springer: New York, 2005, pp 161-186.
- (25) Yeagle, P. *The membranes of cells*; Academic Press: Orlando, 1987.
- (26) Fruhwirth, G. O.; Loidl, A.; Hermetter, A. *Biochim. Biophys. Acta* **2007**, *1772*, 718-736.
- (27) Bernheim, F.; Bernheim, M. L. C. *J. Biol. Chem.* **1939**, *127*, 353-360.
- (28) Reis, A.; Spickett, C. M. *Biochim. Biophys. Acta* **2012**, *1818*, 2374-2387.
- (29) Schaich, K. M. In *Bailey's Industrial Oil and Fat Products*; John Wiley & Sons: New York, 2005.
- (30) Megli, F. A.; Russo, L. *Biochim. Biophys. Acta* **2008**, *1778*, 143-152.
- (31) Sparrow, C. P.; Parthasarathy, S.; Steinberg, D. *J. Lipid Res.* **1988**, *29*, 745-753.
- (32) Kühn, H.; Belkner, J.; Suzuki, H.; Yamamoto, S. *J. Lipid Res.* **1994**, *35*, 1749-1759.
- (33) Kühn, H.; Heydeck, D.; Hugou, I.; Gniwotta, C. *J. Clin. Invest.* **1997**, *99*, 888.
- (34) Gunstone, F. D., Ed. *Fatty Acid and Lipid Chemistry*; Blackie Academic & Professional: Bishopbriggs, Glasgow, 1996.
- (35) Gugiu, B. G.; Mesaros, C. A.; Sun, M. J.; Gu, X. R.; Crabb, J. W.; Salomon, R. G. *Chem. Res. Toxicol.* **2006**, *19*, 262-271.
- (36) Niki, E. *Free Radical Biol. Med.* **2009**, *47*, 469-484.
- (37) Halliwell, B.; Chirico, S. *Am. J. Clin. Nutr.* **1993**, *57*, S715-S725.
- (38) Ohkawa, H.; Ohishi, N.; Yagi, K. *Anal. Biochem.* **1979**, *95*, 351-358.

- (39) Schiller, J.; Süß, R.; Arnhold, J.; Fuchs, B.; Leßig, J.; Müller, M.; Petković, M.; Spalteholz, H.; Zschörnig, O.; Arnold, K. *Prog. Lipid Res.* **2004**, *43*, 449-488.
- (40) Watson, J. T.; Sparkman, O. D., Eds. *Introduction to Mass Spectrometry: Instrumentation, Applications and Strategies for Data Interpretation*, 4th ed.; John Wiley & Sons, Ltd: West Sussex, 2007.
- (41) Benabdellah, F.; Seyer, A.; Quinton, L.; Touboul, D.; Brunelle, A.; Laprévotte, O. *Anal. Bioanal. Chem.* **2010**, *396*, 151-162.
- (42) Schmidt, A.; Karas, M.; Dulcks, T. *J. Am. Soc. Mass Spectrom.* **2003**, *14*, 492-500.
- (43) Hillenkamp, F.; Katalinic, J. P., Eds. *MALDI MS a Practical Guide to Instrumentation, Methods and Applications*; Wiley-VCH: Weinheim, 2007.
- (44) Chughtai, K.; Heeren, R. M. A. *Chem. Rev. (Washington, DC, U. S.)* **2010**, *110*, 3237-3277.
- (45) Stubiger, G.; Belgacem, O.; Rehulka, P.; Bicker, W.; Binder, B. R.; Bochkov, V. *Anal. Chem.* **2010**, *82*, 5502-5510.
- (46) Cohen, S. L. *Anal. Chem.* **2006**, *78*, 4352-4362.
- (47) Garrett, T. J.; Yost, R. A. *Anal. Chem.* **2006**, *78*, 2465-2469.
- (48) Landgraf, R. R.; Prieto-Conaway, M. C.; Garrett, T. J.; Stacpoole, P. W.; Yost, R. A. *Anal. Chem.* **2009**, *81*, 8488-8495.
- (49) Garrett, T. J.; Yost, R. A. In *Mass Spectrometry Imaging: Principles and Protocols*; Rubakhin, S. S., Sweedler, J. V., Eds.; Humana Press, 2010; Vol. 656, pp 209-230.
- (50) Menger, R. F.; Stutts, W. L.; Anbukumar, D. S.; Bowden, J. A.; Ford, D. A.; Yost, R. A. *Anal. Chem.* **2011**, *84*, 1117-1125.
- (51) Karas, M.; Bachmann, D.; Hillenkamp, F. *Anal. Chem.* **1985**, *57*, 2935-2939.
- (52) Guo, Z.; He, L. *Anal. Bioanal. Chem.* **2007**, *387*, 1939-1944.
- (53) Cohen, L.; Gusev, A. *Anal. Bioanal. Chem.* **2002**, *373*, 571-586.
- (54) Gross, J. In *Mass Spectrometry*; Springer-Verlag, 2011, pp 507-559.
- (55) Fuchs, B.; Schiller, J. In *Lipids in Health and Disease*; Quinn, P., Wang, X., Eds.; Springer Netherlands, 2008; Vol. 49, pp 541-565.
- (56) Dreisewerd, K. *Chem. Rev. (Washington, DC, U. S.)* **2003**, *103*, 395-425.

- (57) Stubiger, G.; Belgacem, O. *Anal. Chem.* **2007**, *79*, 3206-3213.
- (58) Griffiths, R. L.; Bunch, J. *Rapid Commun. Mass Spectrom.* **2012**, *26*, 1557-1566.
- (59) Karas, M.; Glückmann, M.; Schäfer, J. *J. Mass Spectrom.* **2000**, *35*, 1-12.
- (60) Karas, M.; Krüger, R. *Chem. Rev. (Washington, DC, U. S.)* **2003**, *103*, 427-440.
- (61) Zenobi, R.; Knochenmuss, R. *Mass Spectrom. Rev.* **1998**, *17*, 337-366.
- (62) Knochenmuss, R.; Zenobi, R. *Chem. Rev. (Washington, DC, U. S.)* **2003**, *103*, 441-452.
- (63) Jaskolla, T.; Karas, M. *J. Am. Soc. Mass Spectrom.* **2011**, *22*, 976-988.
- (64) *Qual Browser, v. 2.0.7*; LTQ XL Hardware Manual; Thermo Scientific: San Jose, Ca, 2006.
- (65) Krishnaveni, A.; Kumar Verma, N.; Menon, A. G.; Mohanty, A. K. *Int. J. Mass Spectrom.* **2008**, *275*, 11-20.
- (66) Schwartz, J. C.; Senko, M. W.; Syka, J. E. P. *J. Am. Soc. Mass Spectrom.* **2002**, *13*, 659-669.
- (67) March, R. E.; Todd, J. F. J. *Quadrupole Ion Trap Mass Spectrometry*, 2nd ed.; Wiley: Hoboken, 2005.
- (68) Garrett, T. J.; Prieto-Conaway, M. C.; Kovtoun, V.; Bui, H.; Izgarian, N.; Stafford, G.; Yost, R. A. *Int. J. Mass Spectrom.* **2007**, *260*, 166-176.
- (69) Sleno, L.; Volmer, D. A. *J. Mass Spectrom.* **2004**, *39*, 1091-1112.
- (70) Rubakhin, S. S.; Sweedler, J. V., Eds. *Mass Spectrometry Imaging: Principles and Protocols*; Springer: New York, 2010.
- (71) Murphy, R. C.; Hankin, J. A.; Barkley, R. M. *J. Lipid Res.* **2009**, *50 Suppl*, S317-322.
- (72) Sjövall, P.; Lausmaa, J.; Johansson, B. *Anal. Chem.* **2004**, *76*, 4271-4278.
- (73) Berry, K. A.; Li, B.; Reynolds, S. D.; Barkley, R. M.; Gijon, M. A.; Hankin, J. A.; Henson, P. M.; Murphy, R. C. *J. Lipid Res.* **2011**, *52*, 1551-1560.
- (74) McDonnell, L. A.; Heeren, R. M. A. *Mass Spectrom. Rev.* **2007**, *26*, 606-643.
- (75) Amstalden van Hove, E. R.; Smith, D. F.; Heeren, R. M. A. *J. Chromatogr., A* **2010**, *1217*, 3946-3954.

- (76) Cornett, D. S.; Reyzer, M. L.; Chaurand, P.; Caprioli, R. M. *Nat. Methods* **2007**, *4*, 828-833.
- (77) Schwartz, S. A.; Reyzer, M. L.; Caprioli, R. M. *J. Mass Spectrom.* **2003**, *38*, 699-708.
- (78) Römpf, A.; Spengler, B. *Histochem. Cell Biol.* **2013**, *139*, 759-783.
- (79) Landgraf, R. R. Analysis of lipids in nerve tissue by MALDI tandem mass spectrometric imaging. Ph.D. Thesis, University of Florida, Gainesville, FL, 2009.
- (80) Puolitaival, S.; Burnum, K.; Cornett, D. S.; Caprioli, R. *J. Am. Soc. Mass Spectrom.* **2008**, *19*, 882-886.
- (81) Axelsson, J.; Hoberg, A.-M.; Waterson, C.; Myatt, P.; Shield, G. L.; Varney, J.; Haddleton, D. M.; Derrick, P. J. *Rapid Commun. Mass Spectrom.* **1997**, *11*, 209-213.
- (82) Baluya, D. L.; Garrett, T. J.; Yost, R. A. *Anal. Chem.* **2007**, *79*, 6862-6867.
- (83) Chen, Y.; Allegood, J.; Liu, Y.; Wang, E.; Cachon-Gonzalez, B.; Cox, T. M.; Merrill, A. H.; Sullards, M. C. *Anal. Chem.* **2008**, *80*, 2780-2788.
- (84) Hankin, J. A.; Barkley, R. M.; Murphy, R. C. *J. Am. Soc. Mass Spectrom.* **2007**, *18*, 1646-1652.
- (85) Garrett, T. J. Imaging small molecules in tissue by matrix-assisted laser desorption/ionization tandem mass spectrometry. Ph.D. Thesis, University of Florida, Gainesville, FL, 2006.
- (86) Strupat, K.; Kovtoun, V.; Bui, H.; Viner, R.; Stafford, G.; Horning, S. *J. Am. Soc. Mass Spectrom.* **2009**, *20*, 1451-1463.
- (87) Yin, H.; Cox, B. E.; Liu, W.; Porter, N. A.; Morrow, J. D.; Milne, G. L. *J. Mass Spectrom.* **2009**, *44*, 672-680.
- (88) Salomon, R. G.; Gu, X. *Chem. Res. Toxicol.* **2011**, *24*, 1791-1802.
- (89) Sun, M. J.; Finnemann, S. C.; Febbraio, M.; Shan, L.; Annangudi, S. P.; Podrez, E. A.; Hoppe, G.; Darrow, R.; Organisciak, D. T.; Salomon, R. G.; Silverstein, R. L.; Hazen, S. L. *J. Biol. Chem.* **2006**, *281*, 4222-4230.
- (90) Leitinger, N. *Curr. Opin. Lipidol.* **2003**, *14*, 421-430.
- (91) Lee, S.; Birukov, K. G.; Romanoski, C. E.; Springstead, J. R.; Lusic, A. J.; Berliner, J. A. *Circ. Res.* **2012**, *111*, 778-799.
- (92) Gao, D.; Ashraf, M. Z.; Kar, N. S.; Lin, D.; Sayre, L. M.; Podrez, E. A. *J. Biol. Chem.* **2010**, *285*, 4447-4454.

- (93) Tokumura, A.; Sumida, T.; Toujima, M.; Kogure, K.; Fukuzawa, K.; Takahashi, Y.; Yamamoto, S. *J. Lipid Res.* **2000**, *41*, 953-962.
- (94) Kayganich-Harrison, K. A.; Murphy, R. C. *Anal. Biochem.* **1994**, *221*, 16-24.
- (95) Watson, A. D.; Leitinger, N.; Navab, M.; Faull, K. F.; Hörkkö, S.; Witztum, J. L.; Palinski, W.; Schwenke, D.; Salomon, R. G.; Sha, W.; Subbanagounder, G.; Fogelman, A. M.; Berliner, J. A. *J. Biol. Chem.* **1997**, *272*, 13597-13607.
- (96) Frey, B.; Haupt, R.; Alms, S.; Holzmann, G.; König, T.; Kern, H.; Kox, W.; Rüstow, B.; Schlame, M. *J. Lipid Res.* **2000**, *41*, 1145-1153.
- (97) Nakamura, T.; Henson, P. M.; Murphy, R. C. *Anal. Biochem.* **1998**, *262*, 23-32.
- (98) Hall, L. M.; Murphy, R. C. *Anal. Biochem.* **1998**, *258*, 184-194.
- (99) Reis, A.; Domingues, P.; Ferrer-Correia, A. J. V.; Domingues, M. R. M. *J. Mass Spectrom.* **2004**, *39*, 1513-1522.
- (100) Nakanishi, H.; Iida, Y.; Shimizu, T.; Taguchi, R. *J. Chromatogr., B: Anal. Technol. Biomed. Life Sci.* **2009**, *877*, 1366-1374.
- (101) Spickett, C. M.; Rennie, N.; Winter, H.; Zambonin, L.; Landi, L.; Jerlich, A.; Schaur, R. J.; Pitt, A. R. *Biochem. J.* **2001**, *355*, 449-457.
- (102) Oskolkova, O. V.; Afonyushkin, T.; Preinerstorfer, B.; Bicker, W.; von Schlieffen, E.; Hainzl, E.; Demyanets, S.; Schabbauer, G.; Lindner, W.; Tselepis, A. D.; Wojta, J.; Binder, B. R.; Bochkov, V. N. *J. Immunol.* **2010**, *185*, 7706-7712.
- (103) Domingues, M. R. M.; Simões, C.; da Costa, J. P.; Reis, A.; Domingues, P. *Biomed. Chromatogr.* **2009**, *23*, 588-601.
- (104) Reis, A.; Domingues, P.; Ferrer-Correia, A. J. V.; Domingues, M. R. M. *Rapid Commun. Mass Spectrom.* **2004**, *18*, 2849-2858.
- (105) Reis, A.; Domingues, M. R. M.; Amado, F. M. L.; Ferrer-Correia, A. J. V.; Domingues, P. *Biomed. Chromatogr.* **2005**, *19*, 129-137.
- (106) Stübiger, G.; Belgacem, O. *Anal. Chem.* **2007**, *79*, 3206-3213.
- (107) van den Brink, O. F.; Boon, J. J.; O'Connor, P. B.; Duursma, M. C.; Heeren, R. M. A. *J. Mass Spectrom.* **2001**, *36*, 479-492.
- (108) Bischoff, A.; Eibisch, M.; Fuchs, B.; Suss, R.; Schurenberg, M.; Suckau, D.; Schiller, J. *Acta Chromatogr.* **2011**, *23*, 365-375.
- (109) Vance, J. E. *J. Lipid Res.* **2008**, *49*, 1377-1387.

- (110) Domingues, P.; Domingues, M. R. M.; Amado, F. M. L.; Ferrer-Correia, A. J. *Rapid Commun. Mass Spectrom.* **2001**, *15*, 799-804.
- (111) Pulfer, M.; Murphy, R. C. *Mass Spectrom. Rev.* **2003**, *22*, 332-364.
- (112) Hsu, F.-F.; Turk, J. *J. Am. Soc. Mass Spectrom.* **2003**, *14*, 352-363.
- (113) Han, X.; Gross, R. W. *J. Am. Soc. Mass Spectrom.* **1995**, *6*, 1202-1210.
- (114) Hsu, F.-F.; Turk, J. *J. Am. Soc. Mass Spectrom.* **2010**, *21*, 657-669.
- (115) Hsu, F.-F.; Turk, J. *J. Chromatogr., B: Anal. Technol. Biomed. Life Sci.* **2009**, *877*, 2673-2695.
- (116) Cheng, C.; Gross, M. *J. Am. Soc. Mass Spectrom.* **1998**, *9*, 620-627.
- (117) Suzuki, M.; Kamei, M.; Itabe, H.; Yoneda, K.; Bando, H.; Kume, N.; Tano, Y. *Mol. Vis.* **2007**, *13*, 772-778.
- (118) Busik, J. V.; Reid, G. E.; Lydic, T. A. *Methods Mol. Biol.* **2009**, *579*, 33-70.
- (119) Khaselev, N.; Murphy, R. C. *Free Radical Biol. Med.* **1999**, *26*, 275-284.
- (120) von Schlieffen, E.; Oskolkova, O. V.; Schabbauer, G.; Gruber, F.; Bluml, S.; Genest, M.; Kadl, A.; Marsik, C.; Knapp, S.; Chow, J.; Leitinger, N.; Binder, B. R.; Bochkov, V. N. *Arterioscler., Thromb., Vasc. Biol.* **2009**, *29*, 356-362.
- (121) Hsu, F.-F.; Turk, J. *J. Mass Spectrom.* **2000**, *35*, 595-606.
- (122) Chen, X.; Steill, J. D.; Oomens, J.; Polfer, N. C. *J. Am. Soc. Mass Spectrom.* **2010**, *21*, 1313-1321.
- (123) Radak, Z.; Zhao, Z.; Goto, S.; Koltai, E. *Mol. Aspects Med.* **2011**, *32*, 305-315.
- (124) Subbanagounder, G.; Watson, A. D.; Berliner, J. A. *Free Radical Biol. Med.* **2000**, *28*, 1751-1761.
- (125) Watson, B. D.; Busto, R.; Goldberg, W. J.; Santiso, M.; Yoshida, S.; Ginsberg, M. D. *J. Neurochem.* **1984**, *42*, 268-274.
- (126) Marathe, G. K.; Harrison, K. A.; Murphy, R. C.; Prescott, S. M.; Zimmerman, G. A.; McIntyre, T. M. *Free Radical Biol. Med.* **2000**, *28*, 1762-1770.
- (127) Amstalden van Hove, E. R.; Blackwell, T. R.; Klinkert, I.; Eijkel, G. B.; Heeren, R. M. A.; Glunde, K. *Cancer Res.* **2010**, *70*, 9012-9021.
- (128) Alexandrov, T. *BMC Bioinf.* **2012**, *13 Suppl 16*, S11.

- (129) Eijkel, G. B.; Kükrer Kaletaş, B.; van der Wiel, I. M.; Kros, J. M.; Luider, T. M.; Heeren, R. M. A. *Surf. Interface Anal.* **2009**, *41*, 675-685.
- (130) Hasegawa, M.; Hakamata, H.; Matsunaga, I.; Kusu, F. *Eur. J. Lipid Sci. Technol.* **2011**, *113*, 423-429.
- (131) Lyons, M. A.; Brown, A. J. *Int. J. Biochem. Cell Biol.* **1999**, *31*, 369-375.
- (132) Milne, G. L.; Porter, N. A. *Lipids* **2001**, *36*, 1265-1275.
- (133) Bayir, H.; Tyurin, V. A.; Tyurina, Y. Y.; Viner, R.; Ritov, V.; Amoscato, A. A.; Zhao, Q.; Zhang, X. J.; Janesko-Feldman, K. L.; Alexander, H.; Basova, L. V.; Clark, R. S. B.; Kochanek, P. M.; Kagan, V. E. *Ann. Neurol.* **2007**, *62*, 154-169.
- (134) Tyurina, Y. Y.; Kini, V.; Tyurin, V. A.; Vlasova, I. I.; Jiang, J.; Kapralov, A. A.; Belikova, N. A.; Yalowich, J. C.; Kurnikov, I. V.; Kagan, V. E. *Mol. Pharmacol.* **2006**, *70*, 706-717.
- (135) Calcutt, N. A.; Lopez, V. L.; Bautista, A. D.; Mizisin, L. M.; Torres, B. R.; Shroads, A. L.; Mizisin, A. P.; Stacpoole, P. W. *J. Neuropathol. Exp. Neurol.* **2009**, *68*, 985-993.
- (136) Feldman, E. L. *J. Clin. Invest.* **2003**, *111*, 431-433.
- (137) Cunha, J. M.; Jolival, C. G.; Ramos, K. M.; Gregory, J. A.; Calcutt, N. A.; Mizisin, A. P. *Metab., Clin. Exp.* **2008**, *57*, 873-881.

## BIOGRAPHICAL SKETCH

Whitney Leigh Stutts, the daughter of Debbie and Terry Stutts and older sister to Lauren Stutts, was born in Winston-Salem, North Carolina. She grew-up in the beautiful foothills of NC where she enjoyed the outdoors and local music. After graduating from East Wilkes High School, Whitney began a degree in chemistry at North Carolina State University.

While at NC State, Whitney was involved in the University Scholars Program and Alpha Chi Sigma, the professional chemistry fraternity. She also conducted undergraduate research under the direction of Dr. Damian Shea, studying the fate and concentrations of steroid hormones in North Carolina's surface waters. During the summers, Whitney worked as a clinical laboratory technician at Suncare Research Laboratory assessing the photostability, phototoxicity, and photoallergenicity of sunscreens and dermatological products through in vitro and in vivo studies. In December of 2007, Whitney graduated magna cum laude with a Bachelor of Science degree in chemistry and a minor in environmental toxicology.

In 2008, Whitney began her graduate career at the University of Florida, pursuing a doctorate of philosophy in chemistry. She joined Dr. Richard A. Yost's group and, for the past five years, has investigated oxidized lipids by MALDI MS<sup>n</sup>. Over the course of her graduate career, Whitney had several collaborations, domestic and international, and greatly enjoyed merging two of her passions, science and traveling. Whitney completed her doctorate in August 2013. She hopes to pursue a career in mass spectrometry and lead others in their scientific endeavors.